COMPUTATIONAL FLUID DYNAMICS SIMULATION OF THE AIRFLOW THROUGH THE HUMAN RESPIRATORY TRACT

By

Jamasp Azarnoosh

Kidambi Sreenivas
Research Professor,
Computational Engineering
(Chairperson/Principal Adviser)

Abdollah Arabshahi
Research Professor,
Computational Engineering
(Committee Member)

James C. Newman, III
Professor,
Computational Engineering
(Committee Member)

COMPUTATIONAL FLUID DYNAMICS SIMULATION OF THE AIRFLOW THROUGH THE HUMAN RESPIRATORY TRACT

By

Jamasp Azarnoosh

A Thesis Submitted to the Faculty of the University of Tennessee at Chattanooga in Partial Fulfillment of the Requirements of the Degree of Master of Science: Engineering

The University of Tennessee at Chattanooga
Chattanooga, Tennessee

August 2016

ABSTRACT

This study compares the effect of extra-thoracic airways (ETA) on the flow field through the lower airways by carrying out simulations of the airflow through the human respiratory tract. Three geometries, consisting of the ETA, CT-derived lower airway, and a combination of the two were utilized in simulations that were performed for transient breathing in addition to constant inspiration/expiration. Physiologically-appropriate regional ventilation for two different flow rates was induced at the distal boundaries by imposing appropriate lobar specific flow rates. Two breathing rates were considered, i.e., 7.5 and 15 breaths per minute with a tidal volume of 0.5 liter. For comparison, the flow rates for constant inspiration/expiration were selected to be identical to the peak flow rates during the transient breathing. Significant differences indicate that simulations that utilize constant inspiration or expiration may not be appropriate for gaining insight into the flow patterns through the human airways.

ACKNOWLEDGEMENTS

First and foremost, I truly appreciate my major advisor, Dr. Kidambi Sreenivas for his advice, guidance throughout this research.

I would like to thank my committee members, Dr. Abi Arabshahi and Dr. James Newman III, for valuable discussions and their helps. Furthermore, I really thank Richard R. Gruetzemacher, III for sharing his vast knowledge in this research. Indeed, this thesis would not have been possible without the support and assistance of him.

TABLE OF CONENTS

LIST OF TABLES

LIST OF FIGURES

LIST OF ABBREVIATIONS

CFD, Computational Fluid Dynamics

COPD, Chronic obstructive pulmonary disease

PIV, Particle Image Velocimetry

RANS, Reynolds Averaged Naviers-Stokes

SST, Shear Stress Transport

LBM, Lattice Boltzmann Method

DNS, Direct Numerical Simulation

DES, Detached eddy Simulation

LES, Large Eddy Simulation

TI, Turbulence intensity [Nondimensional]

TKE, Turbulence kinetic energy [m^2/s^2]

SGS, Subgrid-scale

LIST OF SYMBOLS

A_{out}, Local Area at the outlet [m^2]

A_{local}, Local cross-sectional area [m^2]

U_{local}, Local bulk velocity or mean velocity magnitude at the airway location [m/s]

D, Average diameter of the trachea [m]

De, Dean Number [Nondimensional]

L, Liter

Q, Flow rate [m^3/s]

Re, Reynolds number [Nondimensional]

Re', Reynolds number of the ETA [Nondimensional]

T, time [s]

u, Cartesian velocity component [m/s]

$\bar{u}$, Filtered velocity

y^+, Dimensionless wall distance for a wall-bounded flow [Nondimensional]

x, y, z, Cartesian coordinates [m]

μ_t, Turbulence eddy viscosity [m^2/s]

U_{max}, Maximum velocities imposed at the distal boundaries [m/s]

$\overline{V}_{max}$, Maximum velocity at each bronchi branch [m/s]

Ω, Angular frequency of the oscillation [1/s]

Δv_{lobe}, Lobar volume [m^3]

δ_{ij}, Kronecker delta [$\delta_{ij} = 1$ if $i = j$ otherwise it is zero]

$\bar{S}_{ij}$, Rate of strain tensor or deformation tensor

f, The breathing rate [Hz]

ν, Kinematic viscosity [m^2/s]

α, Womersley number [Nondimensional]

τ_{ij}, Subgrid-scale stress tensor

u_i', u_j', Velocity fluctuation

ϕ, Phase angle

V, The volume of a computational cell

i, j, k, coordinate index

CHAPTER I

INTRODUCTION

There are hundreds of millions of people worldwide who suffer from chronic respiratory diseases such as asthma and chronic obstructive pulmonary disorder (COPD), obstructive sleep apnea syndrome (OSAS), pulmonary hypertension, etc. [1]. Asthma and COPD are significant public health burdens and the symptoms of asthma include wheezing, coughing, chest tightness, and shortness of breath. It is reported that approximately 4% of the United States population is affected by OSAS [2]. OSAS occurs during sleep wherein breathing repeatedly stops and starts. Air pollution is directly connected to these illnesses because of the deposition of particulate pollutants in the lungs. These toxic pollutant particles have the potential to induce these diseases. Inhaled pharmaceuticals are widely utilized to overcome these lung illnesses, due to their convenience and rapid action. Particles are transported to the lungs by inhalation; therefore the flow field within the respiratory system will influence the deposition patterns of airborne pollutants and pharmacological drugs. These effects are very prominent in the extra-thoracic airway (ETA). An investigation reported that 80–95% of an inhaled aerosol dose is deposited in the ETA [3]. This observation illustrates that the ETA acts as a filter and decreases the delivery of medication to the lungs. In practice, particle deposition decreases the optimal delivery of treatment medicines to the lungs. The flow field inside the ETA has a profound effect on drug deposition. A detailed analysis of the airflow mechanisms within the human respiratory tract could lead to a better understanding of the deposition of toxic aerosols during breathing and help

with health risk assessments. Complex airflow patterns in the airways, while effective at removing inhaled toxic elements, hinder the delivery of therapeutic materials delivered through inspiration.

Over the past 20 years, computational fluid dynamics (CFD) has been established as a powerful tool for the study of these complex flow patterns and its application to improvements in aerosolized medication delivery. CFD is a technique that is capable of providing details in physical models to predict nonlinear transitional/turbulent airflow. It refers to the use of numerical methods to solve the Navier-Stokes equations, which are the partial differential equations governing the flow of a single-phase Newtonian fluid. Even with these advances, the complex flow patterns in these airways are still understood only at a relatively rudimentary level.

In the present study, the simulations of the airflow through three geometries, i.e., ETA, lower airway, and entire (combined ETA and lower airway) geometry, were conducted. The computational results of the ETA were validated by comparing to experimental and computational results from other researchers. Analysis of the flow field is presented for two normal breathing cycles as well as analogous constant inspiration/expiration for the geometries considered in this study. The main goal of this research is to investigate the effects of the ETA on the flow regime through pulmonary airway. CFD calculations are carried out by solving the Navier-Stokes equations using either a Large Eddy Simulation (LES) or the shear stress transport (SST) turbulence model. The SST model was used for validation cases of the ETA geometry only while all cases were simulated using LES.

CHAPTER II

LITERATURE REVIEW

Over the last decade, the airflow pattern and particle deposition through the human respiratory tract has been studied extensively, both experimentally and via numerical simulations. Studies utilizing only the lower airways typically use a laminar profile at the trachea, which is the point of delineation between the ETA and the lower airways. However, various studies conducted using ETA models, have clearly shown that the flow exiting the ETA is very likely turbulent[4][5][6][7][8]. The inherent complexity of flows through the ETA can lead to regions which are laminar, transitional or fully turbulent. Attempts to study flows (experimental or computational) through the ETA are stymied because of the wide variability in ETA geometries depending on age, disease, etc. One approach to the problem of variability is to create an idealized ETA geometry which contains all the basic physiological elements that are present in the real geometry. Yu et al. [9] used a teaching model as the basis of the geometry for the ETA while Stapleton et al. [10] utilized an idealized version of an ETA based on CT scans. Stapleton et al. investigated airflow and particle deposition using $k-\varepsilon$ Reynolds-averaged Navier–Stokes (RANS) turbulence model for the low (2 l/min) and high flow rates (28.3 l/min) and good agreement was reported only for the low flow rate. The so called Alberta ETA geometry [4] has been studied extensively using both experimental [4], [11] and computational [5], [6] approaches. Ball et al. [5] used various RANS turbulence models to simulate the flow through this geometry and compared their results to experimental data. They also used a Lattice Boltzmann method

(LBM) to study the details of the flow field [6]. In this novel approach the discrete Boltzmann equation is solved to conduct a direct numerical simulation (DNS). LBM is a stable method and the convection operator is linear, while convection term in Navier–Stokes equations is nonlinear. Slightly better agreement has been achieved using LBM than that using RANS models, but still some discrepancies were observed between experimental data and LBM solutions. In the following years, Kleinstreuer and Zhang [7] used LES approach to simulate airflow through this geometry. Due to the nature of the Alberta geometry, the nasal cavity is excluded for investigation of airflow and particle deposition. There are several investigations on the nasal cavity that interested readers are referred to [12], [13],[14].

Over the years several geometries of the lung have been studied. The framework for the study of the airflow through the lung and human pulmonary airways was laid by Weibel [15] and Horsfield et al. [16]. One of the very first models was proposed by Weibel [15]. Weibel Type A and B models are not realistic and based upon data and observations in his study. The geometric data reported by Weibel are for normal breathing for an adult lung. In late 1960s, Horsfield et al [16] expanded Weibel's work and studied airflow through two models of pulmonary airways experimentally to provide more details of irregular dichotomy in the pulmonary airways.

Due to the importance of the accurate prediction of the airflow and particle deposition in pulmonary system, most researchers nowadays concentrate on realistic lung models. For instance, Xu et al. [17] simulated constant inspiration and expiration of the airflow through a CT-based geometry. De Backer et al. [18] carried out numerical simulation of constant inspiration through CT-based lower airways. Another steady inspiration simulation was performed by Van Ertbruggen et al. [19] through a realistic three-dimensional (3D) seven-generation model of the bronchial tree based upon the morphometrical data of Horsfield et al.

There are two major regions of the ETA, i.e. larynx and trachea, which mainly impact on the fluid flow and proportion of deposition of the entire respiratory tract. Lin et al. [8] compared the effects of an ETA by simulating the airflow through a CT-derived model of the upper respiratory tract and the lower airways with the corresponding lower airway geometry only. They concluded that a curved sheet-like turbulent laryngeal jet in the entire airway geometry, with turbulence intensity exceeding 10 to 20% in the trachea, could significantly affect airway flow patterns as well as tracheal wall shear stress. Similar observations were made by Corcoran et al. [20] in a simplified model of the larynx–trachea.

These simulations were limited to constant inspiration only. Oscillating flow through idealized lower airways has been examined in the literature as well. For instance, Tanaka et al. [21] conducted experimental investigation in a five-generation model based upon the data from Horsfield et al. during high-frequency oscillating with Womersley number (α = 7.5). In the flowing year, Zhang and Kleinstreuer [22] compared both the peak inspiration and expiration velocity profiles for α = 0.93 and found good agreement with those of instantaneously equivalent constant inspiration/expiration cases and reported quasi-steady flow through planer and nonplaner bifurcations. In another study, an experimental particle image velocimetry (PIV) study of breathing cycle was carried out by Ramuzat et al.[23] in an idealized three-generation model.

In an earlier study, the effects of inhalation transience through CT-based human airway geometry were explored by Gruetzemacher[24], where he obtained solutions for five complete breathing cycles. As is the norm in these types of simulations, a uniform velocity profile was imposed at the trachea (for the constant inspiration case) and lobar specific flow rates were imposed at the distal airways (for the full breathing cycle). An interested reader directed to Gruetzemacher [24] for more details.

For the computational simulation the use of appropriate CFD technique is significant for obtaining correct airflow structures within the respiratory tract. There are four approaches for simulation of turbulent flows, namely DNS, RANS turbulent models, LES and Detached eddy simulations (DES). Simulation of the airflow through respiratory tract has not been conducted using DES approach by any researcher thus far. Generally, RANS turbulence models were used by researchers, and the common turbulence models were either the $k-\varepsilon$ or $k-\omega$ models. Nevertheless, RANS methods may be inaccurate for separated turbulent flows, due to numerous limitations associated with RANS turbulence modeling. An appropriate approach, in terms of computational costs and better prediction of high levels of unsteadiness in the flow, is LES which only models the effects of the small scales on the large scales. This method requires fine mesh and is much more expensive than RANS methods. Because of low computational cost, RANS methods have commonly been utilized to simulate airflow through human airways. Nonetheless, these models provided acceptable solution of the time-averaged airflow; it is difficult for the RANS models to predict airflow fluctuations to provide accurate solution[5]. In order to capture time-varying nature of the airflow through complicated geometries, LES is a proper technique to apply. Hence, most researchers considered LES as an appropriate and accurate method for simulating of airflow in this complex geometry (see [25], [7], [26], [27] and [28]).

Numerical studies provide detailed information of airflow patterns that is very difficult to obtain using in vivo observations or in vitro experiments. The majority of attention by most researchers has been directed to the inspiration portion of the cycle, i.e. steady state boundary conditions, although some of them did consider a full breathing cycle or constant expiration. The geometries utilized in most of these studies were limited to either the ETA or the lower airway only. This study focuses on the effects of the ETA on the lower airway (and vice versa) for one

full breathing cycle and compares the results of transient simulations with simulations corresponding to constant inspiration and expiration using LES method.

CHAPTER III

COMPUTATIONAL METHODS

This chapter presents the description of the three computational geometries utilized in this study. Details regarding the mesh generation are also provided. A brief description of the flow solver is presented followed by a discussion on the physiologically appropriate, lobar-specific boundary conditions for the simulation of the transient breathing cycle.

3.1. Computational Geometries

3.1.1. The Idealized Upper Airway Geometry (Alberta Geometry)

Because of the existence of geometric variability in the ETA from a child to a healthy or diseased adult, it is useful to consider an idealized geometry which consists of all the basic physiological elements such as the oral cavity, none-nasal pharynx, the larynx and the trachea. The computational ETA geometry utilized in this study is based on the so-called Alberta ETA model from The University of Alberta which mimics the complete extra-thoracic airway from the oral cavity to the trachea of an adult human. Licensing issues prevented the actual geometry from being used in this research. The geometry utilized in this study has been reconstructed based on the descriptions and cross-sections available in the literature, for instance [4], [11] and [29]. The geometry was created using SolidWorks, a 3D Computer Aided Design (CAD) modeling package. The overall height (including the inlet nozzle) and width of this geometry are 160.4 and 110 mm, respectively. Figure 3.1.1 shows the dimensions and the anatomical names which

include the most important airflow structures in the sagittal plane of the ETA. Traverse cross-sectional views of the airway passage of all thirteen cross-sections are depicted in Figure 3.1.1c.

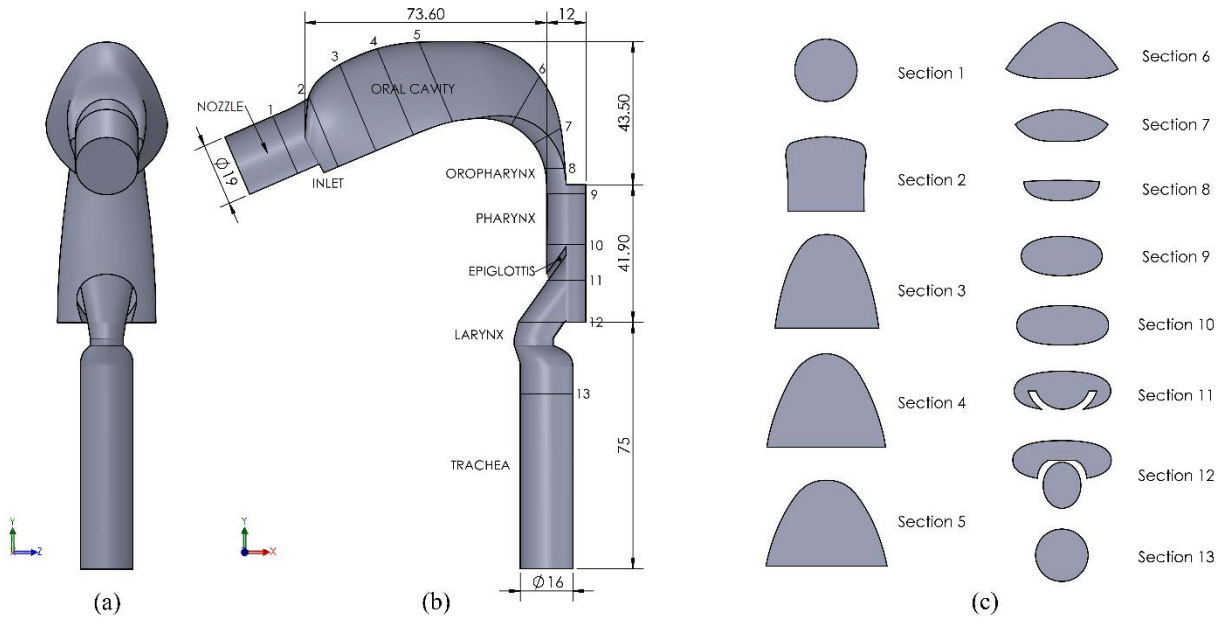

Figure 3.1.1 The idealized ETA geometry: (a) Coronal view (b) Sagittal cross section view with dimensions (c) Traverse cross sectional views of the airway passages

The various regions of the ETA are geometrically very different which is revealed in the complexity of the model. The oral cavity features different radii of curvature along the sagittal and coronal (frontal) planes. In the posterior of the oral cavity, the cross sectional shape converges to a somewhat half elliptical shape, and is then extended by the uvula. The shape remains elliptical within the pharynx before the glottal region. The epiglottis protrudes into the pharynx volume, thus the airflow must travel around it before entering the trachea and then on to the main bronchi and subsequently the lungs.

As can be seen from Figure 3.1.1, the local area increases from the inlet to the oral cavity and then decreases through the oro-pharynx (cross-sections 2-8). There is a sudden change in the

local area from oro-pharynx to pharynx (cross-sections 8-9). Thus, the bulk velocity decreases, consequently reducing the Reynolds number. The existence of epiglottis (cross-sections 11 and 12) in the pharynx causes this region of the model to be more complicated. Even though the Reynolds numbers is low, because of the shape of the geometry, transition to turbulent flow is expected.

3.1.2. The Lower Airway Geometry (CT-based Airway)

In the recent study by Gruetzmacher [24], two sets of CT imagery were selected for surface reconstruction (Standard Resolution Computed Tomography (SRCT) and High Resolution Computed Tomography (HRCT)). For the simulations that were carried out as part of that study, SRCT was used. This imagery was obtained by assistance of The University of Tennessee College of Medicine, Chattanooga (UTCOMC). Imagery from a healthy patient's chest was selected from patients at Erlanger Medical Center, de-identified, and provided for use in this study. The generation of the surface model was performed by Slicer3D, an open source medical imaging software package, and was exported as a point cloud. MeshLab, an open source meshing package, was used for the surface reconstruction. The resulting 9-generation CT-based lower airway geometry, depicted in Figure 3.1.2, consists of 25 outlets and was used in the current study. The interested reader is directed to Gruetzemacher [24] for details about the geometry.

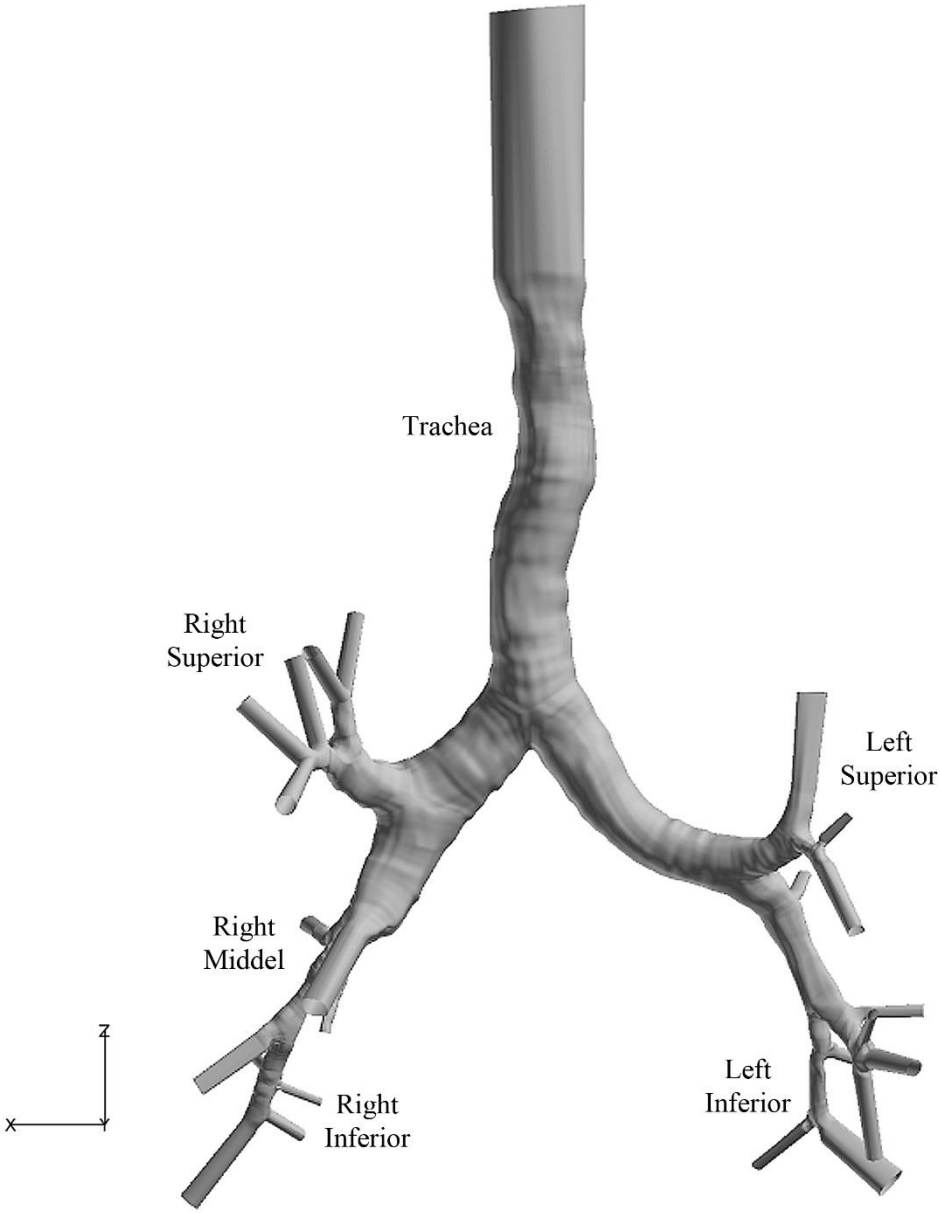

Figure 3.1.2 A 9-generation CT-based lower airway geometry

3.1.3. The Entire Airway Geometry

The ETA geometry (Figure 3.1.1) was scaled to match with the CT-based lower airways model of Gruetzmacher (Figure 3.1.2) to provide the combined upper/lower airways model or the entire airway geometry (Figure 3.1.3 a, b).

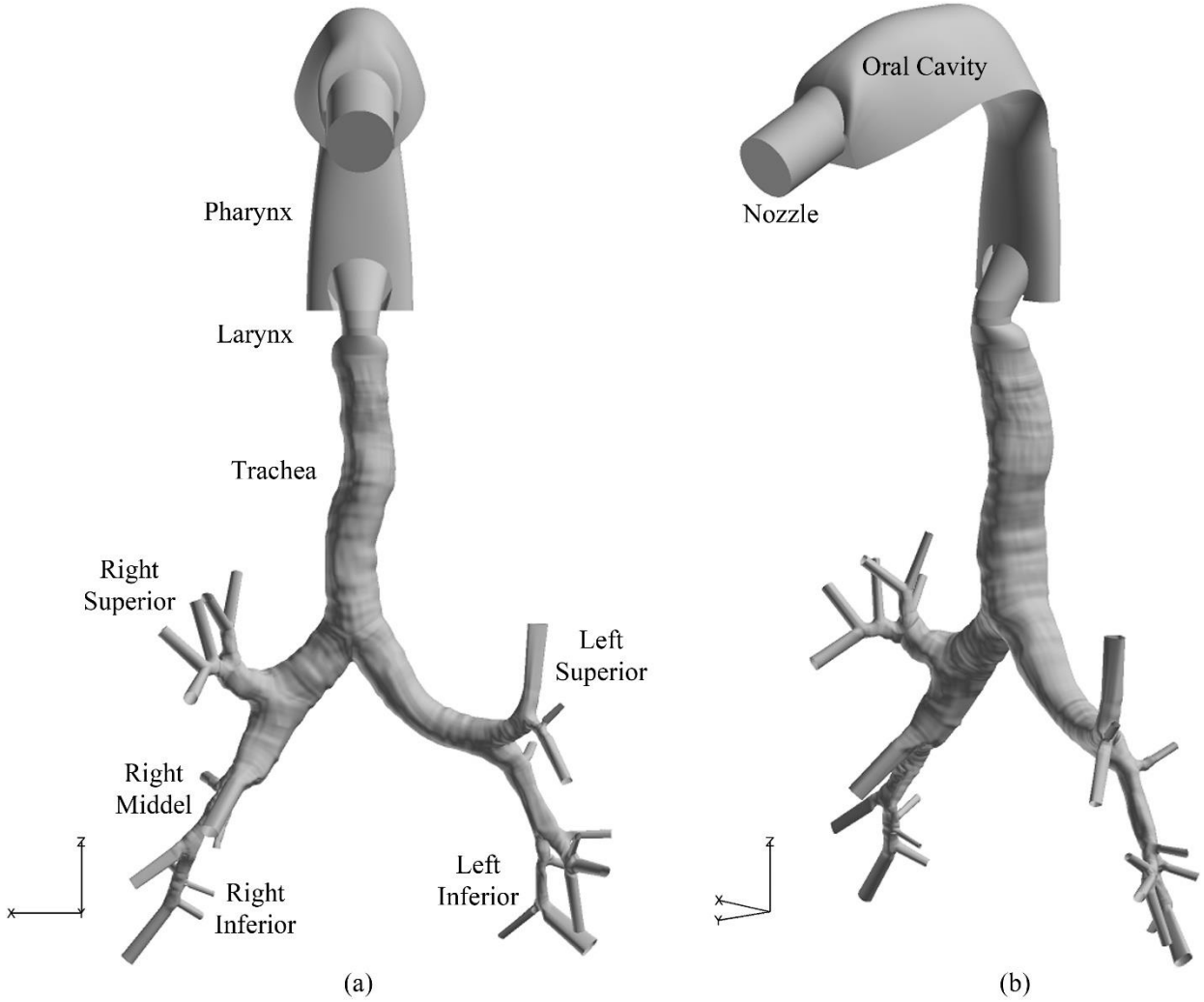

Figure 3.1.3 The entire airway geometry: a) Coronal view. b) Right oblique (45°)

3.2. Mesh Generation

All geometries were meshed using Pointwise version 17.3. Note that the CAD model of the ETA was imported in Initial Graphic Exchange Specification (IGES) format into Pointwise for generating the mesh. The surface meshes were almost entirely structured for all the geometries except for a small region in the trachea. The volume mesh was generated using an off-wall spacing ranging from 0.01 to 0.05 mm such that an average y^+ of around unity was obtained. The

volume mesh utilized the T-Rex feature of Pointwise [30]. This resulted in the extrusion of regular layers of tetrahedra from boundaries, which are recombined to obtain prism elements off the walls. A minimum of 7 prism layers were utilized in this study.

Total of five meshes were generated. Two different meshes were generated for the ETA and the entire airway geometry so as to maintain adequate viscous resolution for the two different flow rates considered in this study, whereas only one mesh for the lower airway geometry was generated. The mesh for the lower airway maintains the necessary viscous resolution for both flow rates. Number of nodes and volume elements of all meshes are summarized in Table 3.2.1.

Table 3.2.1 Number of nodes and volume elements of all grids

Geometry		Low flow rate		High flow rate	
		Nodes	Number of volume elements	Nodes	Number of volume elements
The upper airway	Coarse	4,990,450	12,979,034	5,110,5590	13,559,688
	Fine	9,744,653	25,520,582	10,059,168	27,399,523
The lower airway		3,142,780	18,035,344	3,142,780	18,035,344
The entire airway		7,886,440	31,157,333	8,491,553	32,788,751

3.3. Flow Solver

The in-house flow solver, *Tenasi* [31], was used in this study to simulate constant inspiration/expiration and four full respiratory breathing cycles. The baseline flow solver in *Tenasi* employs a node centered, finite volume, implicit scheme with high resolution fluxes based on Roe averaging and a Newton subiteration procedure for time accuracy. The linear system at each Newton subiteration is solved using a symmetric Gauss–Seidel algorithm. For the cases considered here, *Tenasi* solves the artificial-compressibility form of the incompressible Navier-

Stokes equations. *Tenasi* has been validated in a previous study for steady and unsteady flow through idealized and CT-based geometries [24].

All simulations were conducted using a Large Eddy Simulation (LES) formulation to investigate structure of turbulent flows through these complex geometries. LES is sufficient to resolve the large-scale eddies of turbulent flow without using any turbulence model, however, this is inappropriate to resolve smaller scales of turbulent motions i.e. length scales smaller than the grid spacing. Therefore, these small unresolved length scales are modeled by a SGS turbulence model. In this study, the Wall-Adapting Local Eddy-viscosity (WALE) model [32] is used for the SGS stresses. The SGS tensor τ_{ij} is given by

$$\tau_{ij} = \bar{u}_i\bar{u}_j - \overline{u_i u_j} \tag{1}$$

Subgrid scale modeling is based upon an eddy-viscosity assumption. The eddy viscosity model is defined as

$$\tau_{ij} - \frac{1}{3}\tau_{kk}\delta_{ij} = 2\mu_t\bar{S}_{ij} \tag{2}$$

where $\bar{S}_{ij} = \frac{1}{2}\left(\frac{\partial\bar{u}_i}{\partial x_j} + \frac{\partial\bar{u}_j}{\partial x_i}\right)$. Note that the over-bar denotes a time-average.

The eddy viscosity appearing in the SGS term of the WALE model (μ_t) is defined as

$$\mu_t = \left(\rho C_w V^{1/3}\right)^2 \frac{\left(S_{ij}^d S_{ij}^d\right)^{3/2}}{\left(\bar{S}_{ij}\bar{S}_{ij}\right)^{5/2} + \left(S_{ij}^d S_{ij}^d\right)^{5/4}} \tag{3}$$

where $S_{ij}^d = \left(\bar{g}_{ij}^2 + \bar{g}_{ji}^2\right)/2 - \delta_{ij}\bar{g}_{kk}^2/3$, $\bar{g}_{ij} = \partial\bar{u}_i/\partial x_j$, $\rho = 1$ for incompressible flow and $C_w = 0.325$.

This model was used because it resulted in good predictions of the wall stress and turbulent intensities as reported by Ducros et al. [32].

To investigate turbulent characteristic of the flow, the turbulence kinetic energy (TKE) and turbulence intensity were used. The TKE can quantified by the mean of the turbulence normal stresses which is defined as

$$\mathrm{TKE} = \frac{1}{2}\left(\overline{(u_1' u_1')} + \overline{(u_2' u_2')} + \overline{(u_3' u_3')}\right) \tag{4}$$

For steady laminar flow TKE is zero while the large value of TKE represents the existence of the turbulent flow phenomena.

The turbulence intensity is

$$\mathrm{TI} = \frac{u'}{U} \tag{5}$$

where $u' = \sqrt{\frac{2}{3}\mathrm{TKE}}$.

3.4. Numerical Solution

According to investigation of Johnstone et al. [4], the Reynolds numbers (Re') can be varied in a wide range ($650 < Re' < 13{,}000$), depending on inhalation flow rate, the local mean diameter and local bulk velocity (U_{local}). This range of changing Reynolds number implies laminar flow through transition and then into the fully turbulent flow. The Reynolds number for the ETA is defined as

$$Re' = U_{local}\frac{\sqrt{A_{local}}}{\nu} \tag{6}$$

This definition of Reynolds number was used for the simulation of the ETA to validate CFD solutions with experimental data [4], [11] and LBM results of Ball et al. [6]. Note that for this comparison the time-averaged solutions were run, corresponding to 5s in real time, for 5000 and 10,000 iterations in the low and high flow rates, respectively.

The computations utilized a quadratic reconstruction approach, and were solved in unsteady (time-accurate) mode utilizing 80 Newton subiterations to ensure second order temporal accuracy. Dual-time-stepping was used to enhance stability of the iterative solution process with a Courant-Friedrichs-Lewy (CFL) number in the range of 0.015 to 0.025.

Two breathing rates (7.5 and 15 breaths per minute) corresponding to the range of typical human breathing at rest were considered in this study. The transient breathing cases were simulated for four breathing cycle and utilized 31,872 iterations resulting in different time steps (Δt). Table 3.4.1 summarizes the various parameters that were used in these simulations. The Womersley number (α) [33] shown in the table is the ratio of the transient inertial force to the viscous force and is a significant nondimensional parameter in the study of transient flows. It is defined as

$$\alpha = D\sqrt{\omega/\nu} \tag{7}$$

where $\omega = 2\pi f$.

Table 3.4.1 Parameters for the breathing cycles considered in this study

Breathing Rate	T (seconds)	f (Hz)	α	Re	Δt (seconds)
7.5 breaths/minute	8	0.125	4.72	875	0.001004016064
15 breaths/minute	4	0.25	6.68	1750	0.000502008032

The constant inspiration and expiration simulations corresponded to the peak inspiration and expiration for the two breathing rates considered here (hereinafter referred to as $\alpha = 0$). They were carried out for 8,000 iterations and the resulting solutions were time-averaged over the last 3,000 time steps.

In these simulations, the Reynolds number defined as

$$\mathrm{Re} = \mathrm{U_{local}} D/\nu \tag{8}$$

3.5. Boundary Conditions

Humans have two lungs which consist of five lobes. Three lobes on the right and two on the left; right superior (RS), right middle (RM), right inferior (RI), left superior (LS), and left inferior (LI) bronchus. For the transient breathing cases, a sinusoidal waveform velocity profile was imposed at the distal lobar boundaries, i.e., $\overrightarrow{\mathrm{V}_{\mathrm{out}}} = \overline{\mathrm{V}}_{\mathrm{max}} \sin(\omega t) = \overline{\mathrm{V}}_{\mathrm{max}} \sin(\phi)$ while the pressure was allowed to float. To enforce the appropriate velocities at lobar boundaries, an expression for velocity as a function of the lobar volume $\Delta\nu_{\mathrm{lobe}}$ was written [24]:

$$\overline{\mathrm{V}}_{\mathrm{max}} = \omega \Delta\nu_{\mathrm{lobe}} / 2\mathrm{A}_{\mathrm{out}} \tag{9}$$

The values of $\Delta\nu_{\mathrm{lobe}}$, for each lobar bronchus are summarized in Table 3.5.1. Note that these boundary conditions are lobar-specific boundary conditions to generate the appropriate flow rate based upon the values reported by Horsfield et al.

Table 3.5.1 Lobar volumes in the lung

Lobe	RS	RM	RI	LS	LI	Total
Percentage of $\Delta\nu_{\mathrm{lobe}}$	21	9	25	20	25	100
$\Delta\nu_{\mathrm{lobe}}$ (L)	0.105	0.045	0.125	0.1	0.125	0.5

The velocity used for the constant inspiration/expiration cases matched the flow conditions at peak inspiration and expiration of the transient breathing cases, i.e. at phase angle of $\pi/2$ and $3\pi/2$, respectively. At the inlet boundary, a pure Dirichlet boundary condition was

used to keep static pressure fixed at standard atmospheric pressure while the velocities were allowed to float.

CHAPTER IV

RESULTS AND DISCUSSION

A discussion of the results obtained for all three geometries are presented in this chapter. Firstly, the ETA geometry was validated with experimental data and computational (LBM) simulation for a flow rate of 10 l/min using the SST turbulence model and LES which resulted in four simulations, i.e., simulations for coarse and fine mesh for each technique. Two LES simulations were performed for 30 l/min so that a comparison between the two flow rates could be carried out. A comparison of constant inspiration/expiration with the first transient breathing cycle was carried out for each flow rate and that resulted in six simulations. Excluding simulations of 30 l/min, there are total of ten simulations for the ETA geometry. Similarly, the simulations of the lower airway only and the entire airway geometry are presented for constant inspiration/expiration and four full transient breathing cycles resulted in six simulations for each geometry. Finally, comparisons between the constant inspiration/expiration and first transient breathing cycle simulations of all geometries were carried out. Overall, a total of twenty two simulations were conducted in this study.

4.1. The Idealized Upper Airway Geometry (the ETA geometry)

The comparison of LES simulation with PIV data and LBM is presented in the first part of the simulation of the ETA. In the second part, transient breathing cycle simulations are compared with corresponding inspiration/expiration simulations.

4.1.1. Validation with Experimental Data and Computation Simulations

The local coordinate system used here is the same as the one used by Johnstone et al. [4] and Ball et al. [6]. As depicted in Figure 4.1.1, the coordinate system is defined in the sagittal plane. x is defined along the direction of the probe, y is perpendicular to the x-direction (in the direction of the flow) and z is perpendicular to the sagittal plane. The origin of the coordinate system is on the superior (inlet and cross-sections 1 to 4) or posterior wall (cross-sections 5 to 7) in the sagittal plane of the ETA (Figure 4.1.2). Note that these cross-sections are the measuring locations that were used by Johnstone et al. [4].

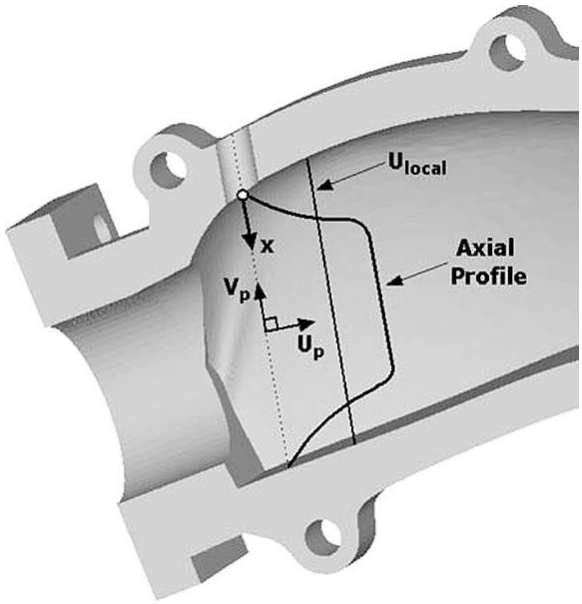

Figure 4.1.1 Local coordinate systems from Johnstone et al. (2004)

As mentioned in Chapter 3, the geometry utilized in this study is not the original geometry and has been reconstructed based on available papers in the literature. Therefore, some deviations from the geometry used in the experiments can be expected. The investigation was

carried out by comparing the results of the LES simulation with hot-wire anemometry data [11], [4] as well as direct numerical simulation i.e., LBM [6], at seven cross-sections (see Figure 4.1.2) for the flow rate 10 l/min.

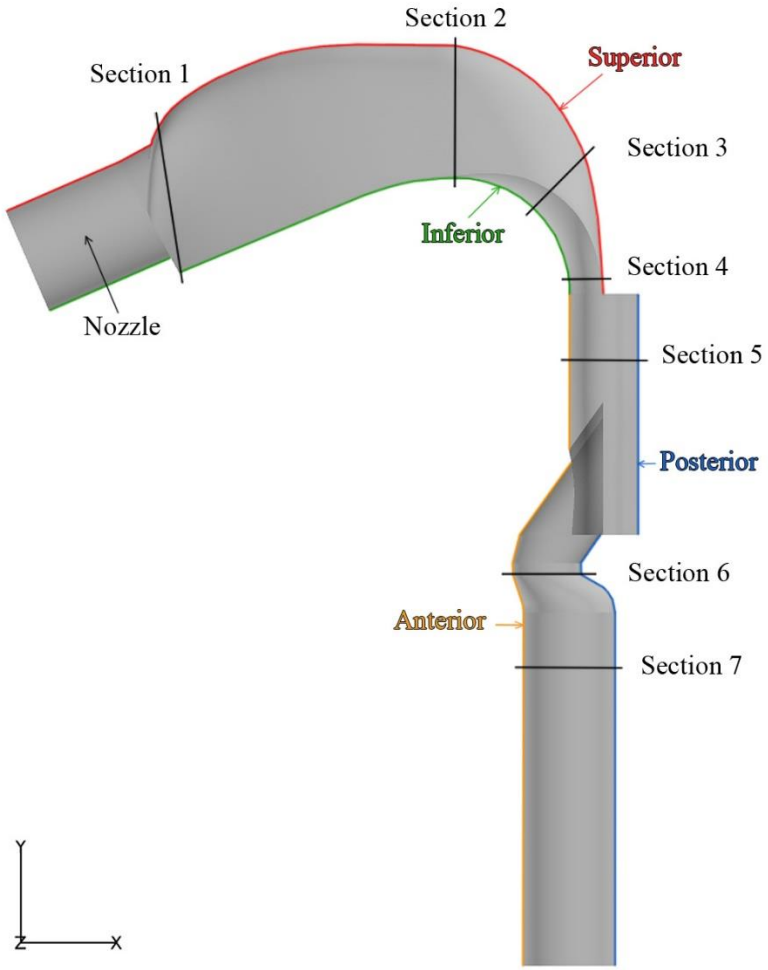

Figure 4.1.2 Seven traverse cross-sections illustrated in sagittal plane of the ETA

Simulations were carried out for two grids (coarse and fine gird as summarized in Table 3.2.1), but for comparison solutions of the coarse mesh were utilized, because no significant differences were observed between these two grids. This will be discussed at end of this section.

The contour plot of the time-averaged LES solution in central sagittal plane for flow rates of 10 and 30 l/min are shown in Figure 4.1.3. Generally, the same structure of the flow can be observed for both flow rates. The difference is in the strength of the flow that is clearly visible in the length of laryngeal jet within the trachea. Therefore, the comparisons of time-averaged velocity profiles and flow structures through the ETA with experimental and computational results (LBM solutions) were carried out only for 10 l/min.

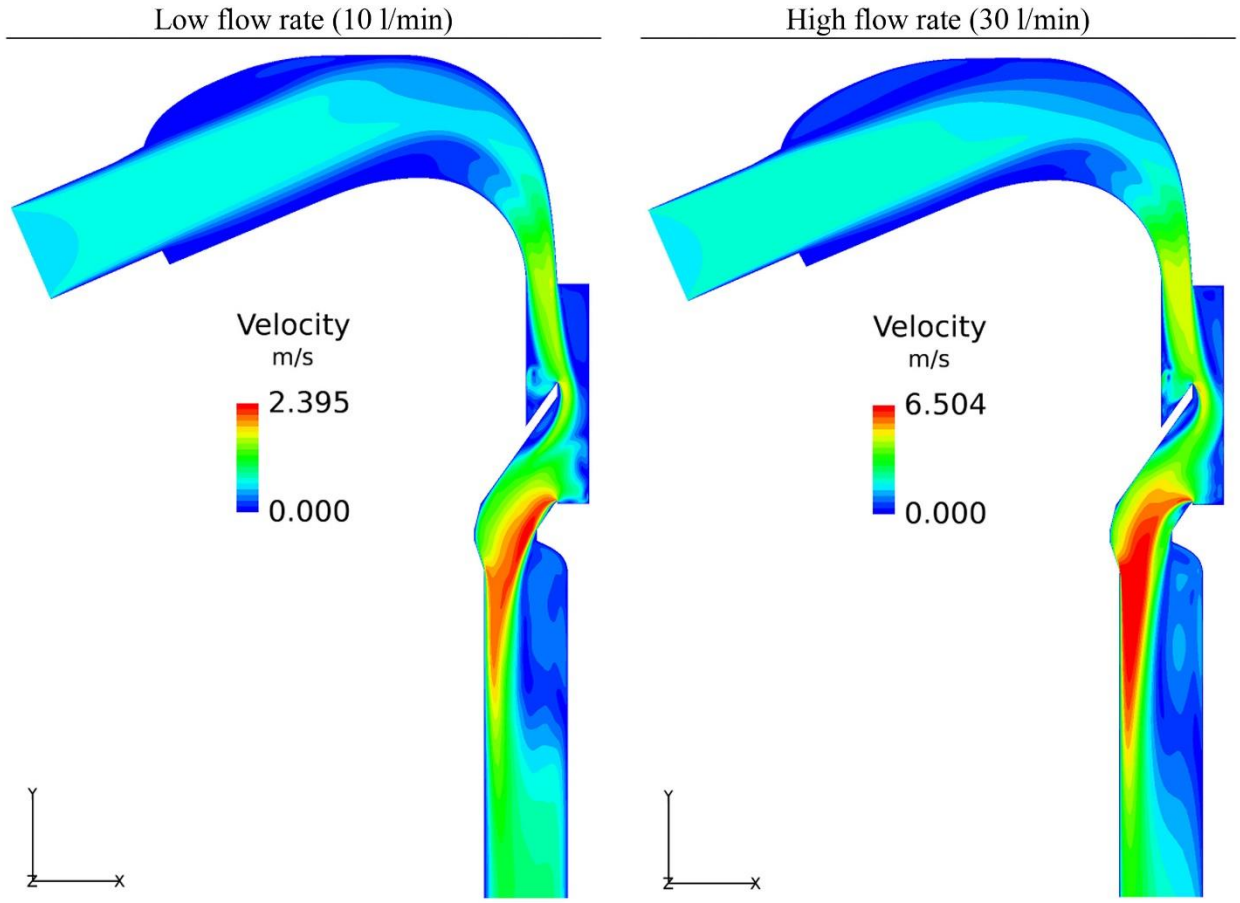

Figure 4.1.3 Contour plot of the central sagittal plane of the ETA, colored with the velocity magnitude, for flow rate 10 and 30 l/min

4.1.1.1. Cross-Section 1

The presence of the nozzle results in a fully developed flow at the entrance of the oral cavity. This can clearly be seen in the velocity profile of the first cross-section in Figure 4.1.4. Cross-section 1 is located at the inlet of the oral cavity, right after the first backward facing step, i.e. the upper and the lower teeth, downstream of the straight pipe nozzle (see Figure 4.1.2).

A comparison of the computed velocity profile to experimental data [4] and LBM computations [6] are shown in Figure 4.1.4. The overall trend of the computed velocity profile is consistent with the experimental data as well as the LBM results. The top-hat shaped region $6 \leq x \leq 19$ is visible in both sets of experimental data; however, the computations have bumps at the beginning and the end of the top hat regions, i.e., at $x \approx 7$ and 19 mm. In the LES profile, the bump on the right side is much more pronounced compared to the LBM results. These effects are due to the existence of the recirculation bubbles appeared in superior and inferior regions of the oral cavity. Given that this ETA geometry was reconstructed using cross-sections from the literature, the overall agreement is deemed acceptable.

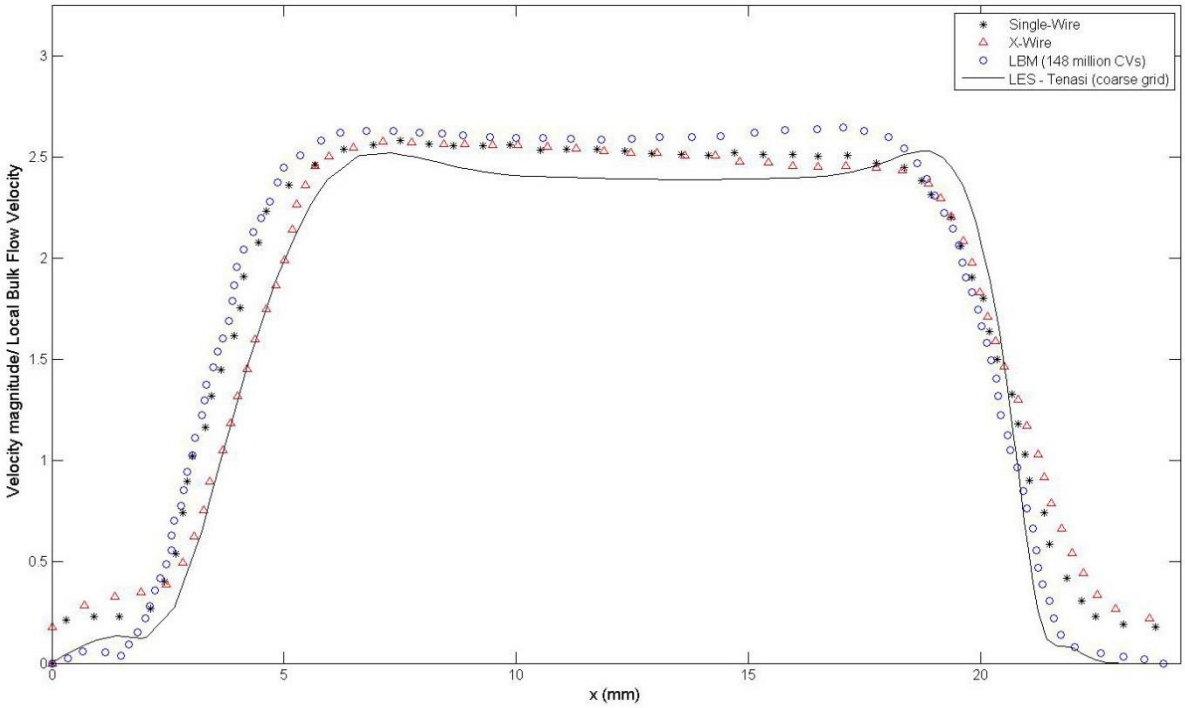

Figure 4.1.4 Velocity profile at Cross-Section 1, 10 l/min

4.1.1.2. Cross-Section 2

Cross-section 2 is located in the middle of the oral cavity, upstream of the oro-pharynx, as depicted in Figure 4.1.2. The comparison of the velocity profiles is shown in Figure 4.1.5. In contrast to Cross-section 1, the LBM results from [6] show poor agreement with the experimental data. In contrast, the LES results from *Tenasi* show better agreement with experimental data. However, the deviations of the predicted velocity profile from experiment are clearly visible, especially within $10 \leq x \leq 15$mm.

The complex nature of the flow field in the oral cavity can be seen in the instantaneous solution shown in Figure 4.1.6. Recirculation bubbles caused by the backward facing steps (upper and the lower teeth), can be seen in the instantaneous LES solution. The impact of the

recirculation zone on the flow field created by backward facing step at the inferior region of the oral cavity was not found to be significant. This conclusion was drawn based on visualization (animation) of the unsteady flow solution.

The secondary flow of the cross-section 2, depicted in Figure 4.1.7, shows the complexity of the flow phenomena in this region. Because of the construction of the oral cavity, two counter rotating vortices appear near the inferior wall of the oral cavity which was also observed in experiment and computational results (see [4], [5]).

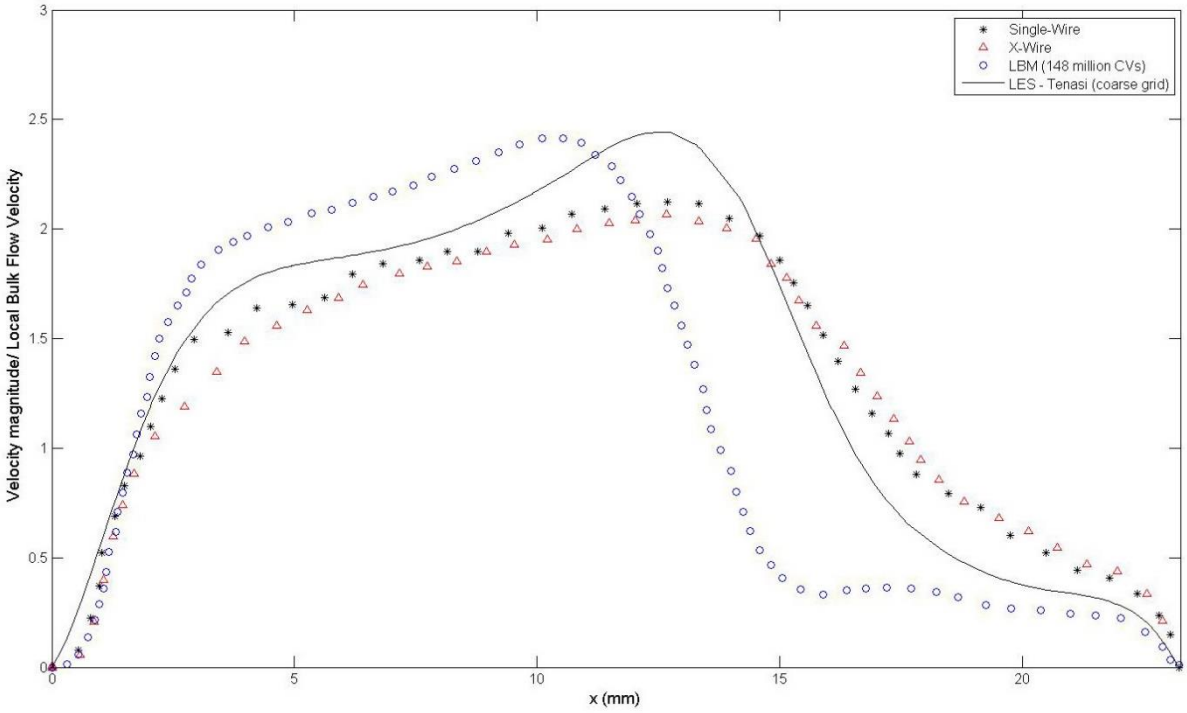

Figure 4.1.5 Velocity profile at cross-section 2, 10 l/min

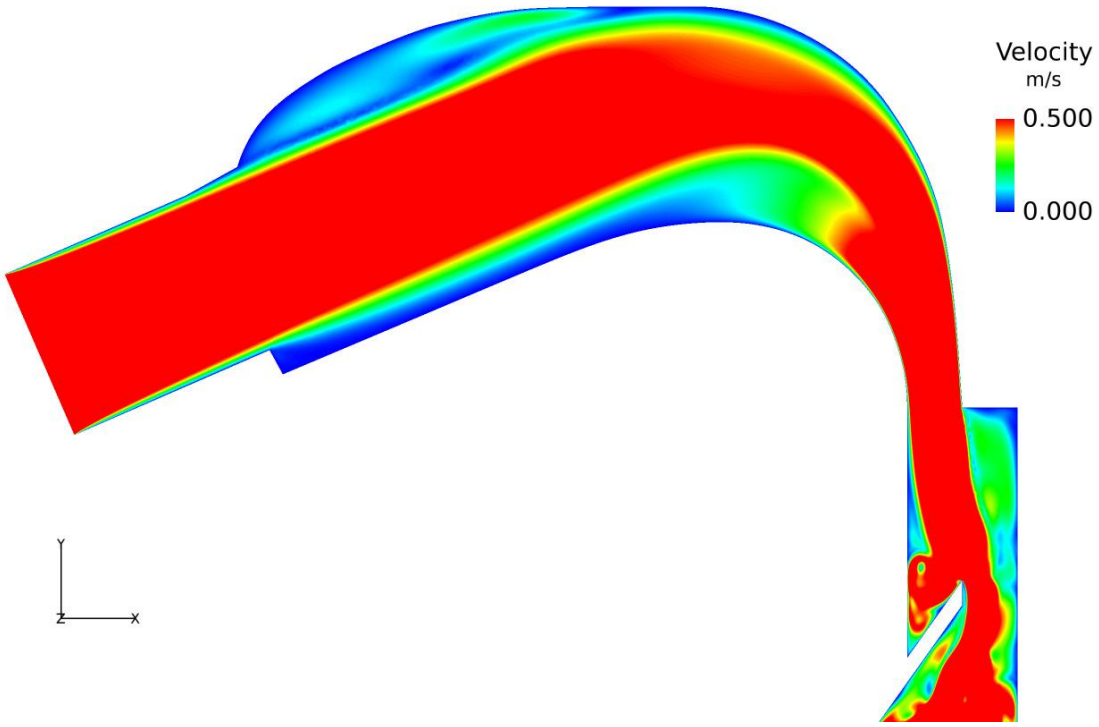

Figure 4.1.6 Contour plot of instantaneous solution in the central sagittal plane of the oral cavity in the ETA. The color spectrum of velocity magnitude is limited to range 0 to 0.5 m/s, 10 l/min

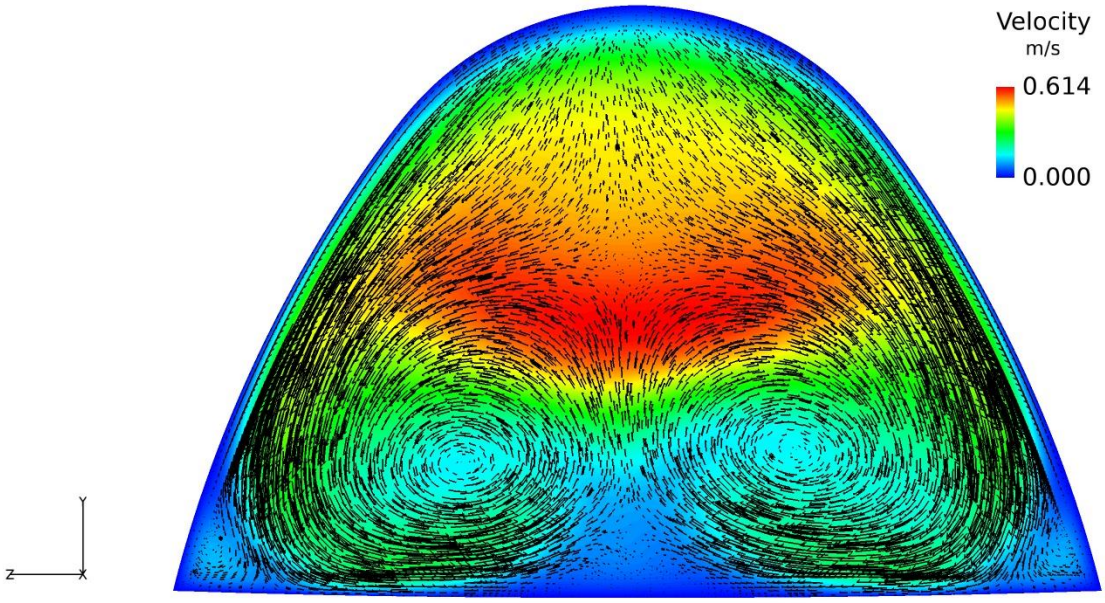

Figure 4.1.7 Secondary flow of LES solution at cross-section 2, 10 l/min

4.1.1.3. Cross-Section 3

The flow features entering the pharynx were affected by the curvature of the oro-pharynx. The flow accelerates as the cross-sectional area of the oro-pharynx is reduced. Cross-sections 3 and 4 are located in this region. This curvature generates Dean-like flow vortices, as can be seen in Figure 4.1.8. Dean-like flow instabilities occurs in the study of the flow in curved pipes or channels and are used for the measurement of the magnitude of the secondary flow [34]. In this region, they arise from a centrifugally-induced pressure gradient, which drives the slower moving fluid near the walls towards the center of the oral cavity, while the faster fluid is swept toward the walls. The two counter rotating vortices visible in this cross-section have already been observed in cross-section 2. From the velocity profile of the cross-section 3, depicted in Figure 4.1.9, two peaks in the velocity magnitude profile are clearly visible in LES as well as experimental and LBM results. LES solution reveals higher velocity values within $2 \leq x \leq 7\text{mm}$ compared to experimental data. Discrepancy of the results was also observed in LBM simulations (Ball et al. [6]) and those utilizing different RANS turbulence models (Ball et al. [5]). This discrepancy between the experimental and computational results reported by Ball et al. is due to the possibility of the errors in hot wire measurements. LES solution shows poor prediction of the airflow at this location, though the overall trends are similar to that of the LBM simulations. The reasons for these discrepancies could be a combination of errors in the experimental measurements and differences resulting from the construction of the geometry utilized in this study.

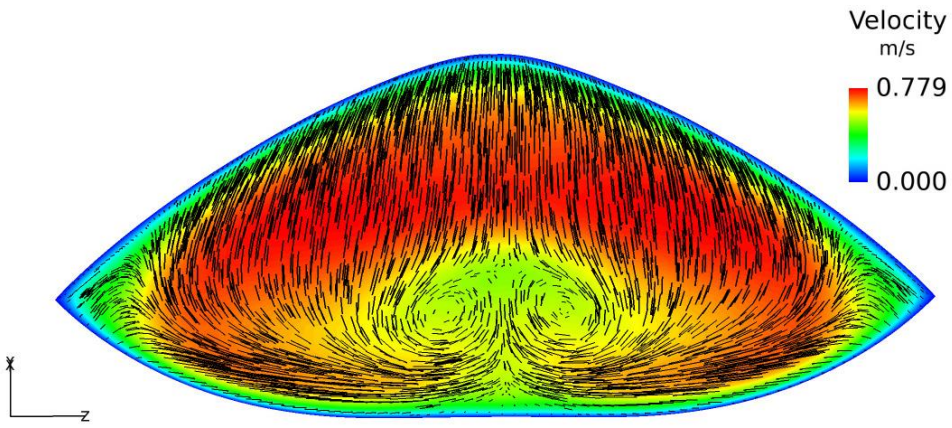

Figure 4.1.8 Secondary flow of LES solution at cross-section 3, 10 l/min

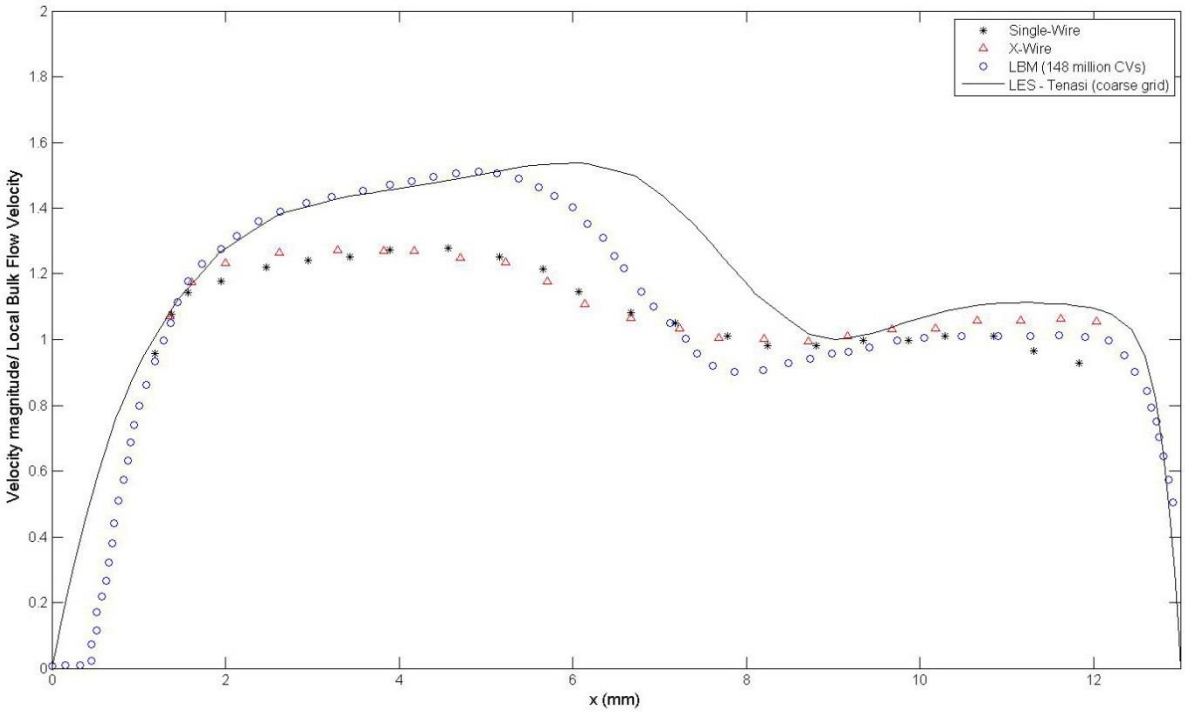

Figure 4.1.9 Velocity profile at cross-section 3, 10 l/min

4.1.1.4. Cross-Section 4

Cross-section 4 has the smallest cross-sectional area in the oro-pharynx. Hence, higher flow velocities are expected in this location where the flow is accelerated downstream of the oro-pharynx. The velocity profiles of LES in this cross-section were remarkably close to both experimental and computational results, as depicted in Figure 4.1.10. The trend of the top-hat shaped velocity profile of LES results was much closer to the single-wire, while the velocity profile of LBM is close to X-Wire. Figure 4.1.11 illustrates secondary flow of LES solution for flow rate 10 l/min and instantaneous secondary flow visualization for 60 l/min from Johnstone et al. at cross-section 4. The higher flow rate (experimental data) shows the presence of two strong counter-rotating vortices, while the lower flow rate (computational simulation) does not show the same. This computational result is in line with those reported by Ball et al. [6] using LBM solution. Johnstone et al. suggested much stronger vortices for higher flow rates which caused flow separation at the anterior region of the oro-pharynx.

In order to identify complex flow structures in the critical regions of the ETA, the Q-criterion is used. Q-criterion is defined as the second invarient (Q) of the velocity gradient tensor (∇u) [35]. A visualizaton of the Q-criterion, colored by velocity magnitude, is shown in Figure 4.1.12. From this figure, two vortices can be observed along the inferior wall of the oro-pharynx.

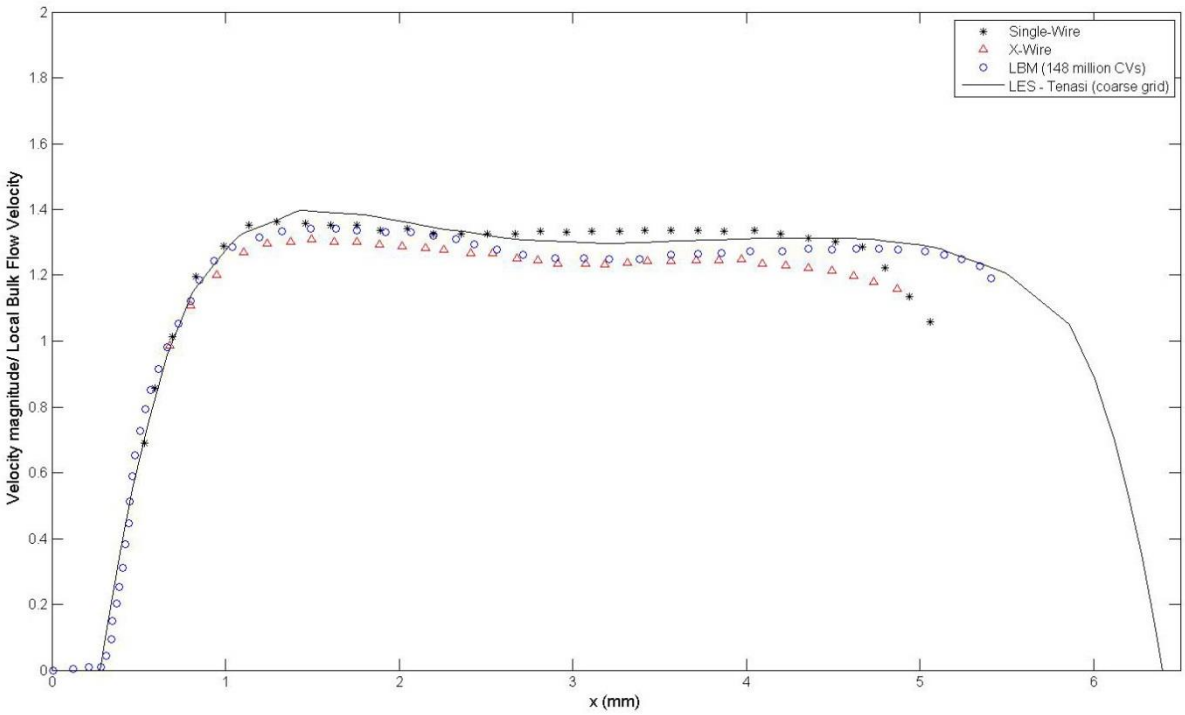

Figure 4.1.10 Velocity profile at cross-section 4, 10 l/min

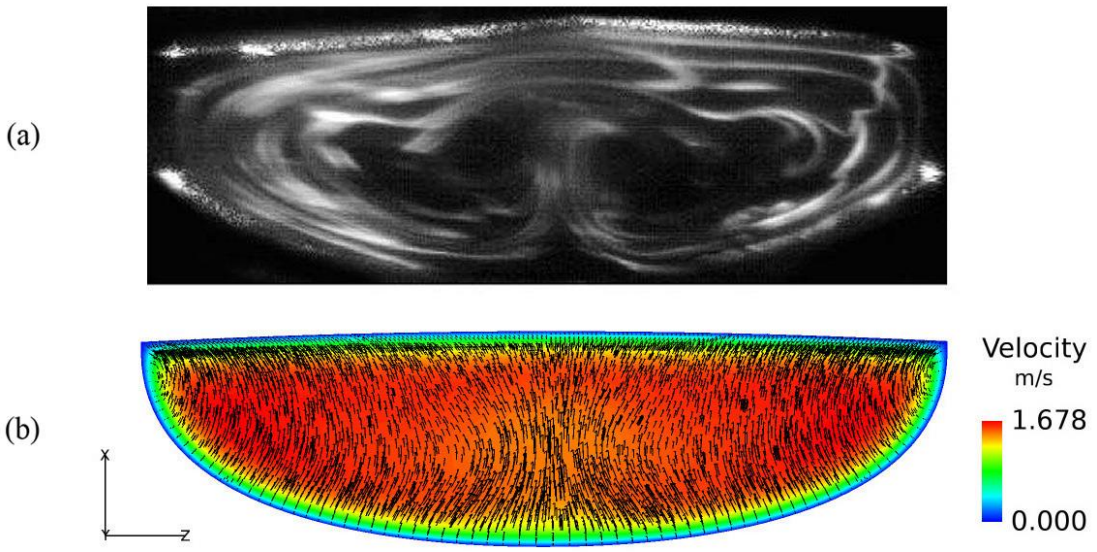

Figure 4.1.11 a) Instantaneous secondary flow visualization for 60 l/min from Johnstone et al. b) Secondary flow of LES solution at cross-section 4, 10 l/min

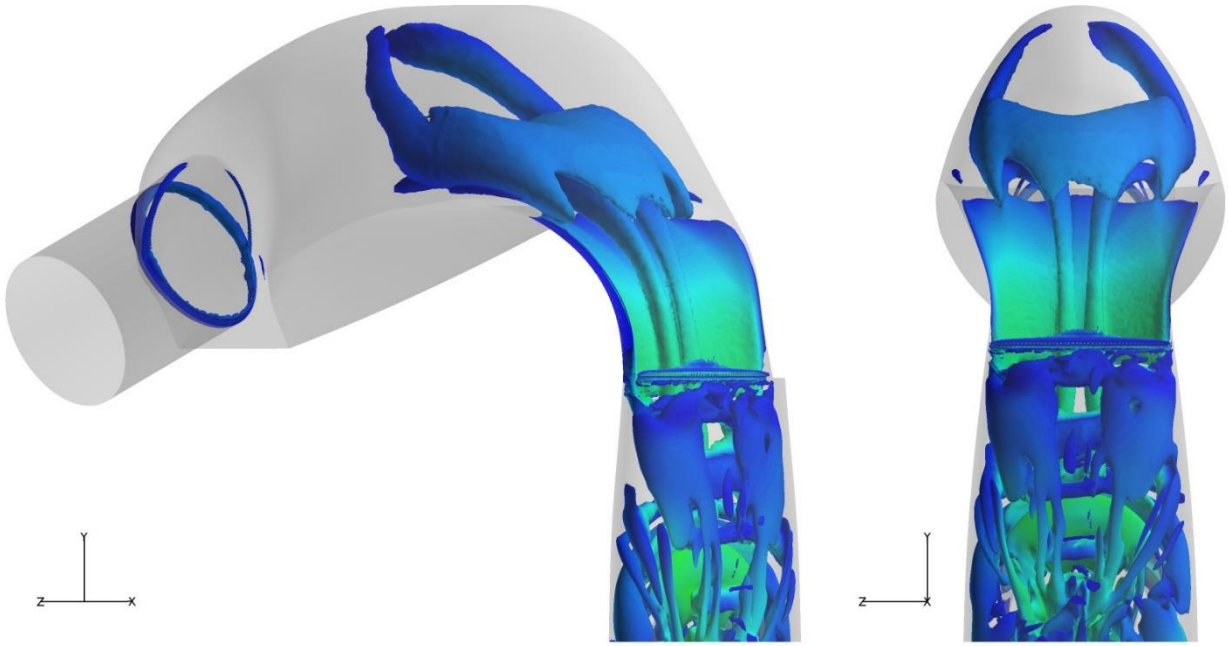

Figure 4.1.12 Iso-surface of Q-criterion colored by velocity magnitude, 10 l/min. Posterior and oblique (45°) of the oral-cavity and oro-pharynx from right to left. The geometry is in gray

4.1.1.5. Cross-Section 5

Figure 4.1.13 shows the complexity of the flow features in the pharynx. This figure illustrates the comparisons of time-averaged solution of LES and LBM for flow rate 10 l/min. However, LES predicted all basic features that can be seen in LBM results, discrepancies in the velocity values are still visible. The recirculation zone in LES solution is bigger than the LBM. This recirculation bubble appeared in the pharynx due to the second backward facing step where the inlet of naso-pharynx is. The presence of the epiglottis caused the separation from the anterior wall of the pharynx.

A better insight into the flow phenomena in the pharynx can be achieved from cross-section 5. Comparisons of the velocity profiles at cross-section 5 are displayed in Figure 4.1.14. The trend

of the velocity profile of LES was remarkably close to the X-Wire of the experimental data; however, it can be seen that the velocity values of LES simulations were lower than experiment in the region $6 \leq x \leq 9$mm. The peak in the velocity profile is the result of the jet-like flow entering the pharynx. Furthermore, there is noticeable difference between computational (LES and LBM) solutions and experimental results within a top-hat type region i.e.$0 \leq x \leq 4$mm. Johnstone et al. [4] reported that hot-wire probes provided unreliable results due to the reverse flow in the recirculation zone. Overall, it can be said that there is a good agreement between LES and other results.

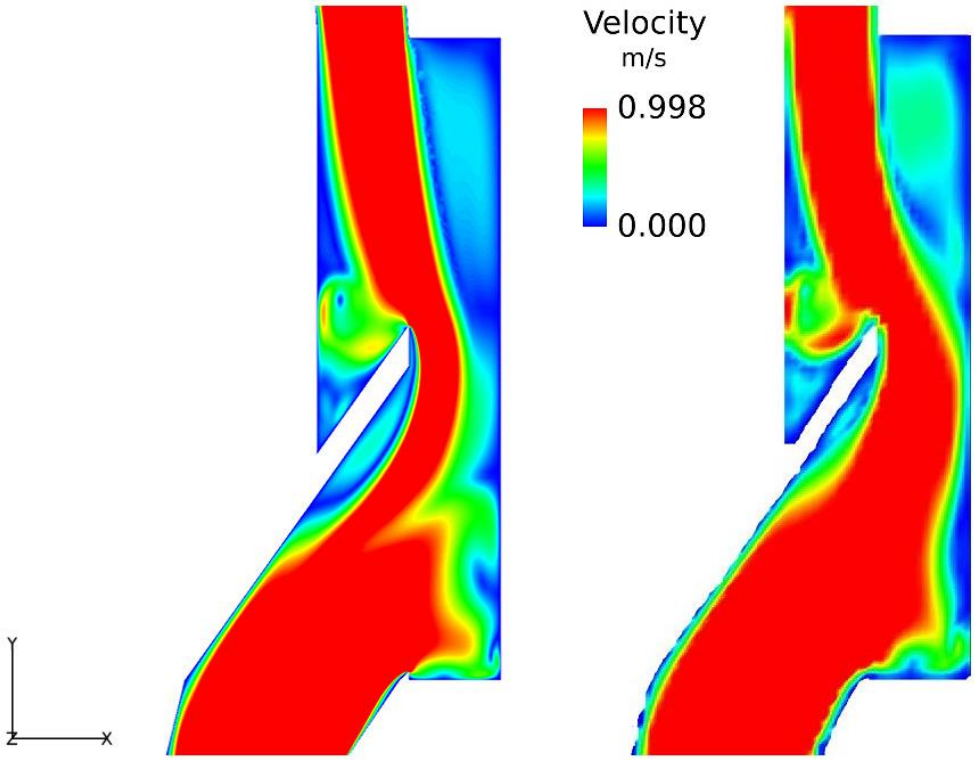

Figure 4.1.13 Velocity contours plot of the central sagittal plane of the pharynx. LES (*Tenasi*) and LBM (from Ball et al.) displayed on the right and left, respectively. The color spectrum of velocity magnitude is limited to range 0 to 0.9976 m/s, 10 l/min

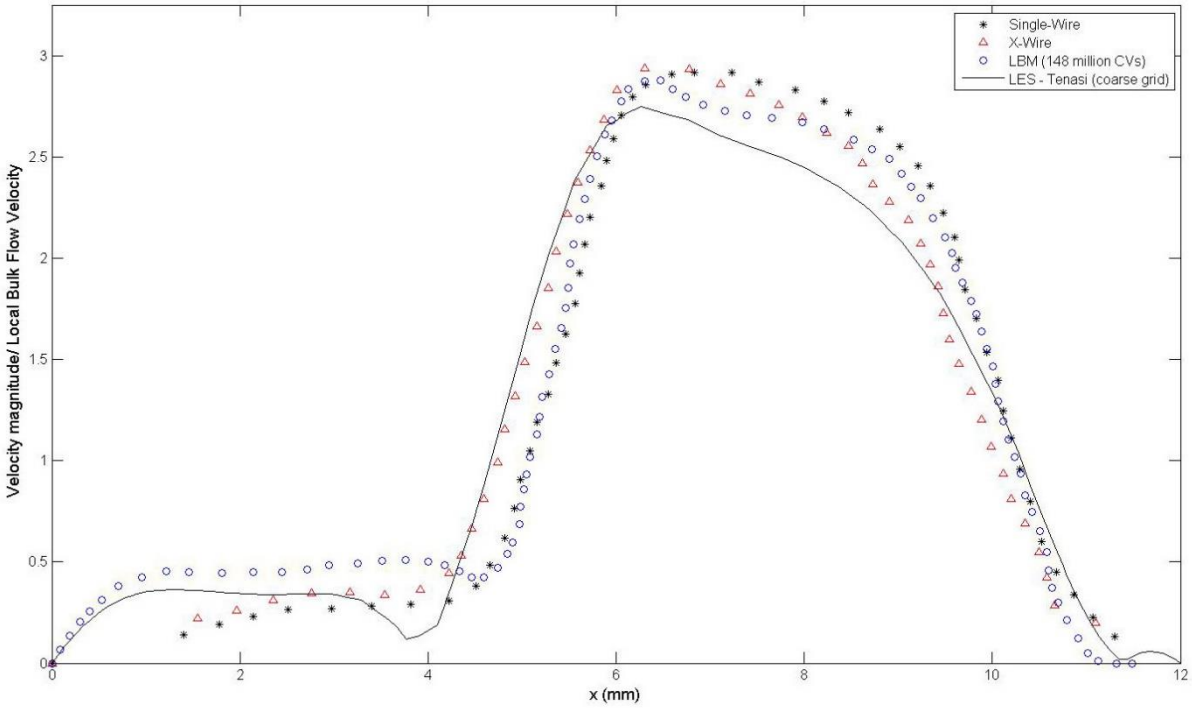

Figure 4.1.14 Velocity profile at cross-section 5

Figure 4.1.15 depicted the secondary flow at cross-section 5 at a flow rate 10 l/min. Two strong vortices can be observed near the posterior wall of the pharynx. The presence of the epiglottis downstream of the cross-section 5 caused the recirculation region and also separation at the anterior wall of the pharynx, as can be seen in Figure 4.1.13. In a realistic human ETA, the epiglottis prevents the food and other matter from entering the lower airway, while in this idealized geometry it is considered to be conical tube. This is caused by a vortex that is convected around the epiglottis, as can be observed in Figure 4.1.16. At the entrance of the larynx, a small separation region was formed on the lower side of the epiglottis that can be seen in Figure 4.1.13.

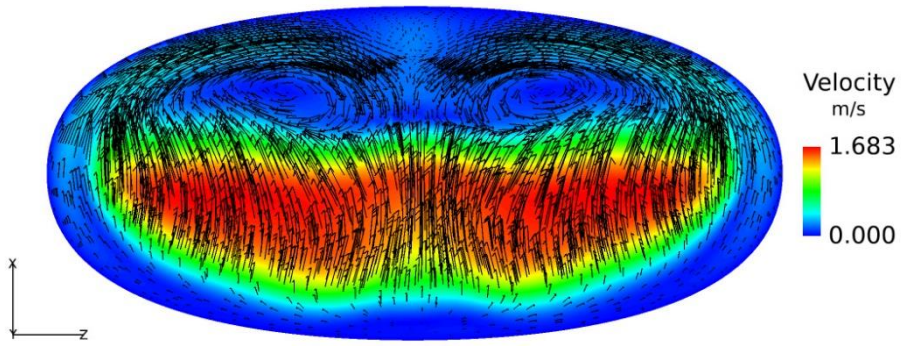

Figure 4.1.15 Secondary flow of LES solution at cross-section 5, 10 l/min

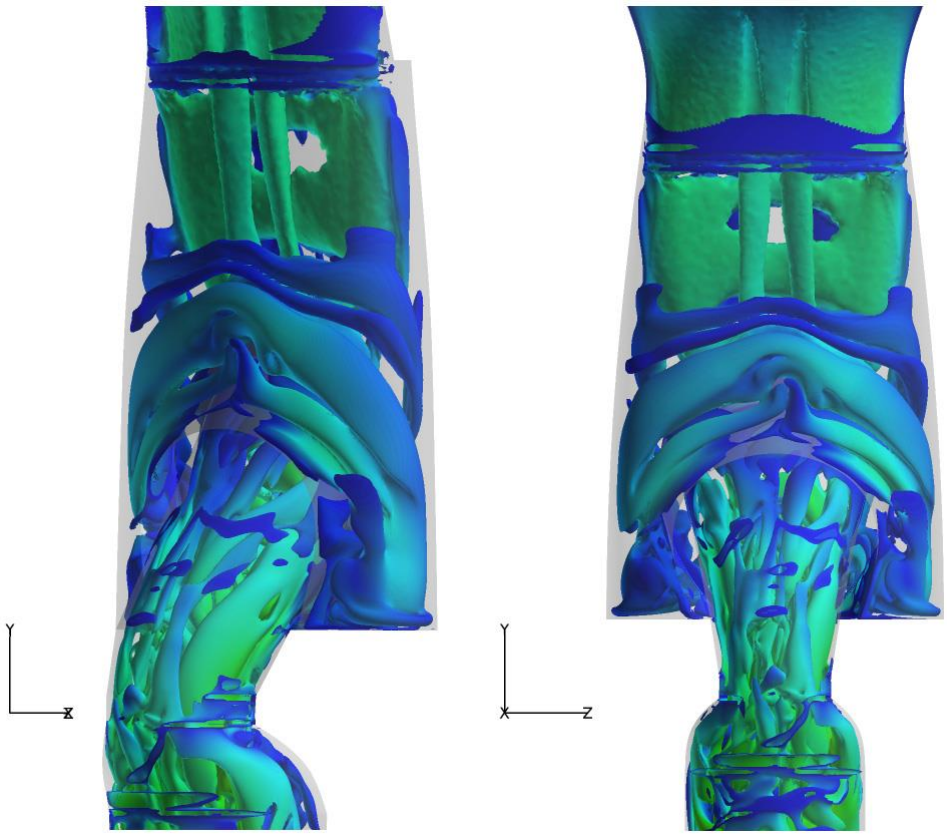

Figure 4.1.16 Iso-surface of Q-criterion colored by velocity magnitude, 10 l/min. Anterior and oblique (45°) of the pharynx and larynx from right to left. The geometry is in gray

4.1.1.6. Cross-Section 6

Because of the construction of the larynx and small cross-sectional area at cross-section 6, the flow accelerated, pushed the flow toward the anterior wall of the trachea and created a jet-like flow that is known as laryngeal jet. This acceleration was almost three times higher than velocity at the inlet (for 10 l/min case). This flow phenomenon can clearly be seen in both LES and LBM solutions for flow rate 10 l/min, as depicted in Figure 4.1.17. However, the same strength of the laryngeal jet can be observed in both solutions, it seems that the recirculation bubble in the posterior region of the LES simulation is larger than the one in the LBM simulation. Cross-section 6 is located at the high-speed region of the larynx, where the jet-like flow occurred (see Figure 4.1.2). The velocity profiles of the LES show good agreement with respect to experiments as well as LBM. The velocity profiles at this cross-section are plotted in Figure 4.1.18. In this plot, a slight negative slope in both experimental and LBM results can be seen while LES showed nonlinear slope within 3 to 5 mm. This might be because of the time-averaging that requires to be considered for more than 5 seconds in real time. As previously mentioned, these differences in LES solution may also be due to the possibility of the errors in the construction of the utilized geometry.

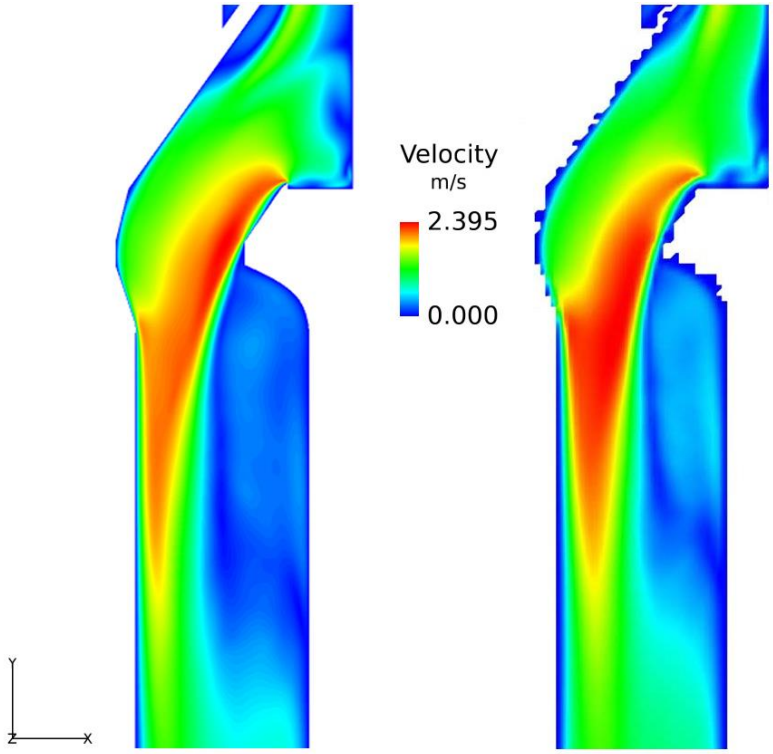

Figure 4.1.17 Central sagittal plane of the velocity contour, illustrating the larynx and trachea. LES (*Tenasi*) and LBM (from Ball et al.) on the left and right, respectively, 10 l/min

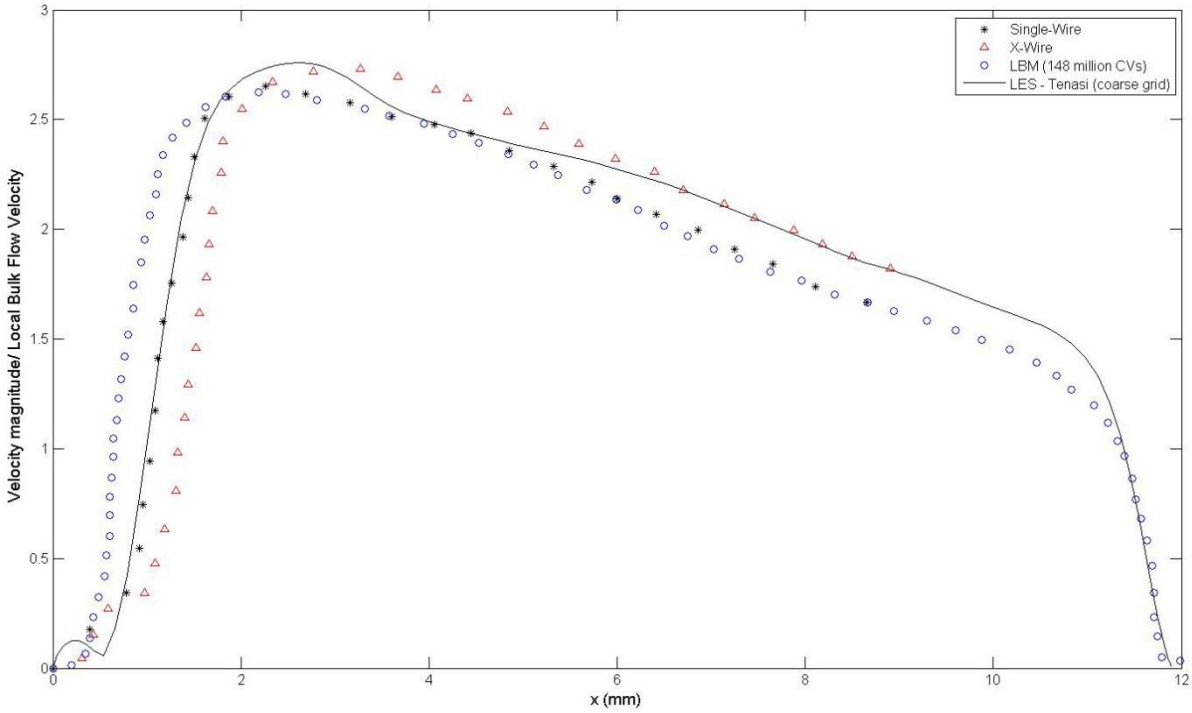

Figure 4.1.18 Velocity profile at cross-section 6, 10 l/min

4.1.1.7. Cross-Section 7

Right after the cross-section 6, the area in the larynx expanded to a circle pipe and it continues down toward the outlet. The third backward facing step caused a recirculation zone in the posterior wall of the trachea. This flow feature can be seen in Figure 4.1.17. In this figure, the velocity contour of LES is depicted against LBM. Some deviations between both numerical solutions can be observed. The laryngeal jet in LES was a little bit closer to the anterior wall of the trachea compared to LBM. This deviation is clearly visible in velocity profiles of the cross-section 7 in Figure 4.1.19. Significant differences observed between LES as well as LBM results within $8 \leq x \leq 14\text{mm}$. This shows a poor prediction of the airflow in both numerical methods. As describe earlier, these errors in LES might be related to the geometry. Moreover, notice that similar to cross-section 5, Johnstone et al. reported dropout data for experimental measurements in this cross-section. Due to the existence of the reverse flow in $0 \leq x \leq 8\text{mm}$, experimental results were suspected as untrustworthy in this region.

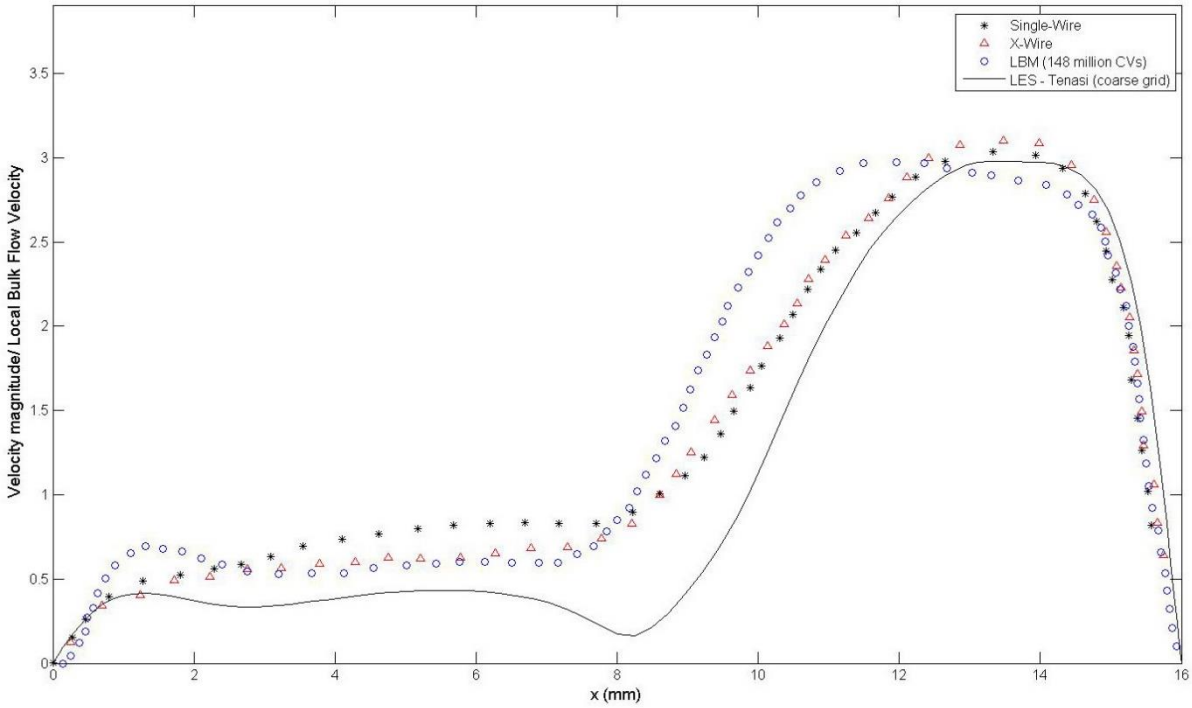

Figure 4.1.19 Velocity profile at cross-section 7, 10 l/min

The flow structure was observed to be fully turbulent in the larynx and consequently through the trachea. This turbulent flow phenomenon can be observed in iso-surface plot of Q- criterion in Figure 4.1.20.

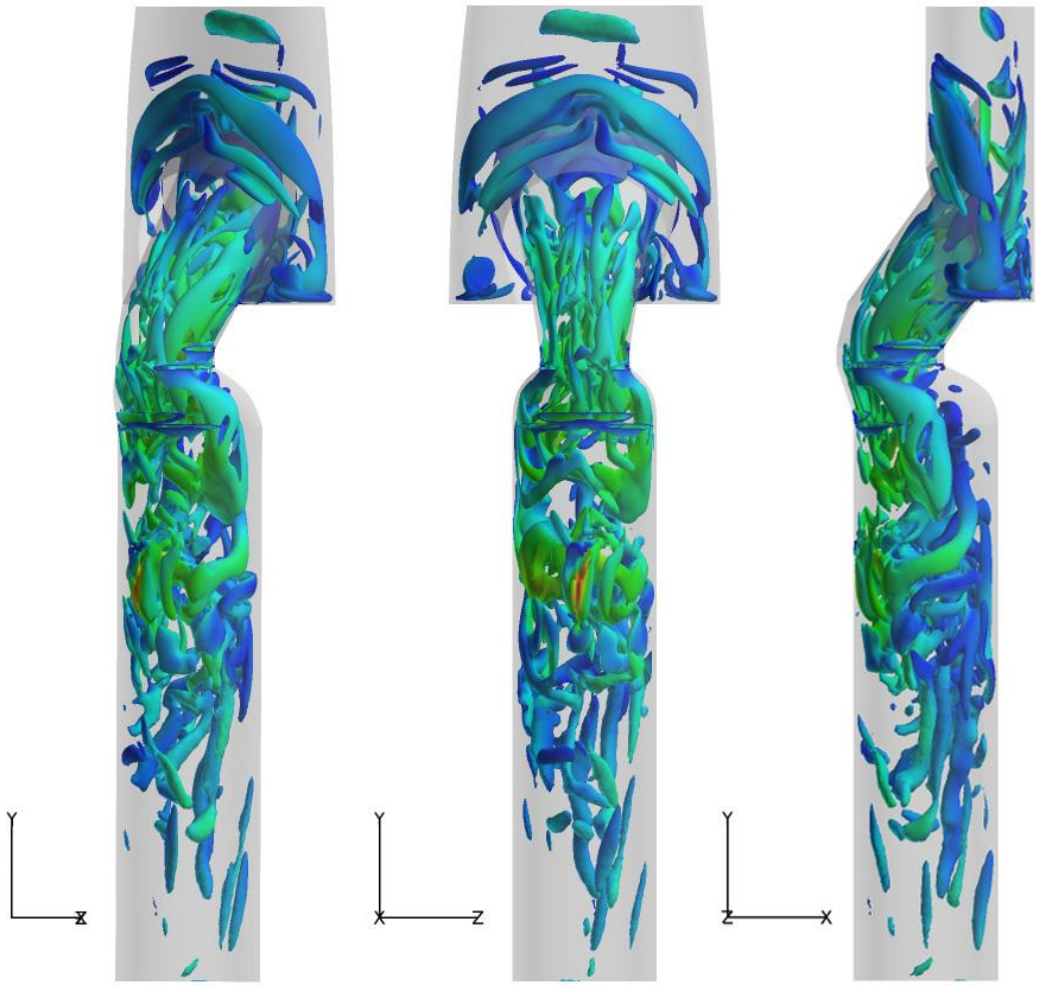

Figure 4.1.20 Iso-surface of Q-criterion colored by velocity magnitude, 10 l/min. Oblique (45°) view, coronal view and sagittal view of the pharynx and larynx from left to right. The geometry is in gray

4.1.1.8. Outflow

The three-dimensional velocity profile at the outlet of the trachea was previously reported by Johnstone et al. [4]. They also concluded that the realistic inlet boundary conditions in the trachea should be considered instead of uniform, parabolic or top-hat type velocity profile in the study of the pulmonary airway in order to obtain realistic results through the lungs. The experimental measurements were not carried out in this location, but the comparison can be

made against LBM from the result of Ball et al. [6], as depicted in Figure 4.1.21. The existence of the jet-like flow in LES was more pronounced than LBM within $10 \leq x \leq 14\text{mm}$. The velocity in the central region of LES solution suggested lower values compared to the LBM.

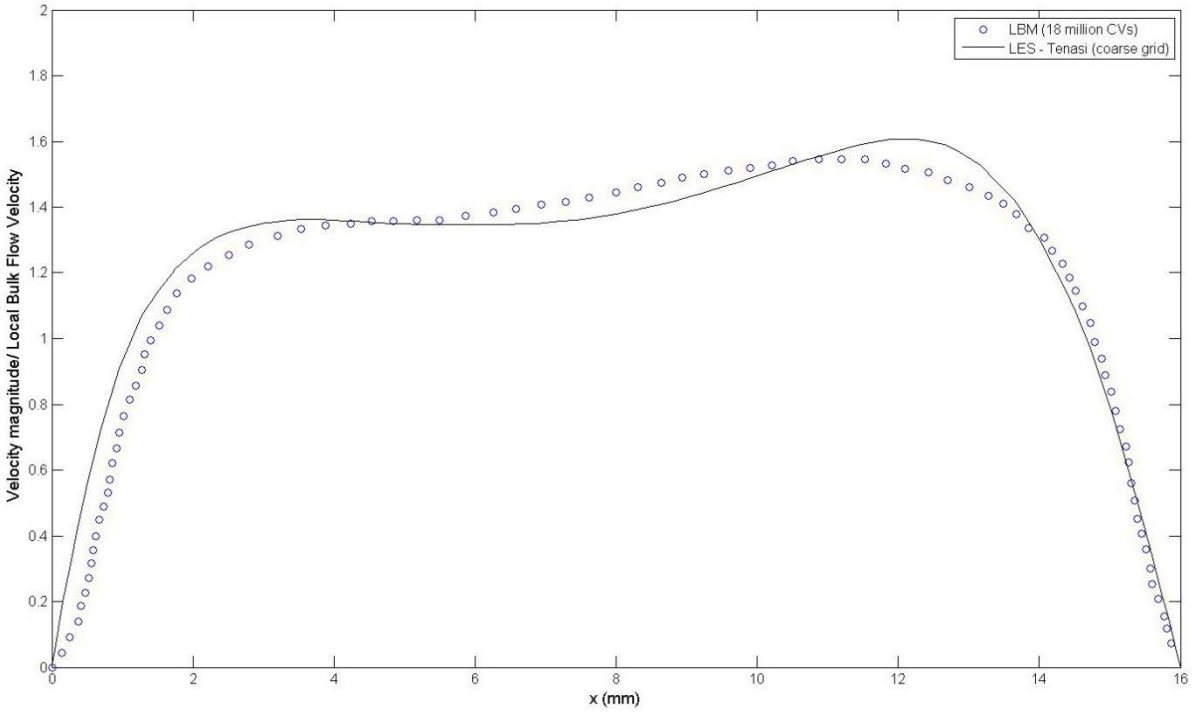

Figure 4.1.21 Velocity profile at the outlet, 10 l/min

Johnstone et al. warned about the possibility of errors in their data measurements at certain cross-sections. Thus, discrepancy between PIV data and CFD solutions could be notable. They also mentioned that more errors would be expected for higher flow rates. These errors in PIV results were due to data drop out, unresolved binormal velocities in Hot Wire measurements, probe disturbance and resolution.

The values of the local Reynolds number, i.e. Re', and local bulk velocities U_{local} at the inlet and all seven cross-sections (see Figure 4.1.2) were compared against the PIV [4] and LBM [6] in Table 4.1.1. The most differences of the local Reynolds number can be found at cross-section 2 and 5 with 8% and cross-section 6 with 10.5%. This shows a reasonable agreement of the reconstructed geometry with the original experimental geometry.

Table 4.1.1 Comparison of the local Reynolds number and local bulk velocity (U_{local}) between PIV data, the LBM and LES solutions at the inlet and seven cross-sections

Sections	PIV results (Johnstone et al.)	LBM solution (Ball et al.)		LES solution (Coarse mesh)	
	Re	U_{local}	Re	U_{local}	Re
Inlet	674	0.587	677	0.58632	675.474
1	483	0.291	477	0.31851	518.922
2	480	0.275	464	0.31151	522.217
3	716	0.542	651	0.55048	688.477
4	1052	1.178	960	1.35403	988.884
5	699	0.623	698	0.68282	758.9313
6	1073	1.368	1034	1.61969	1198.337
7	805	0.778	780	0.85325	827.9199

Figure 4.1.22 to Figure 4.1.28 illustrate the comparison of SST and LES solutions of coarse and fine mesh from *Tenasi* along with experimental results for flow rate 10 l/min. The overall agreement between the various solutions is quite similar, though there are some significant differences. For cross-section 2, the fine grid LES solution has much better agreement with experimental data than either the coarse grid LES or both the SST solutions, though all the solutions over predict the peak velocity at that cross-section. Overall, the fine grid LES solution has better agreement with the experimental data, while the sensitivity of the RANS (SST) solutions to grid density does not seem to be that high.

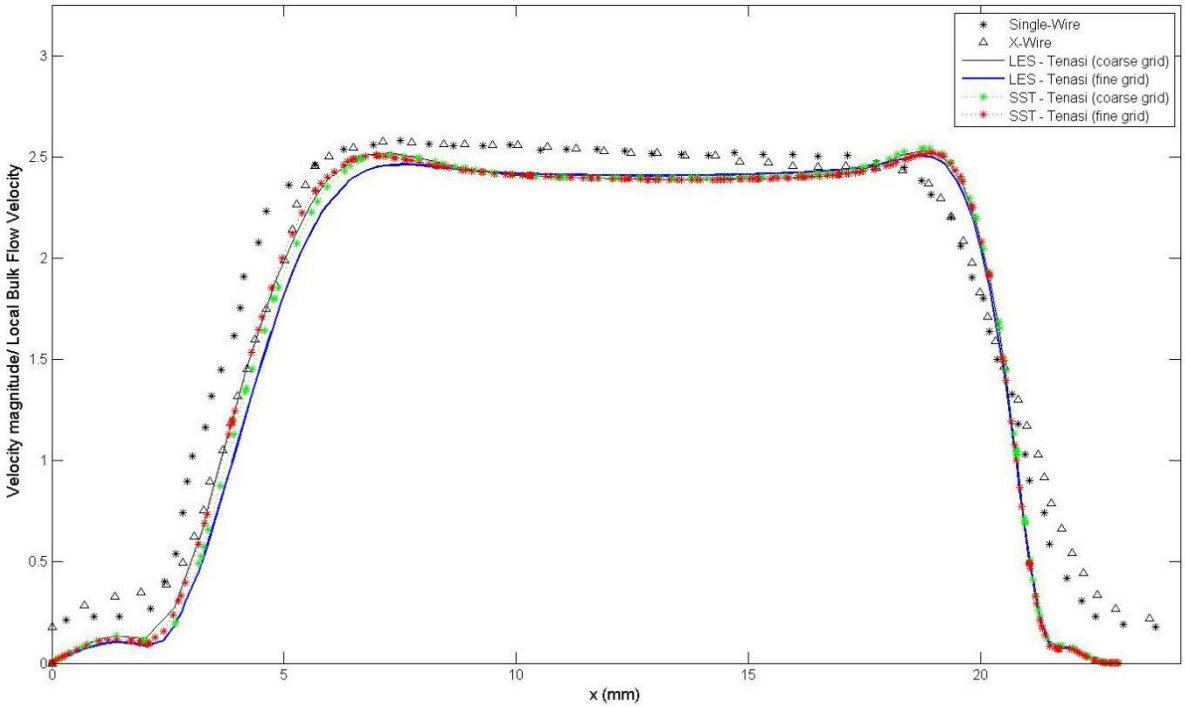

Figure 4.1.22 Comparison of SST and LES solutions of coarse and fine mesh from *Tenasi* with experimental results from Johnstone et al. at cross-sections 1

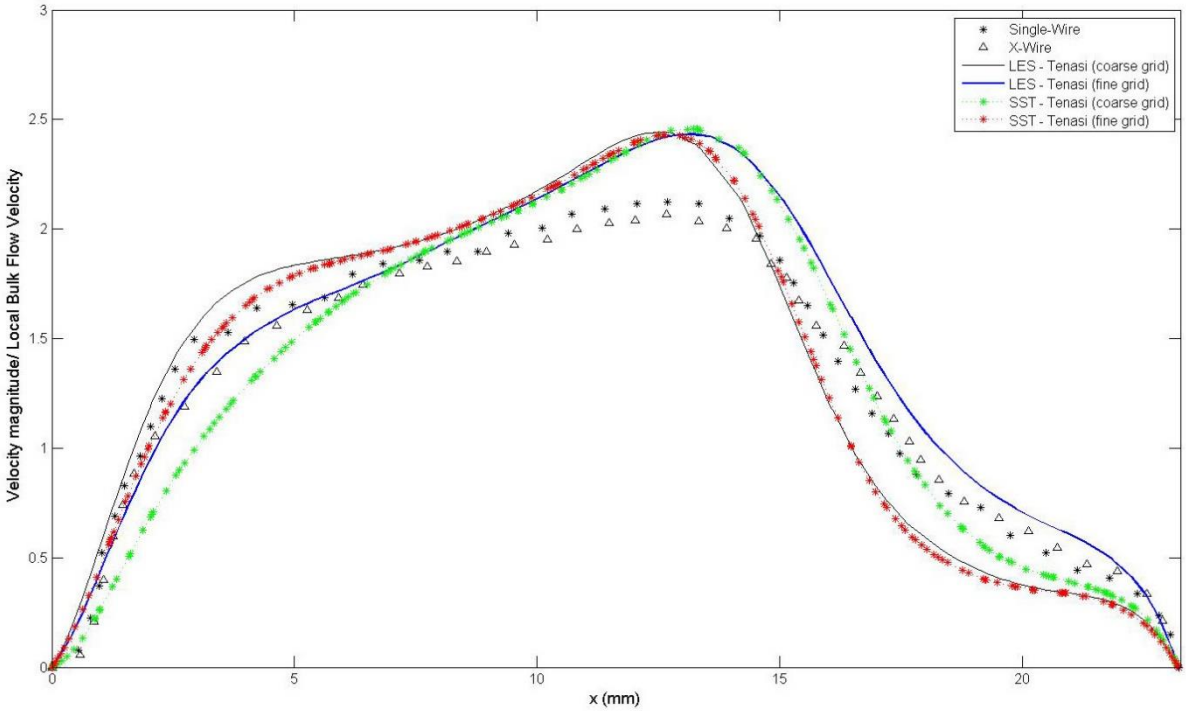

Figure 4.1.23 Comparison of SST and LES solutions of coarse and fine mesh from *Tenasi* with experimental results from Johnstone et al. at cross-sections 2

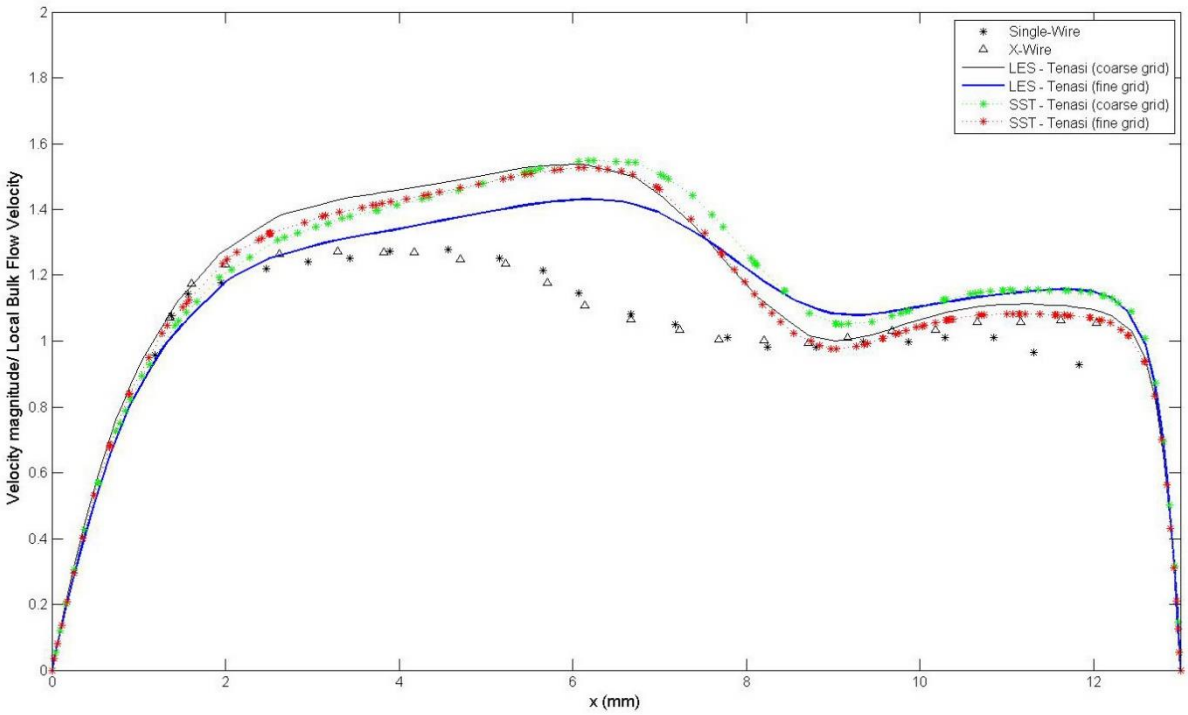

Figure 4.1.24 Comparison of SST and LES solutions of coarse and fine mesh from *Tenasi* with experimental results from Johnstone et al. at cross-sections 3

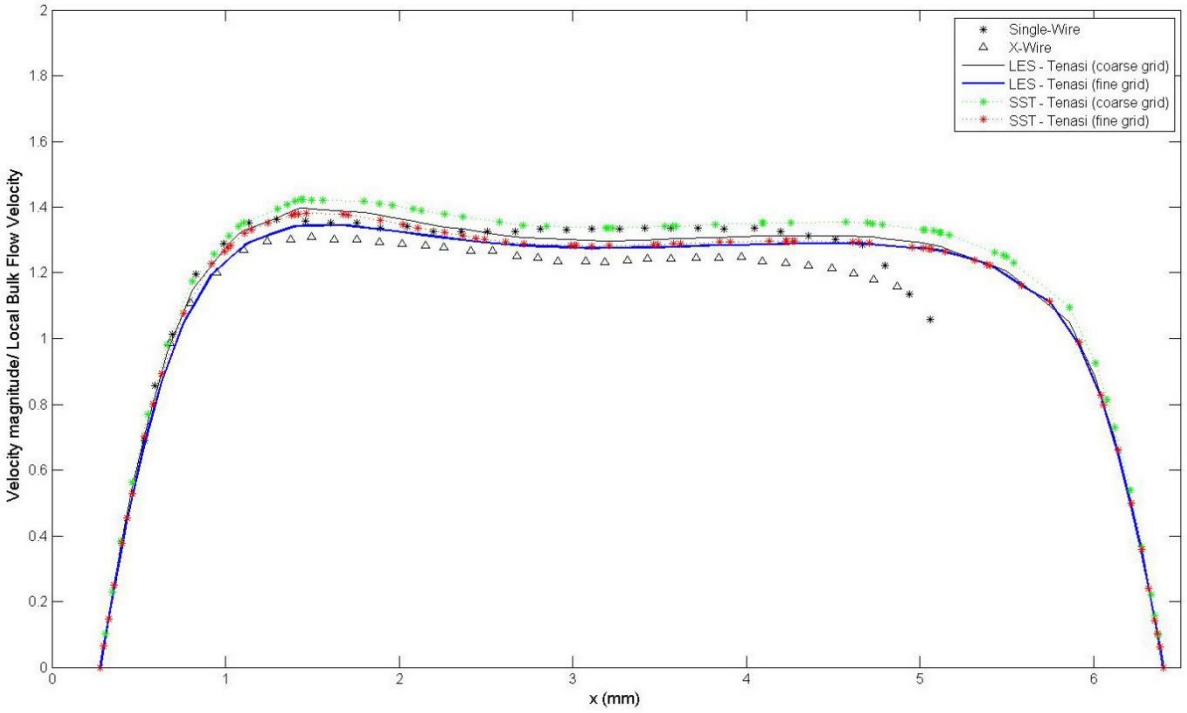

Figure 4.1.25 Comparison of SST and LES solutions of coarse and fine mesh from *Tenasi* with experimental results from Johnstone et al. at cross-sections 4

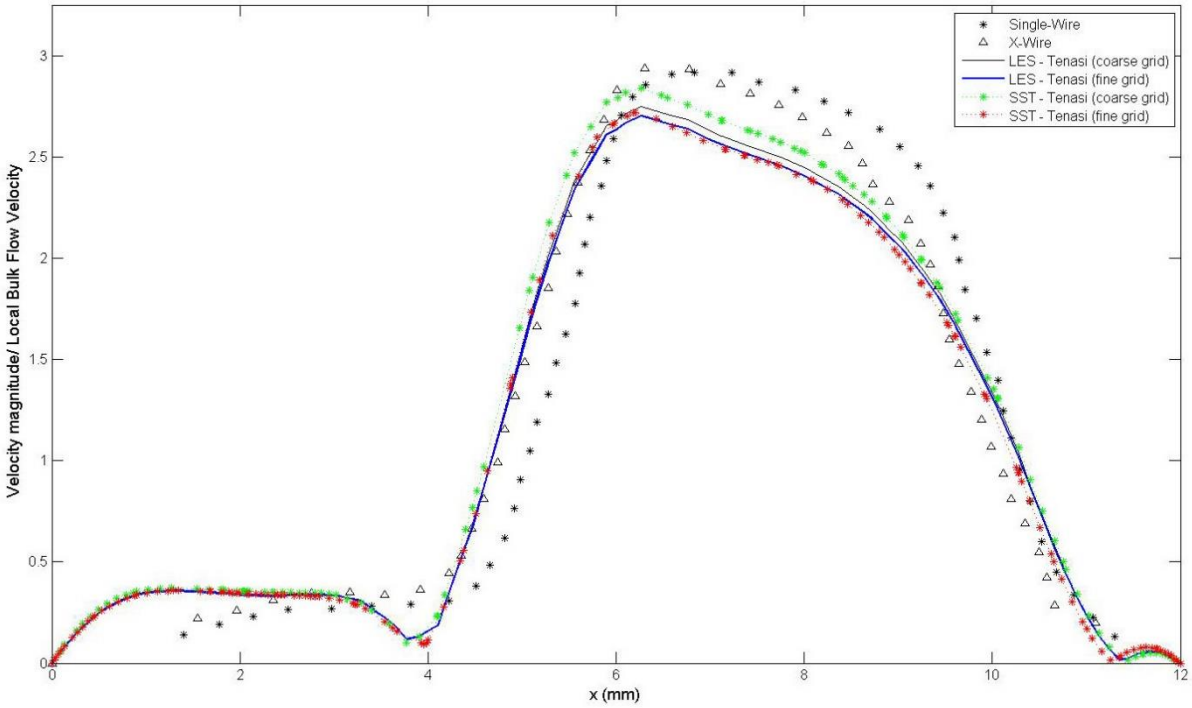

Figure 4.1.26 Comparison of SST and LES solutions of coarse and fine mesh from *Tenasi* with experimental results from Johnstone et al. at cross-sections 5

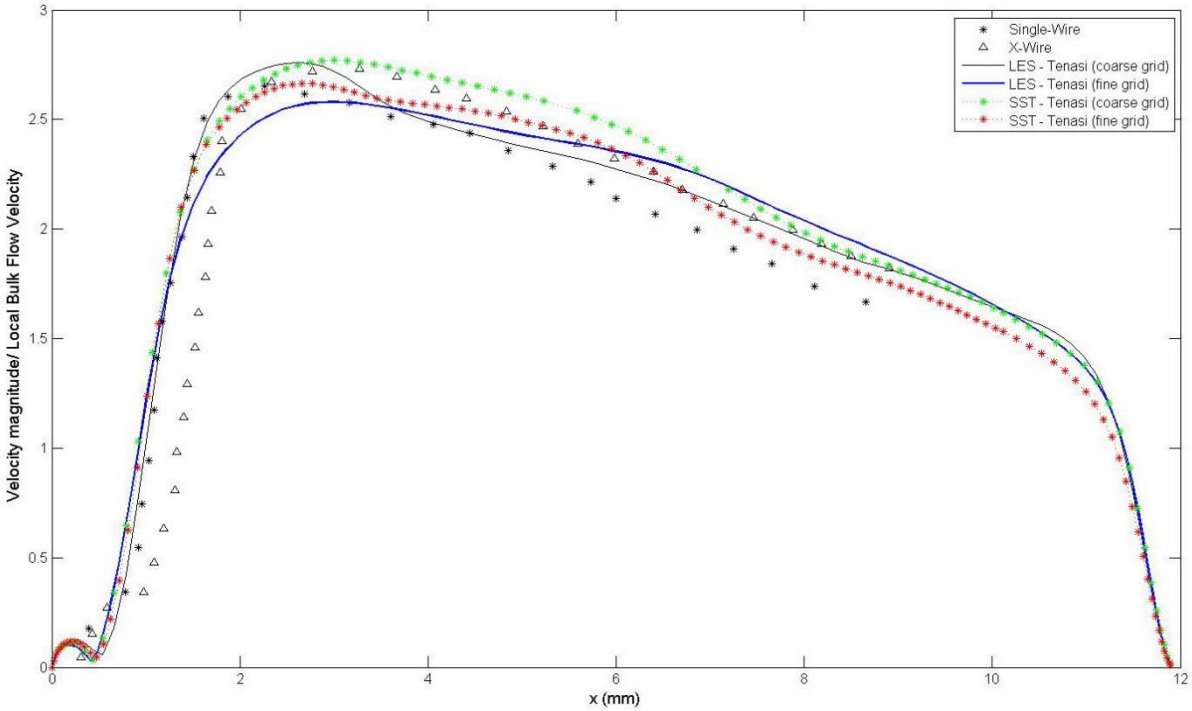

Figure 4.1.27 Comparison of SST and LES solutions of coarse and fine mesh from *Tenasi* with experimental results from Johnstone et al. at cross-sections 6

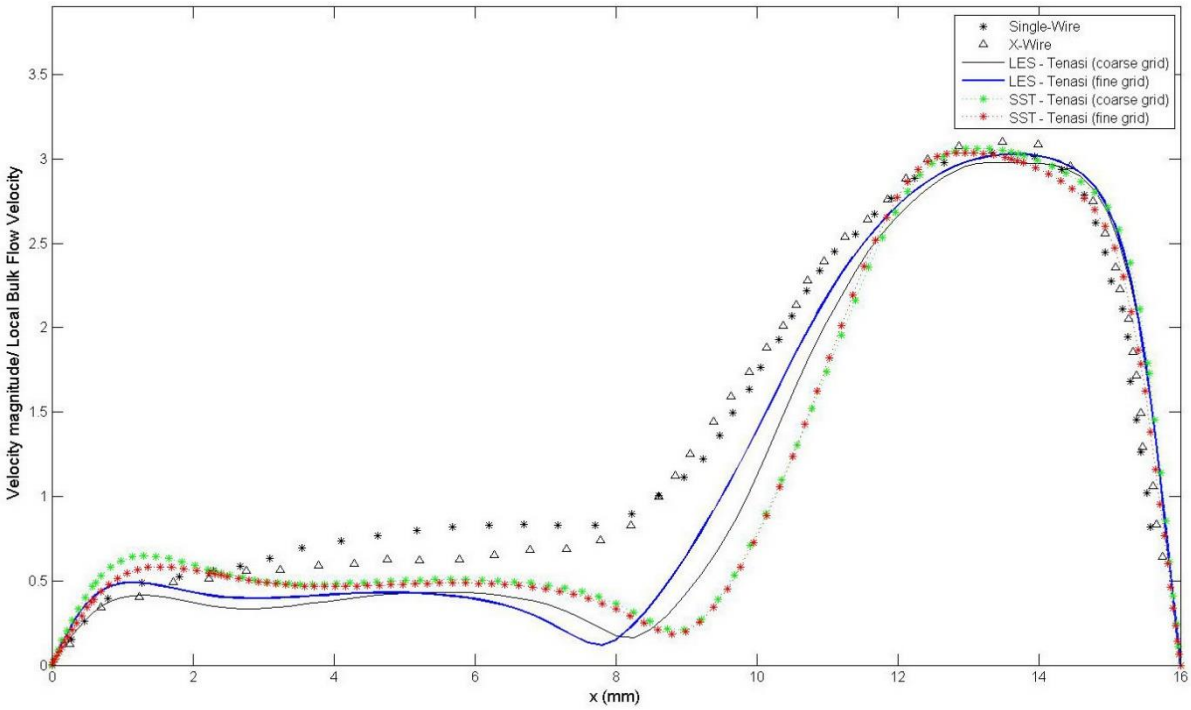

Figure 4.1.28 Comparison of SST and LES solutions of coarse and fine mesh from *Tenasi* with experimental results from Johnstone et al. at cross-sections 7

4.1.2. Transient Breathing Cycle and Constant Inspiration/Expiration

Simulations of the ETA geometry were performed for two flow rates summarized in Table 3.4.1. Two simulations corresponding to constant inspiration/expiration and one for four full breathing cycles were carried out. This resulted in a total of three simulations per flow rate. The constant inspiration/expiration cases were conducted at two Reynolds numbers, i.e., 875 and 1750, analogous to peak flow conditions in the full breathing cases, i.e., the Womersley numbers of 4.72 and 6.68, respectively.

4.1.2.1. Inspiration

Peak inspiration in a breathing cycle solutions occurs at a phase angle (ϕ) of $\pi/2$ at t = 2s and t = 1s for $\alpha = 4.72$ and $\alpha = 6.68$, respectively. The comparison was made between peak

inspiration with corresponding constant inspiration for both flow rates (i.e., Re = 875 and Re = 1750). Volumetric fluxes were computed at the inlet and outlet of the ETA. The deviation of flow rates from the targeted values was found no more than 0.05%.

The flow structure of a transient breathing cycle in both flow rates is depicted against the time-averaged solution in the central sagittal plane of the ETA in Figure 4.1.29. Even though the flow features in the oral cavity as well as the oro-pharynx are observed to be laminar, unsteadiness can be seen in the transient breathing cases for both flow rates, especially for the higher flow rate where unsteadiness was much more pronounced. This figure shows that the flow rate is not the main cause of the turbulent flow through the trachea. Because of the Dean-like instabilities caused by the curvature of the oro-pharynx, as discussed in section 4.1.1, and the complicated structure of the pharynx and the larynx, the airflow became transitional and eventually fully turbulent through the trachea. Fully turbulent flows in both flow rates are clearly visible in the figures.

From the time-averaged solutions the same flow pattern was observed in both flow rates. The only difference is in the strength of the airflow as the velocity values doubled for the higher flow rate. This is clearly visible in the laryngeal jet and the size of the recirculation bubble in the trachea.

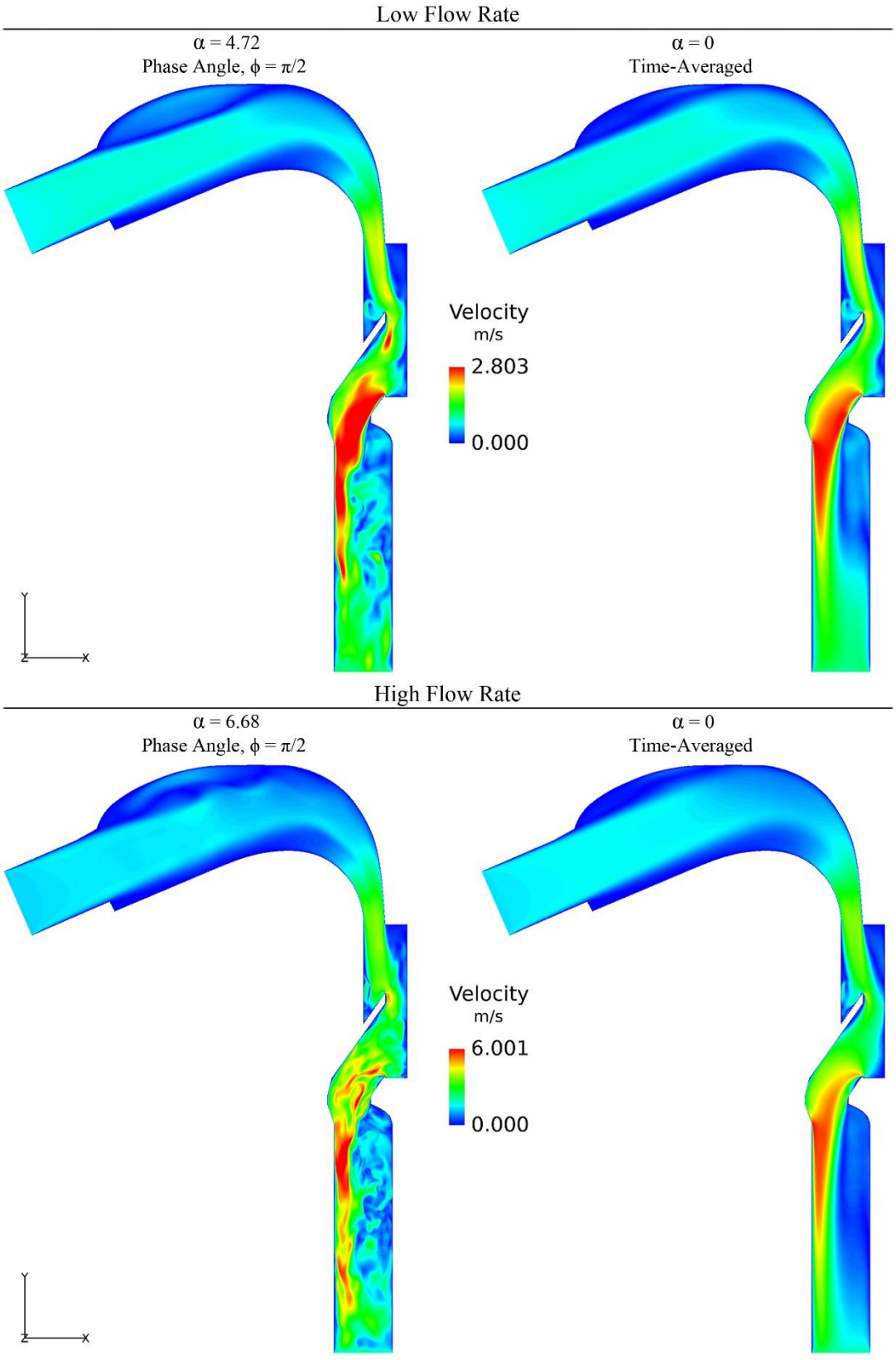

Figure 4.1.29 Central sagittal cross-section of the ETA, illustrating velocity magnitude during inspiration. Peak transient breathing and time-averaged solutions of both flow rates

The secondary flow at three cross-sections of the ETA (see Figure 4.1.2) is illustrated in Figure 4.1.30, to have a better insight into the flow regime during inspiration. Cross-sections 5, 6 and 7 were selected because significant changes in the flow features occur through the pharynx, the larynx and more importantly the trachea. The comparison of these three critical cross-sections between transient breathing and constant inspiration are discussed in the following.

Cross-section 5 is located in the pharynx (see Figure 4.1.2) upstream of the larynx. Clear differences can be observed in the cross-flow pattern between transient breathing and the time-averaged solution of both flow rates. Unsteadiness in the high flow rate case was much more pronounced compared to the low flow rate. This shows the effects of the flow rate in this region. Transient solution of the high flow rate illustrated strong unsteadiness of the flow pattern in the oro-pharynx, before entering the pharynx. As was previously mentioned, this is due to the Dean-type instabilities in oro-pharynx.

The complicated flow regime in the pharynx causes the flow to be turbulent in the larynx and consequently in the trachea. The presence of the turbulent flow is clearly visible in iso-surface of Q-criterion in Figure 4.1.31. Unsteadiness in both transient breathing solutions can be observed at cross-section 6. In this location, the turbulent feature is clearly visible in the transient breathing solution of the high flow rate, whereas the low flow rate shows less turbulent features.

The cross-section in the trachea, cross-section 7, illustrates the fully turbulent flow for both the low and high flow rates. This highly turbulent flow phenomenon is much more prominent for the higher flow rates. Figure 4.1.31 illustrates this flow phenomenon through the larynx and the trachea.

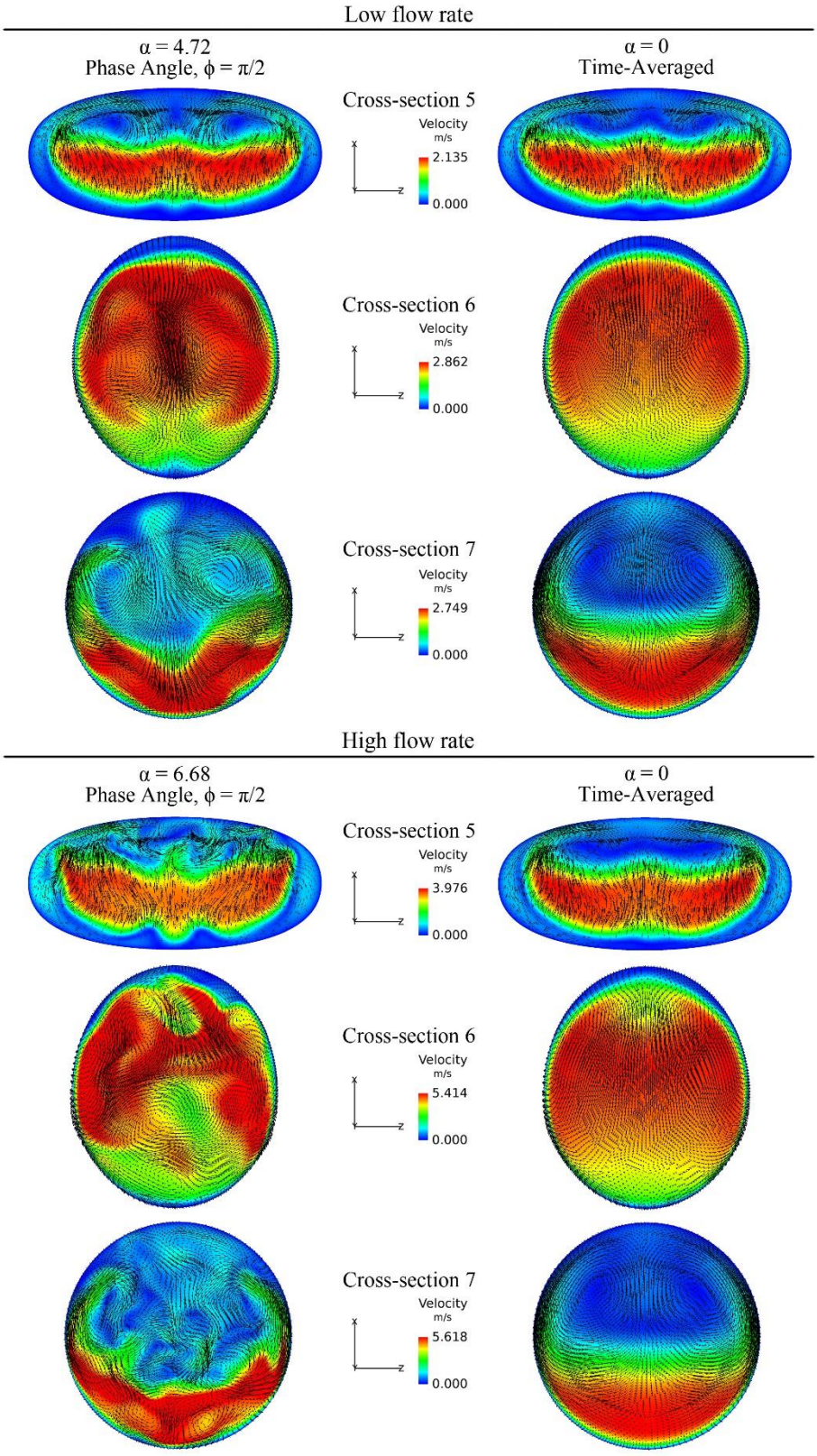

Figure 4.1.30 Secondary flows of the low and the high flow rate during inspiration in the ETA. Cross-sections 5, 6 and 7 of the low and high flow rates from the top and bottom, respectively

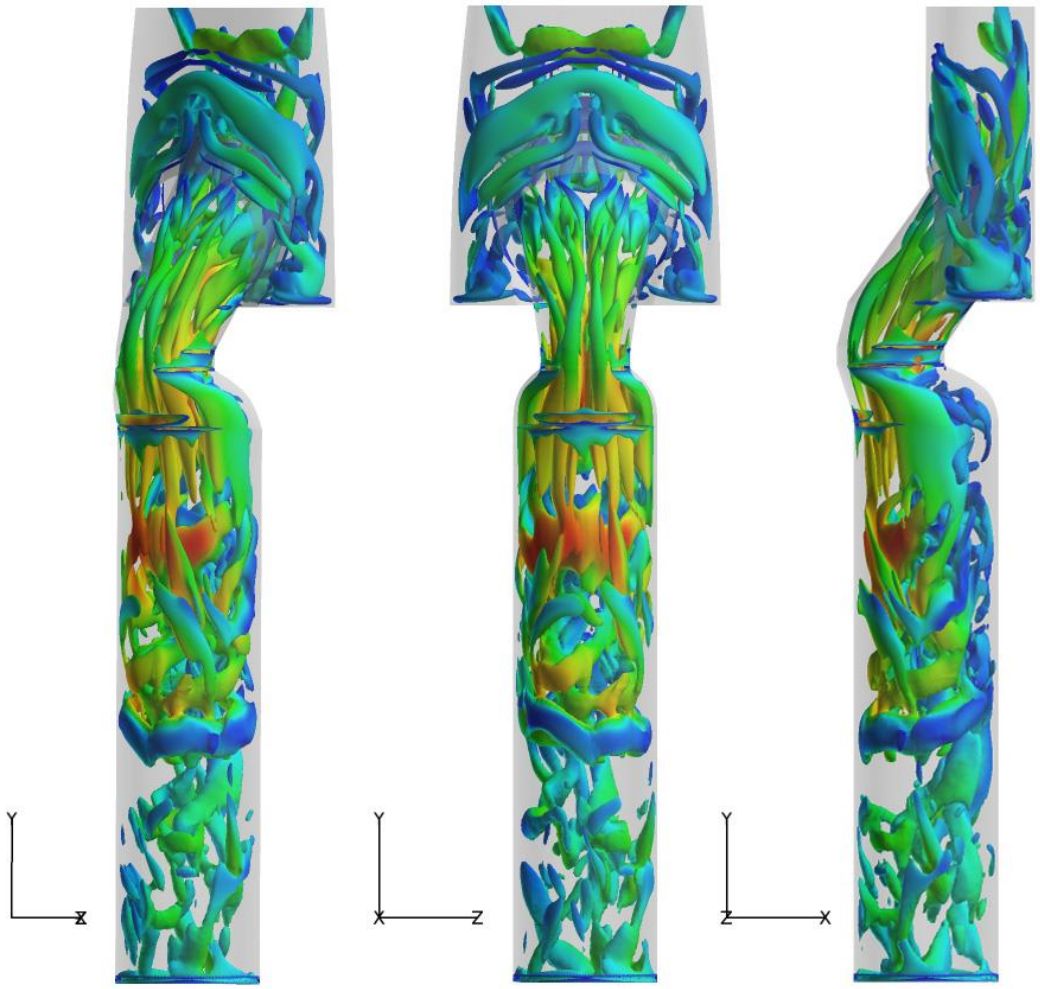

Figure 4.1.31 Iso-surface of Q-criterion colored by velocity magnitude for $\alpha = 4.72$. Oblique (45°) view, coronal view and sagittal view of the pharynx and larynx from left to right. The geometry is in gray

The values of the Reynolds number at all seven cross-sections of interest in Figure 4.1.2 are summarized in Table 4.1.2. The largest differences between Reynolds numbers for the constant inspiration and peak transient breathing for the low Womersley number was found to be no more than 4% and appeared at cross-section 7. As the flow rate is doubled i.e., higher Womersley number, the differences of the Reynolds numbers are almost doubled as well. Similarly, cross-section 7 has the highest discrepancy in Reynolds number with approximately 8.8% for higher Womersley number.

Cross-section 6 has the highest value of Reynolds number in both flow rates among all the cross-sections considered here. This illustrates the effects of complexity of the geometry on the flow field in this region.

Table 4.1.2 Reynolds numbers of constant and transient breathing cycle during inspiration at all seven traverse cross-sections of the ETA

Sections	Low flow rate		High flow rate	
	Re (Constant inspiration)	Re (Transient breathing)	Re (Constant inspiration)	Re (Transient breathing)
1	713.597	728.061	1382.267	1335.218
2	733.432	736.446	1430.346	1355.901
3	964.419	956.027	1875.775	1761.193
4	1438.58	1423.414	2812.341	2711.333
5	1121.371	1127.912	2192.301	2291.231
6	1617.872	1665.383	3164.647	3122.832
7	1284.596	1338.778	2396.159	2628.476

4.1.2.2. Expiration

Peak expiration in breathing cycle solutions occurs at a phase angle $\phi = 3\pi/2$ at $t = 6s$ and $t = 3s$ for $\alpha = 4.72$ and $\alpha = 6.68$, respectively. The comparison was made between peak expiration with corresponding constant expiration for both flow rates (i.e. Re = 875 and Re = 1750).

Velocity contour plot of the central sagittal plane of the ETA during expiration for both flow rates are displayed in Figure 4.1.32. Similar to inspiration, the flow pattern of the time-averaged solution of both flow rates is approximately identical; the only difference is in the strength of the flow. The third backward facing step during inspiration has a role of a forward facing step during expiration. As with inspiration, the jet-like flow was formed in the opposite direction during

expiration. A small recirculation zone appeared at posterior wall of trachea. Unsteadiness in jet-flow was observed in transient breathing of both flow rates. These effects are more significant for higher flow rate. Critical changes in the flow regime occurred right after jet-flow in the larynx. For both flow rates, the flow is unsteady and highly three-dimensional.

Cross-sections 2, 3, 4 and 5 were considered for investigation of the flow structure during expiration. These locations were selected to have a better understanding of the flow phenomena in the pharynx and the oral cavity. As can be seen in the central sagittal plane of both flow rates in Figure 4.1.32, fully turbulent flow is clearly visible in the pharynx, oro-pharynx and consequently in the oral cavity. Secondary flows at the four cross-sectional planes of interest in the ETA are shown in Figure 4.1.33. The flow pattern of the time-averaged solutions of the low and the high flow rates are approximately similar at each cross-section. Again, the difference is in the strength of the flow. The flow pattern of transient breathing solutions at all these four cross-sections shows the presence of the turbulent flow in both flow rates. This can also be seen in the iso-surface of the Q-criterion of the low flow rate in Figure 4.1.34. This reveals that the flow regime during expiration is much more complicated than inspiration with high level of turbulent flow in the pharynx and the oral cavity.

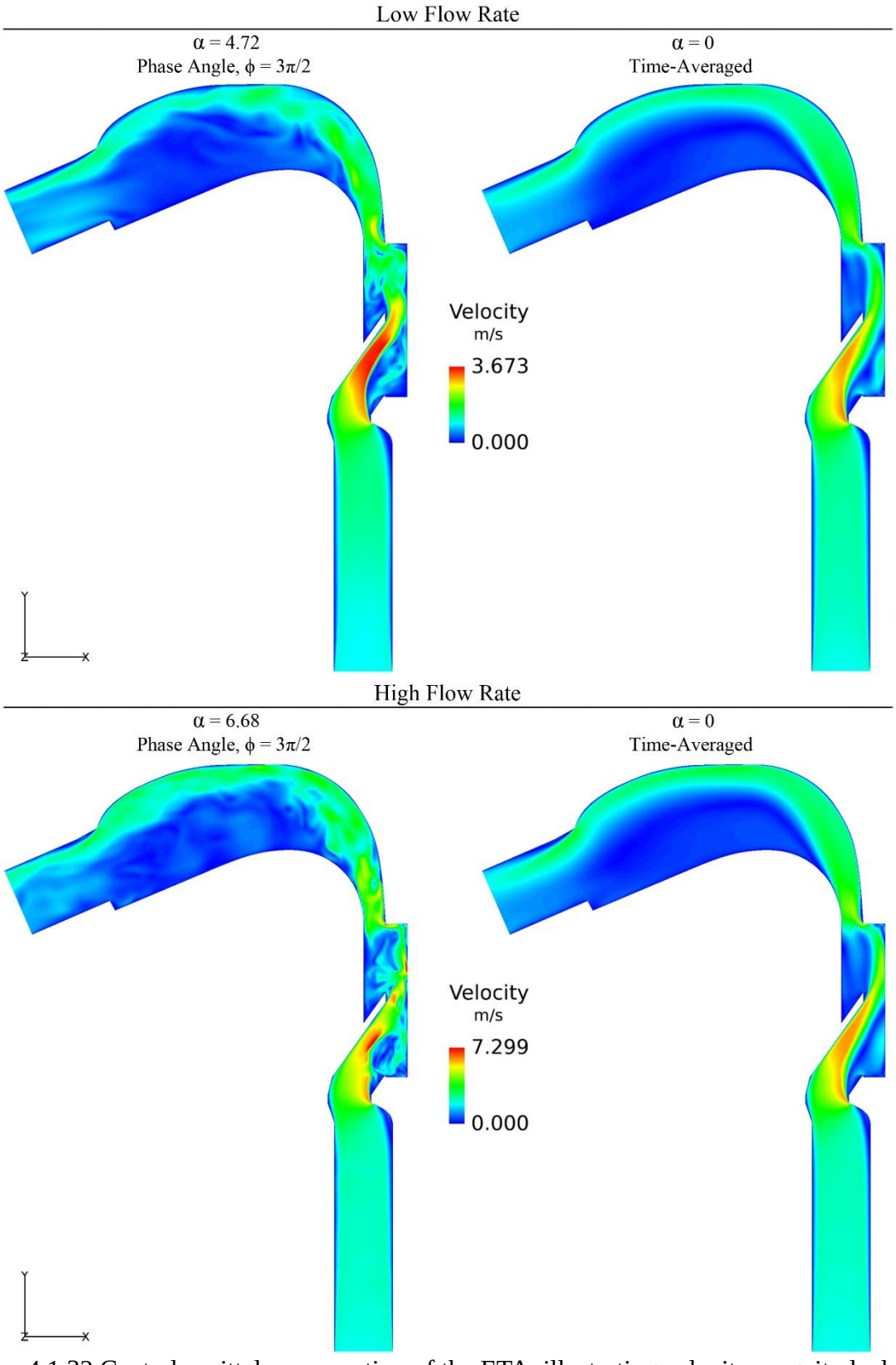

Figure 4.1.32 Central sagittal cross-section of the ETA, illustrating velocity magnitude during expiration. Peak transient breathing and time-averaged solutions of both flow rates

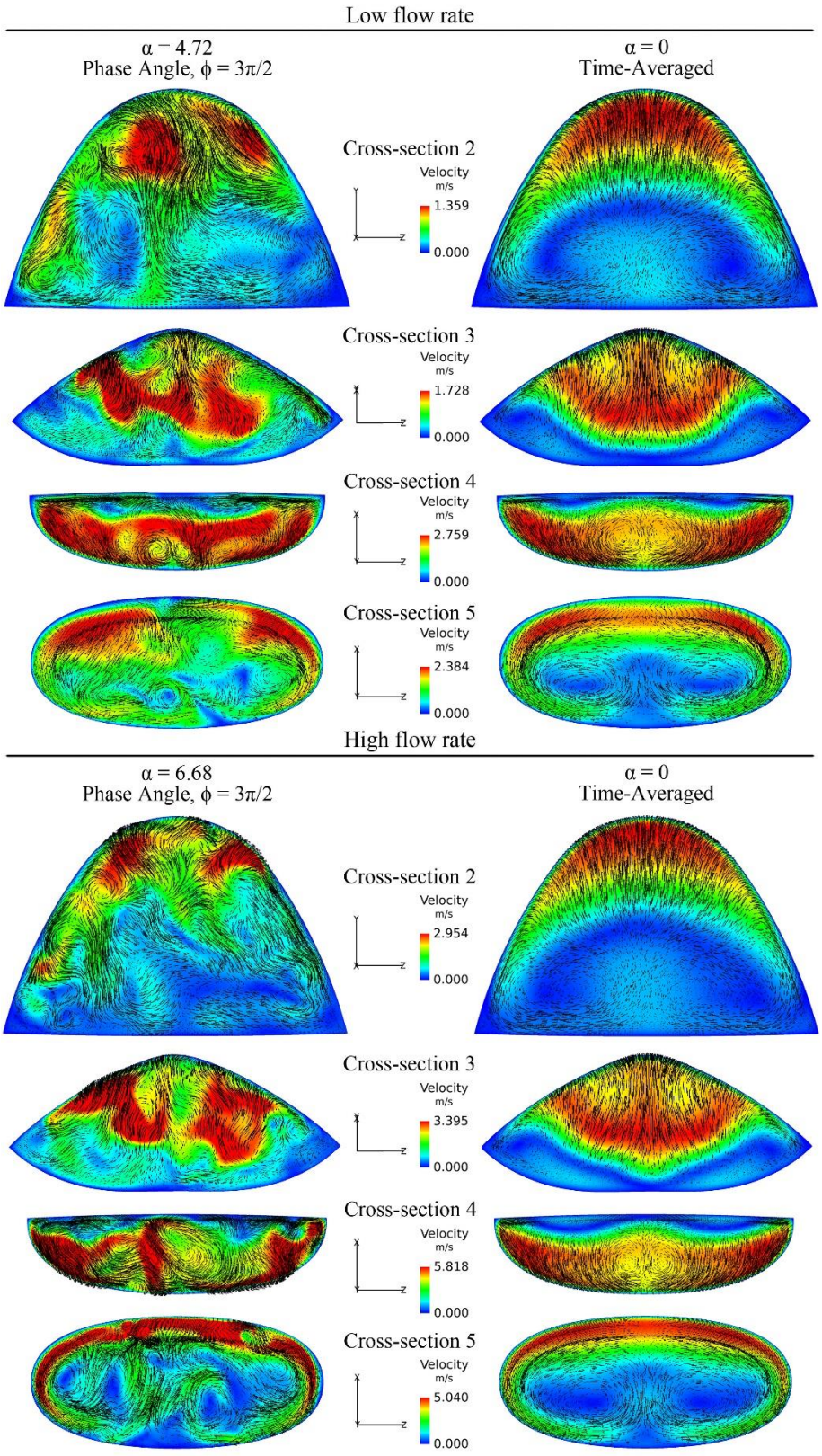

Figure 4.1.33 Secondary flows of the low and the high flow rate during expiration in the ETA. Cross-sections 5, 6 and 7 of the low and high flow rates from the top and bottom, respectively

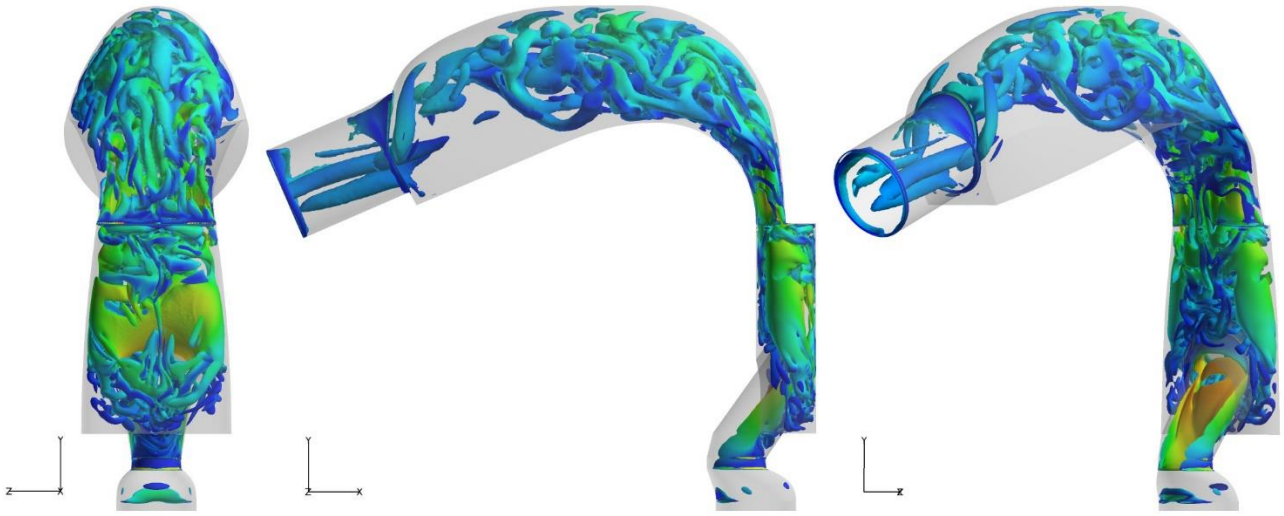

Figure 4.1.34 Iso-surface of Q-criterion colored by velocity magnitude for $\alpha = 4.72$ during expiration. Back view, sagittal view and right oblique (45°) of the ETA and the trachea from left to right. The geometry is in gray

The values of the Reynolds number for both flow rates during expiration are summarized at all seven cross-sections in Table 4.1.3. Reynolds numbers in either flow rates suggested higher values at all locations, except cross-section 7, compared to inspiration in Table 4.1.2. This confirms the earlier statement about the complexity of the flow during expiration. In both flow rates, significant differences of Reynolds number between transient breathing and constant expiration can be observed in many cross-sections, especially at locations 2 and 5. Highly turbulent flow was found through the pharynx, oro-pharynx and the oral cavity. Hence, discrepancies of the Reynolds numbers are not surprising at these locations.

Table 4.1.3 Reynolds numbers of constant and transient breathing cycle during expiration at all seven traverse cross-sections of the ETA

Sections	Low flow rate		High flow rate	
	Re (Constant expiration)	Re (Transient breathing)	Re (Constant expiration)	Re (Transient breathing)
1	945.102	1043.254	2219.366	2022.078
2	895.443	1089.182	1738.081	1956.892
3	1100.579	1196.479	2331.001	2441.723
4	1482.123	1589.581	2957.619	3204.702
5	1276.371	1594.169	2402.271	2726.444
6	1641.512	1604.205	3233.819	3115.181
7	1077.172	1156.734	2113.241	2076.269

4.2. The Lower Airway Geometry

Simulations of the lower airway geometry were carried out for two flow rates similar to the ETA described in 4.1.2.1. Similarly, six simulations per flow rate were conducted.

Five cross-sections of interest in the lower airways which are orthogonal to the axial flow, shown in Figure 4.2.1, were selected for analysis. To visualize secondary flows, velocity vectors were projected onto these two-dimensional cross-sections. These cross-sections are representative of the airflow entering each lobar bronchus. Again, volumetric fluxes were computed at each of the cross-sections. The deviations of flow rates from the targeted values were found no more than 0.045% in the lower airways.

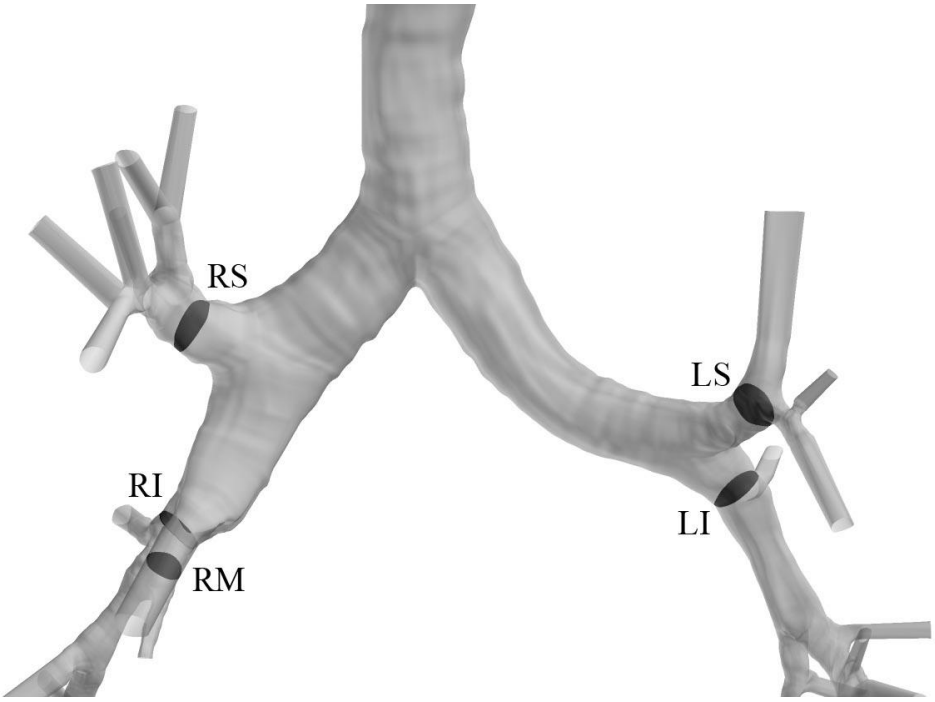

Figure 4.2.1 Five cross-sections examined for each case at each of the lobar bronchus

4.2.1. Inspiration

The comparison was made between peak inspiration (i.e. $\alpha = 4.72$ and $\alpha = 6.68$) with analogous constant inspiration for both flow rates (i.e. Re = 875 and Re = 1750). According to previous study [24], the flow structures at each cross-section for peak inspiration are expected to be approximately similar to constant inspiration.

The flow regime through the lower airway during inspiration can be seen in the coronal view of the lower airway in Figure 4.2.2. The same flow feature was observed for the high flow rate. Hence, it was excluded from this figure and only the $\alpha = 4.72$ solution is depicted here.

In the extension at the inlet, boundary layers started to grow and a fully-developed flow entered the lower airway. Thus, a parabolic velocity profile entered the trachea. The stagnation point can clearly be seen in Figure 4.2.2 where the geometry and the flow bifurcate. The pressure

has the highest value at the stagnation point in the first bifurcation. Therefore, low-speed flow was expected in this zone, as it is visible with circle-shape in Figure 4.2.2 (b). Another observation is a low-speed region at the entrance of the right superior lobar bronchus which can be seen in iso-surface of velocity magnitude in Figure 4.2.2 (a).

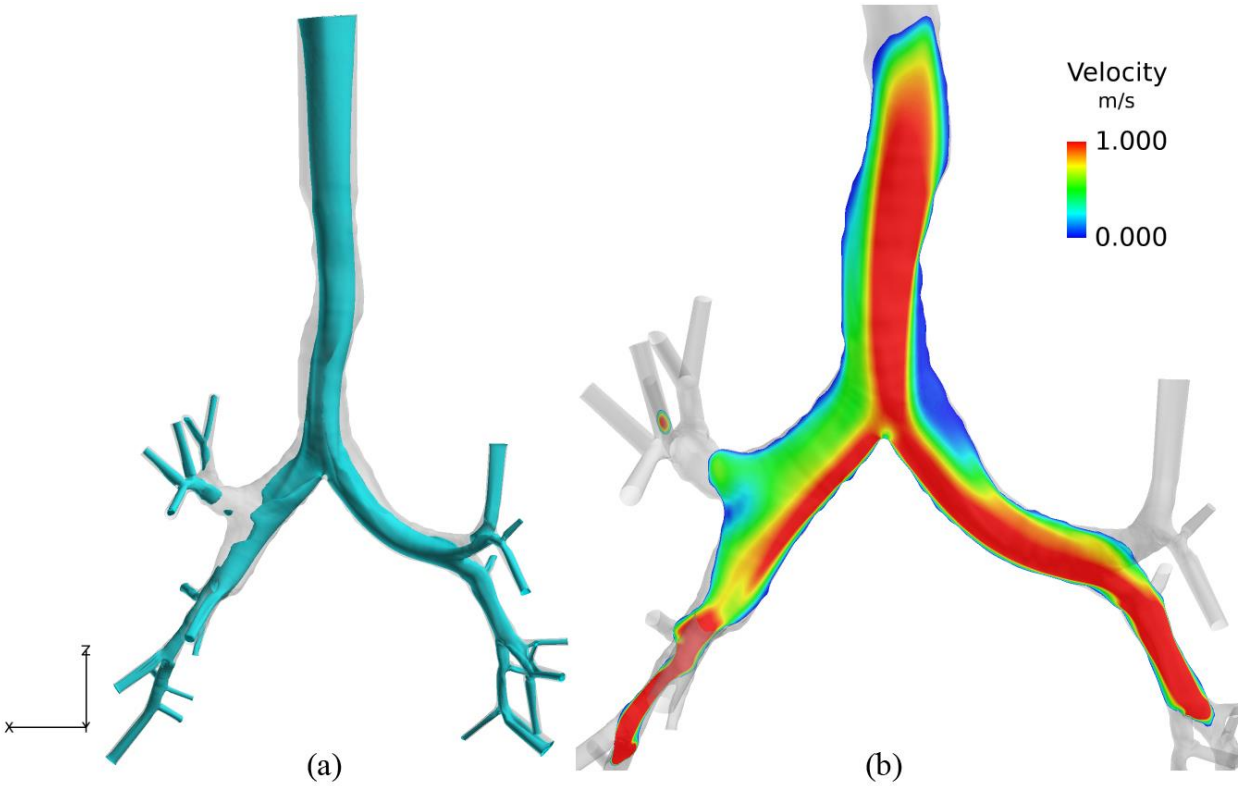

Figure 4.2.2 Coronal view of the lower airway for $\alpha = 4.72$ during inspiration. a) Iso-surface of velocity magnitude speed at 0.75 m/s. b) Cross-sectional plane of velocity magnitude is limited to 1.0 m/s

The secondary flow for the inspiration case at all cross-sections of lobar bronchus is depicted in Figure 4.2.3. At the RS lobar bronchus, no significant difference were observed between peak inspiration and time-averaged solutions for the low flow rate, while noticeable differences were

observed at the higher flow rate. As it can be seen from the figure for low flow rate, there are two counter rotating vortices in the time-averaged solution, while three vortices appeared in $\alpha = 6.68$. This shows the impact of increasing the flow rate and its critical influences on the flow pattern at this cross-section. However, in time-averaged solutions no significant differences can be observed between the low and the high flow rates, these differences were more pronounced in transient breathing solution of both Womersley numbers.

Similarly for the RM, no prominent changes can be seen for the low flow rate. In contrast, the differences between transient solution ($\alpha = 6.68$) and its corresponding time-averaged solution were more pronounced. Although, three vortices are visible in both solutions of the high flow rate, moderate differences can be recognized between transient and constant solutions. Similar to the RS, the impact of the higher flow rate on the flow pattern was significant at this cross-section. The cross-flow velocity pattern in the RI lobar bronchus is approximately equal for both flow rates and no significant differences can be seen between breathing cycle and time-averaged solutions. Similarly, no noticeable changes in the cross-flow pattern of the LS lobar bronchus can be seen between transient peak inspiration and analogous time-averaged solutions for both flow rates. A comparison between the low and high flow rate solutions reveals that the velocity magnitude (the colors in Figure 4.2.3) on the right corner of this cross-section suggested smaller values in high flow rate compared to the low flow rate.

Secondary flows of both flow rates in the LI lobar bronchus shows significant changes in the flow pattern. There are two fully developed vortices in the low flow rate, whereas the number of vortices present in the high flow rate seems to go up by one. Note that only subtle differences are visible in the cross-flow velocity vector patterns between the transient breathing and time-averaged solutions for both flow rates.

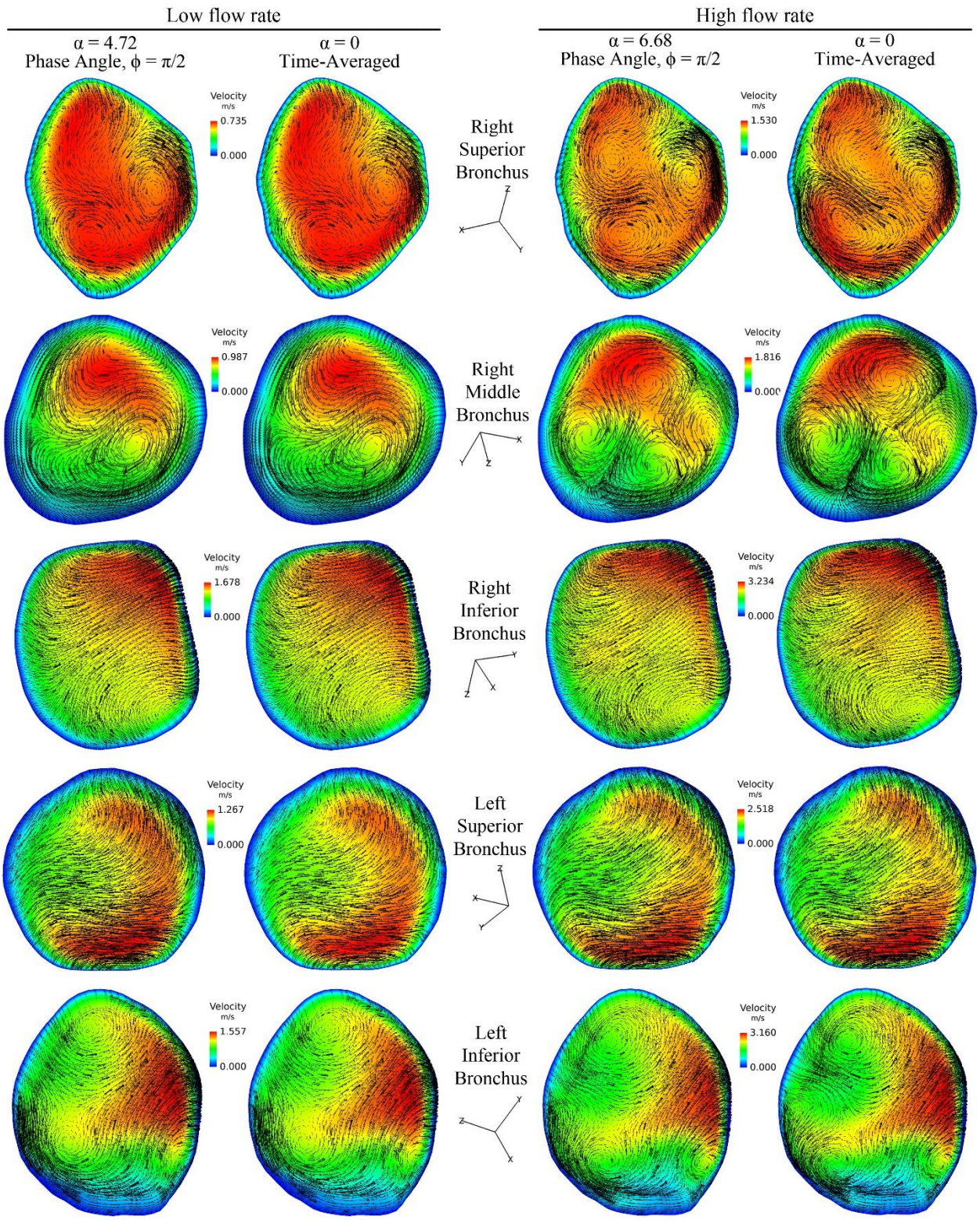

Figure 4.2.3 Secondary flows of the low and the high flow rate during inspiration in the lower airway geometry. RS, RM, RI, LS and LI lobar bronchus are shown from top to bottom

4.2.2. Expiration

Similar simulations, as described in section 4.1.2.2, were performed for two flow rates through the lower airway geometry. The comparison was made between peak transient breathing (i.e. $\alpha = 4.72$ and $\alpha = 6.68$) with corresponding constant expiration for both flow rates (i.e. Re = 875 and Re = 1750).

During expiration, the flow features for all cross-sections were remarkably similar except for the LS lobar bronchus at the high flow rate. The secondary flows at all cross-sections of lobar bronchus are depicted in Figure 4.2.4.

Cross-flow patterns were relatively unaffected by the flow rate for the RS lobar bronchus. Comparison of both flow rates indicates that the flow regime became slightly more complicated as the flow rate increased. In the RM cross-section, this complexity is not noticeable and the same cross-flow pattern can be observed in transient and time-averaged solutions of both flow rates. In the RI and the LI lobar similar to the RS, complex flow feature with significant changes can be seen for both flow rates. Approximately equal cross-flow pattern was observed between transient breathing and time-averaged solutions in each flow rate of these two lobar bronchus. Nevertheless, in the LS cross-section the low Womersley (i.e. $\alpha = 4.72$) and its corresponding time-averaged solution were approximately similar, differences in the high flow rate are clearly visible in cross-flow patterns as well as low velocity magnitude at the bottom corner of the cross-section in constant expiration.

From comparisons of transient breathing with analogues constant expiration in both flow rates, only the LS lobar bronchus for high flow rate showed significant differences in velocity magnitude, while the flow feathers at other cross-sections were remarkably similar.

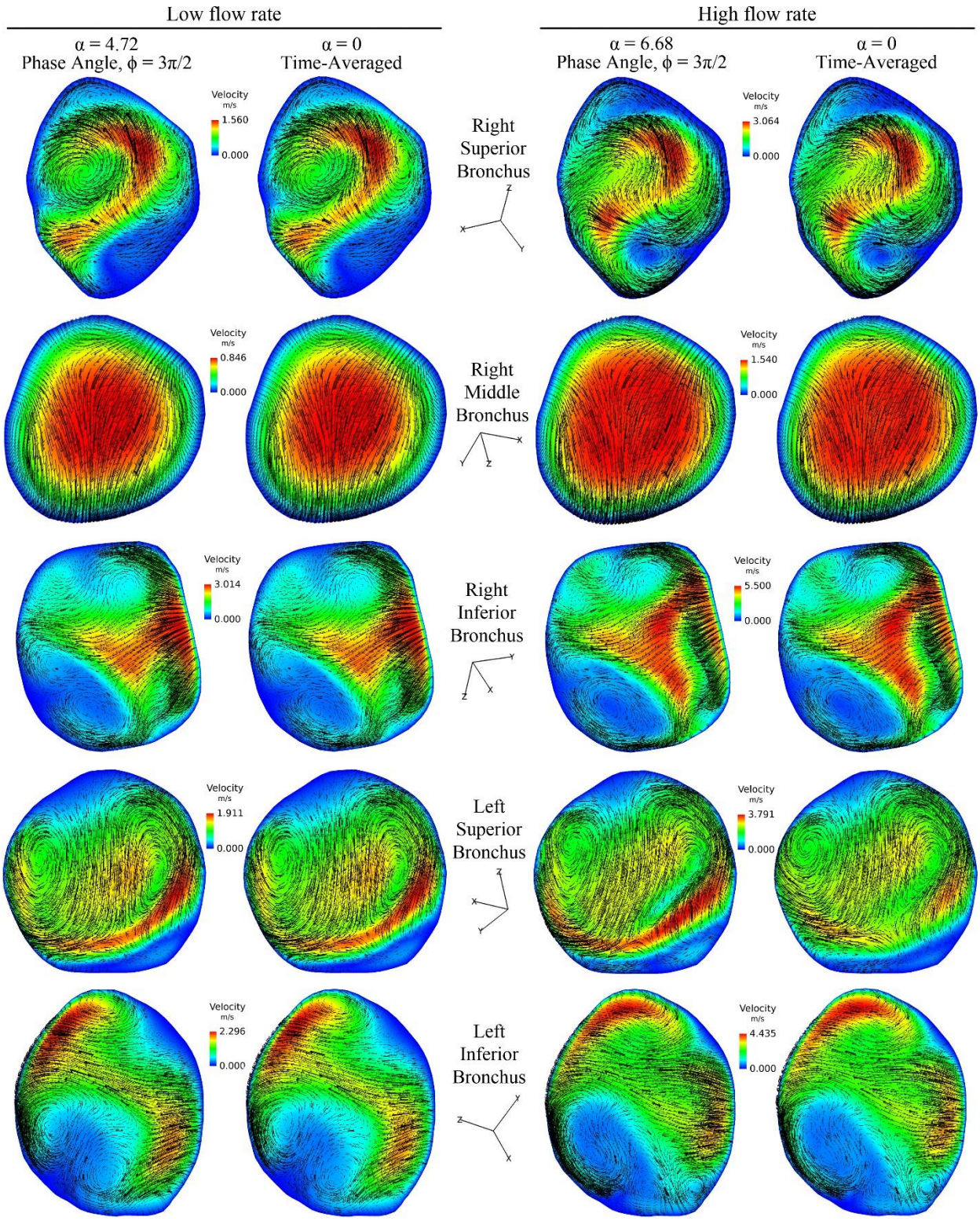

Figure 4.2.4 Secondary flows of the low and the high flow rate during expiration in the lower airway geometry. RS, RM, RI, LS and LI lobar bronchus are shown from top to bottom

In order to have a better understanding of flow regime during expiration, an iso-surface of velocity magnitude (iso-value = 1.0 m/s) for $\alpha = 4.72$ and cross-sectional sagittal view of the lower airway are provided in Figure 4.2.5. Two secondary flows through the daughter branches can be seen and consequently they formed a counter-rotating vortex through the trachea. The low-speed flow is visible in the dashed circle region in Figure 4.1.30 (a) where the flow from right and left primary bronchus joins together. Furthermore, the flow is quasi-steady during expiration for the lower Womersley number, whereas the effects of unsteadiness in the higher Womersley number are more pronounced. This will be discussed in section 4.4.2.

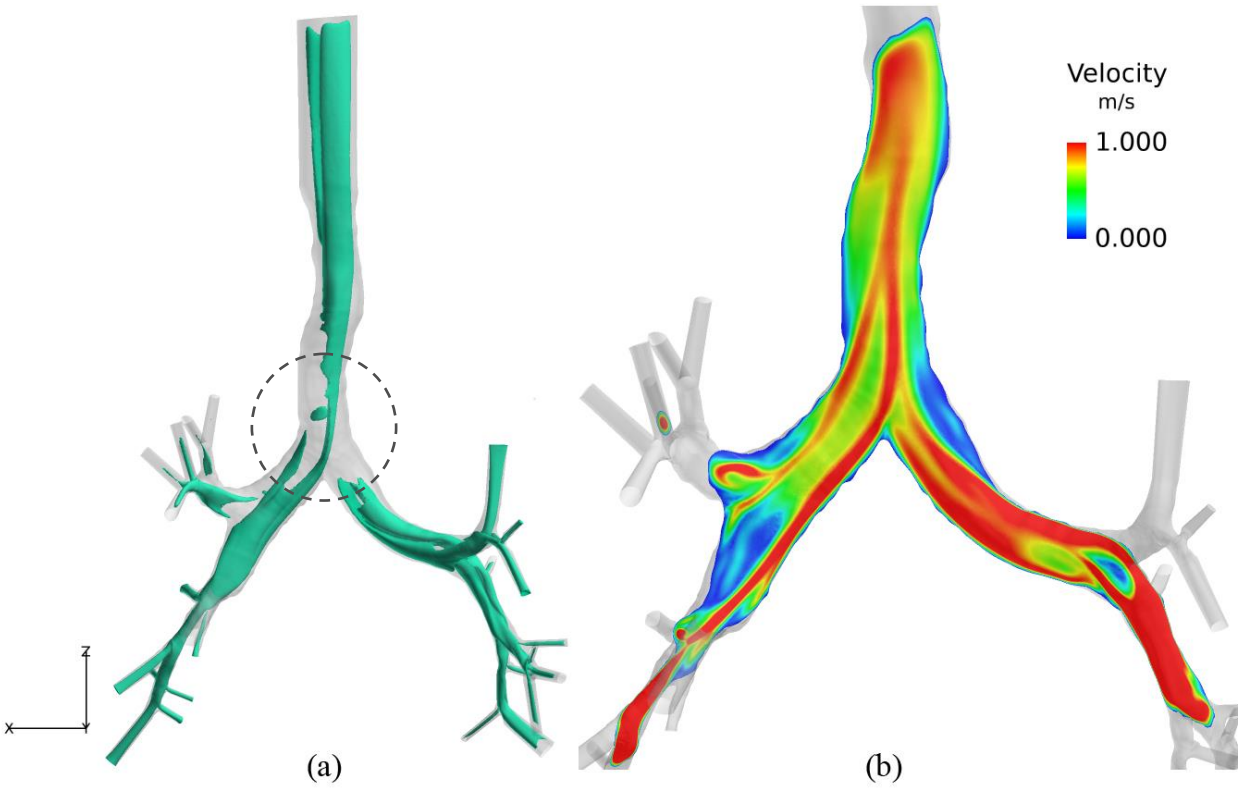

Figure 4.2.5 Coronal view of the lower airway for $\alpha = 4.72$ during expiration. a) Iso-surface of velocity magnitude speed at 1 m/s. b) Cross-sectional plane of velocity magnitude is limited to 1.0 m/s

4.3. The Entire Airway Geometry

The flow phenomena in the lower airway using uniform inlet boundary conditions were investigated in previous section. The presence of the ETA at the inlet of the trachea provided the realistic inlet conditions for the lower airway. As was described in section 3.1.3, the entire airway geometry is the combination of the ETA and the lower airway geometry. Simulations of one full breathing cycle and constant inspiration/expiration through the entire airway geometry were conducted for two flow rates of interest and the comparison of the solutions are discussed in this section.

4.3.1. Inspiration

The effect of the ETA on the airflow through the lower airways is visible in Figure 4.3.1. Sagittal sections of the oro-pharynx, the pharynx, the larynx and the trachea at peak inspiration for transient breathing cases and constant inspiration (time averaged as well as instantaneous) for both flow rates are displayed in this figure. As can be seen, highly turbulent flow occurs in the trachea. The level of the turbulence intensity can be gauged by comparing the flow fields between the instantaneous and time-averaged cases. This is characteristic of the turbulence generated by the effect of the epiglottis and structure of the larynx and is very similar to the results of other researchers [4], [6]. The laryngeal jet is clearly visible in the solutions shown in Figure 4.3.1, with its strength increasing with flow rate.

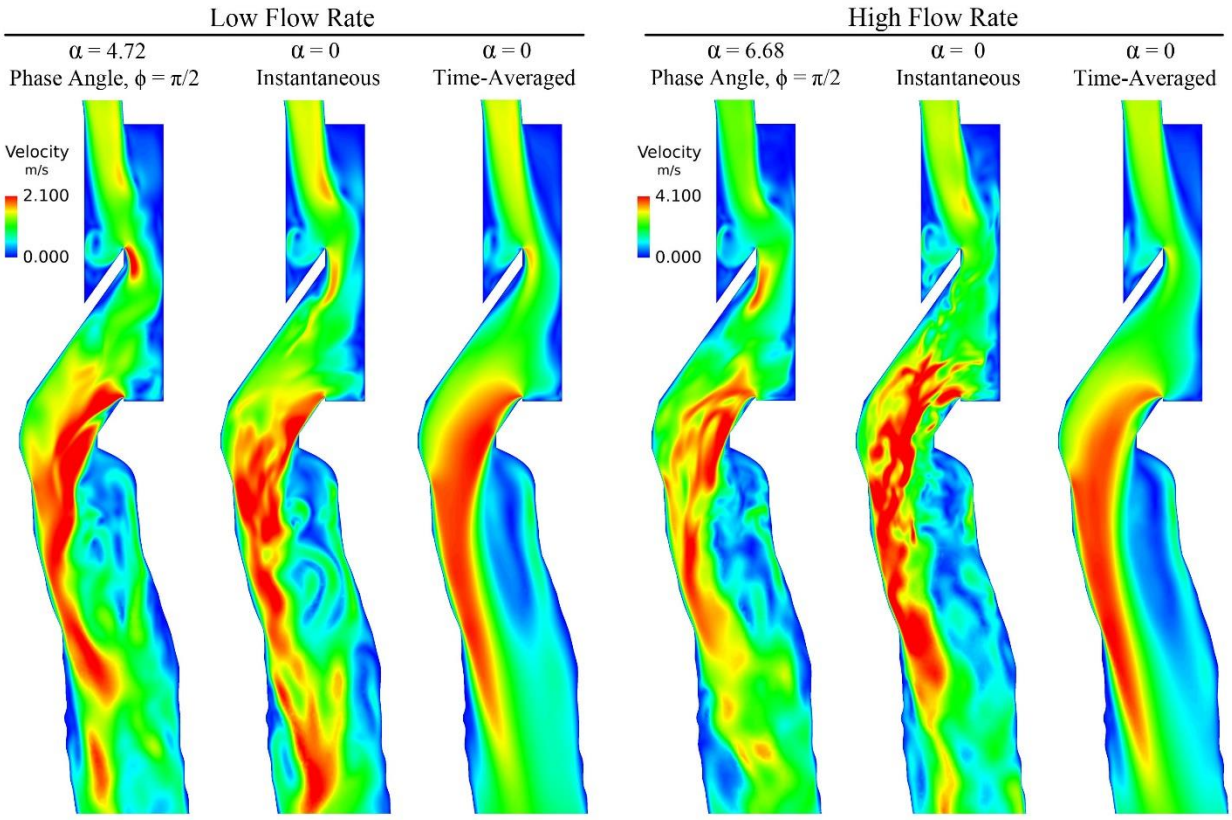

Figure 4.3.1 Sagittal cross-section of the ETA including trachea showing velocity magnitude during inspiration in the entire geometry

The strength of the flow field between the low and high flow rates can be seen by comparing the time-averaged solutions. The recirculation bubble in the posterior region of the high flow rate is bigger, compared to low flow rate. Hence, for high flow rate greater turbulence level and also more unsteadiness are expected downstream of the trachea. This flow regime with high turbulence intensity has a critical impact on the flow features in the downstream of the lower airway. Iso-surface of Q-criterion for $\alpha = 6.68$ is provided in Figure 4.3.2 to have a better insight into this flow phenomenon through the entire airway. In this figure, the presence of highly turbulent flow can be observed through the pharynx, the larynx and the trachea. There is no significant turbulence features in daughter branch or other generations. The feature of

turbulence can be seen in the zeroth generation, i.e. the trachea, caused by the complex flow formed by the ETA. These effects can be recognized by comparing the flow pattern at five cross-sections of interest (see Figure 4.2.1). Secondary flows at all cross-sections of the lobar bronchus are depicted in Figure 4.3.3.

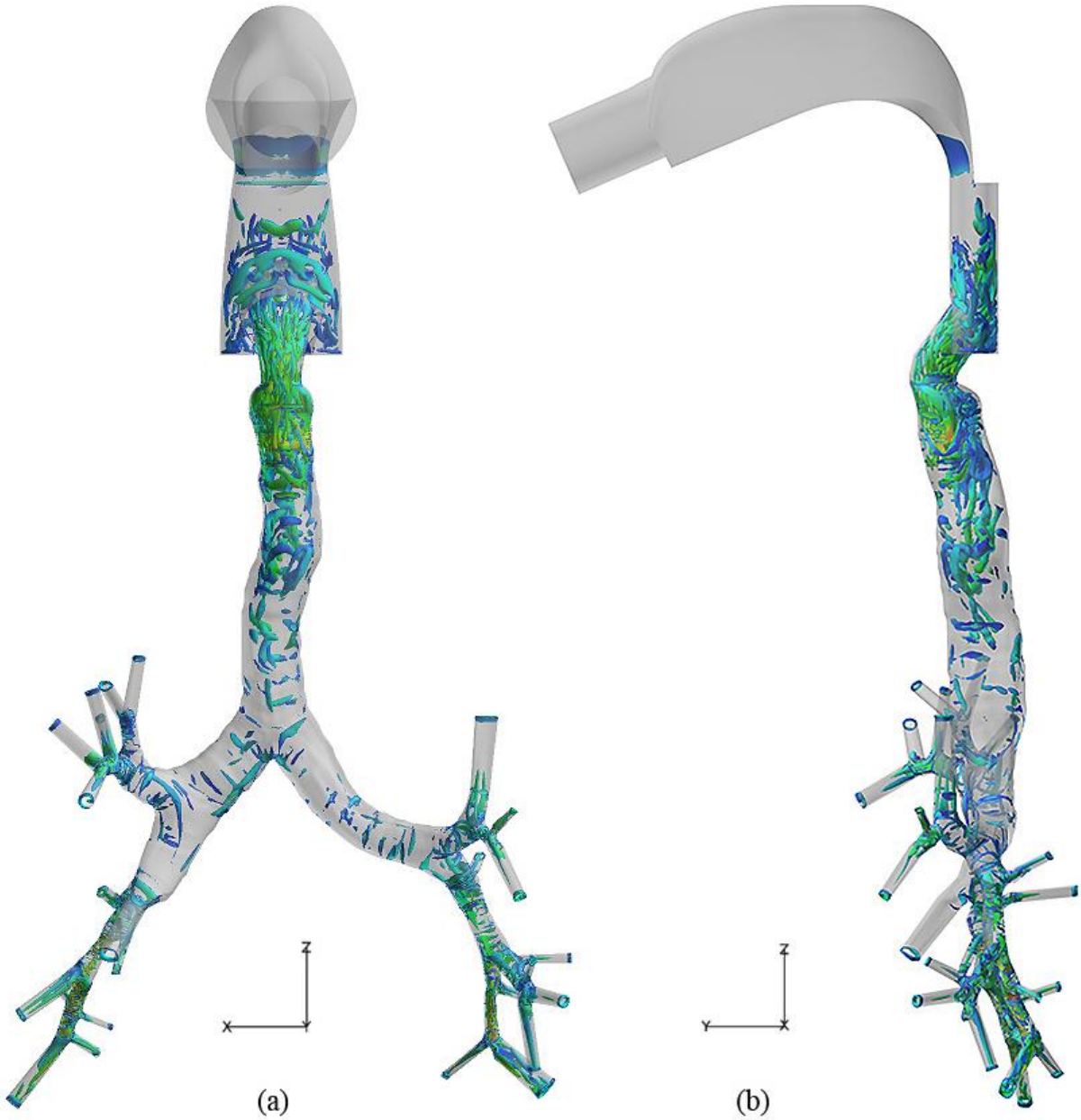

Figure 4.3.2 Iso-surface of Q-criterion colored by velocity magnitude for $\alpha = 6.68$ during inspiration. a) Front view b) sagittal view of the entire airway geometry. The geometry is in grey

In the RS lobar bronchus cross-section, the flow pattern of the transient solution is slightly different from time-averaged solution for the low flow rate ($\alpha = 4.72$). The difference is in the velocity magnitude with the transient breathing solution being approximately 4% higher than the time-averaged solution. In contrast, discernible differences can be seen in flow patterns of the transient breathing and time-averaged solutions for high flow rate ($\alpha = 6.68$). The high Womersley number solution exhibits the presence of two distinct vortices, whereas the cross-flow pattern of corresponding time-averaged solution is similar to that of the low flow rate case.

The differences of the cross-flow patterns for the RM lobar bronchus cross-sections are more pronounced for both flow rates. Two fully-developed vortices appeared in transient breathing and time-averaged solutions of both flow rates, but different flow structure between them can be seen. This suggests the existence of unsteadiness in this cross-section.

For high flow rate, differences between transient breathing and time-averaged solutions are visible for the RI cross-section, while smaller changes can be seen for the low flow rate solutions at this location.

Different cross-flow patterns between transient and time-averaged solutions can be observed for both flow rates of the LS; however, differences are not as noticeable as the RS and RM locations. Conversely, prominent differences are visible at the LI cross-section. In low flow rate, one vortex appears at the bottom left-hand corner of the time-averaged solution that cannot be seen in $\alpha = 4.72$. The flow patterns of the time-averaged solution for both flow rates are approximately the same; however, small deviations are visible between solutions. The numbers of vortices appearing in the high flow rate go up by one in the transient breathing solution, compared to the corresponding time-averaged solution. This additional vortex appeared at the top of the cross-section.

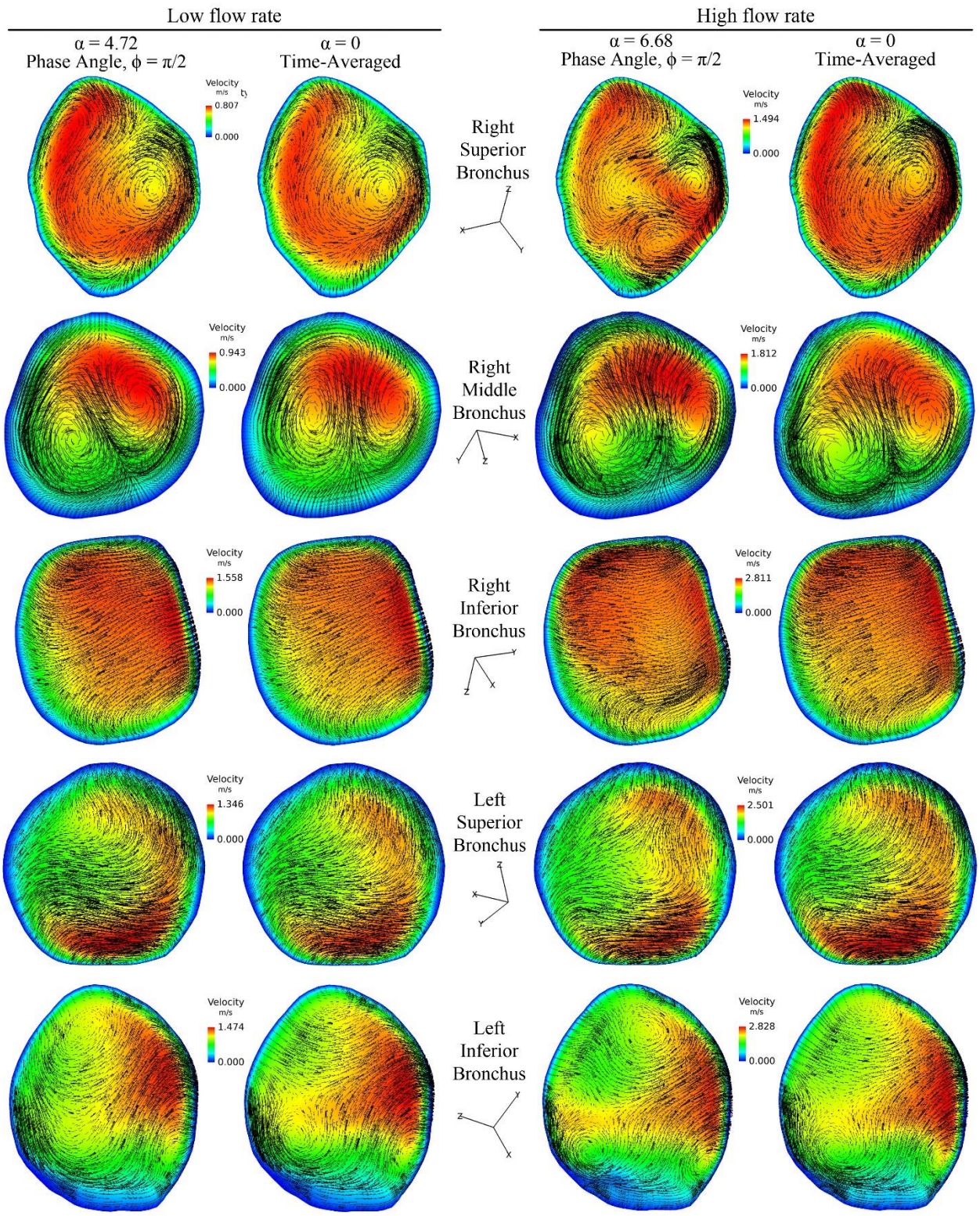

Figure 4.3.3 Secondary flows of the low and the high flow rate during inspiration in the entire airway geometry. RS, RM, RI, LS and LI lobar bronchus are shown from top to bottom

4.3.2. Expiration

The secondary flows during expiration are displayed in Figure 4.3.4 at all lobar bronchus. Similar to the solutions of the lower airway only, the flow structure of transient breathing and corresponding time-averaged solutions at all locations were approximately equal for the low flow rate. Similar cross-flow patterns between transient breathing and constant expiration can be observed at all cross-sections in the high flow rate, except the LS and LI locations. The differences in these two cross-sections are more pronounced in the velocity magnitude rather than the flow patterns. In the LS, the velocity magnitude of the transient breathing is 18% higher than the time-averaged solution. This difference is most visible at the bottom of this cross-section. Similarly for the LI, the velocity magnitude of the transient breathing solution is nearly 10% greater than the time-averaged solution. This is clearly visible at the top left-hand side of the cross-section. Note that the discrepancy of the cross-flow pattern in this location is more prominent than the LS lobar bronchus.

As was observed in Figure 4.3.2, the airflow through the pharynx to the trachea was highly turbulent and unsteady during inspiration. Observation in opposite direction indicates fully turbulent flow field through the ETA. As can be seen from Figure 4.3.5, the bulk of the turbulent structures are within the ETA, and their presence in the thorax is very limited. This is not surprising given that it is the glottis that causes the laryngeal jet to form during inspiration and the same causes turbulence to be generated during expiration. The changes in the velocity flow field observed in Figure 4.3.4 and the turbulence generated in the ETA during expiration could influence particle deposition patterns as one goes through a breathing cycle.

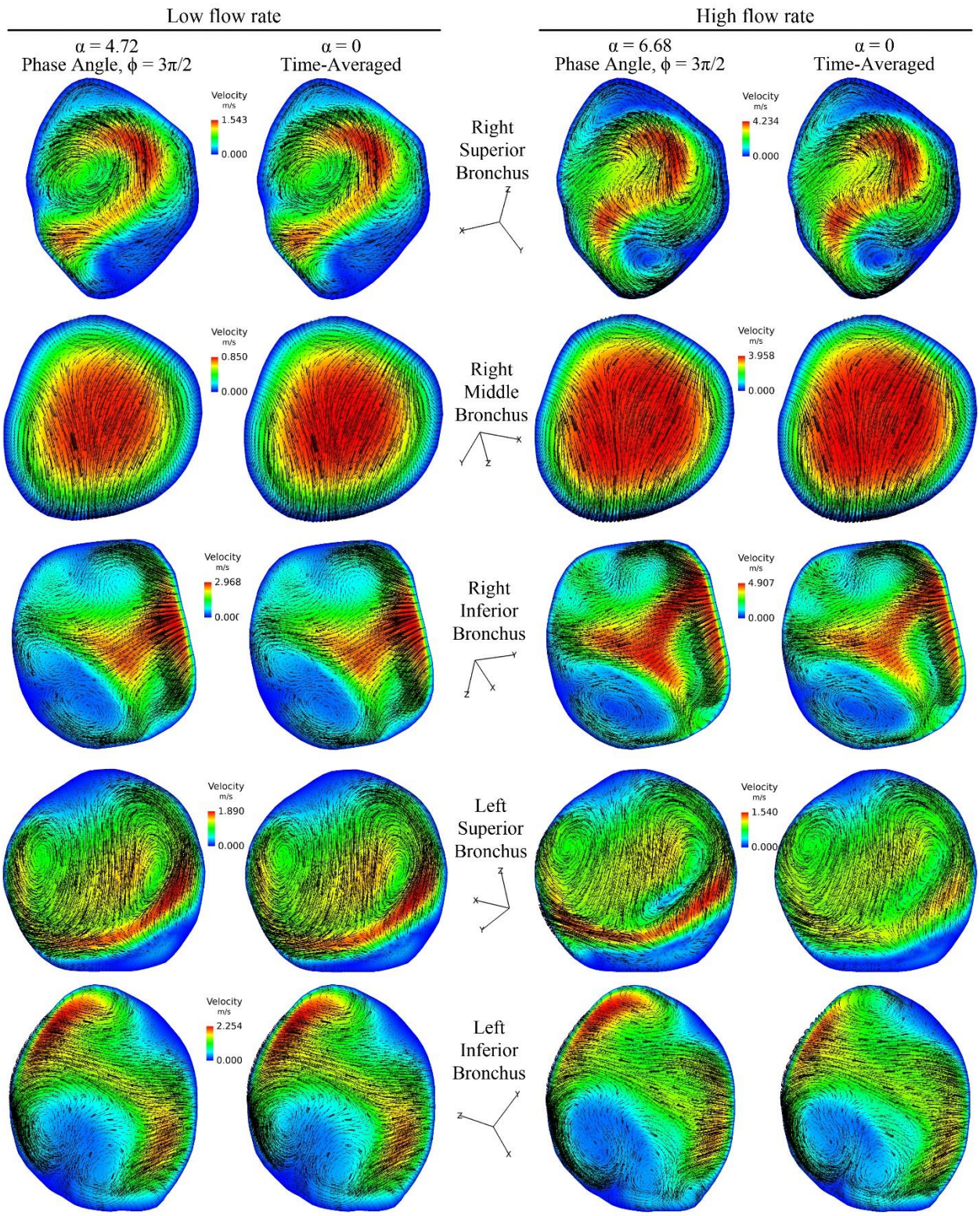

Figure 4.3.4 Secondary flows of the low and the high flow rate during expiration in the entire airway geometry. RS, RM, RI, LS and LI lobar bronchus are shown from top to bottom

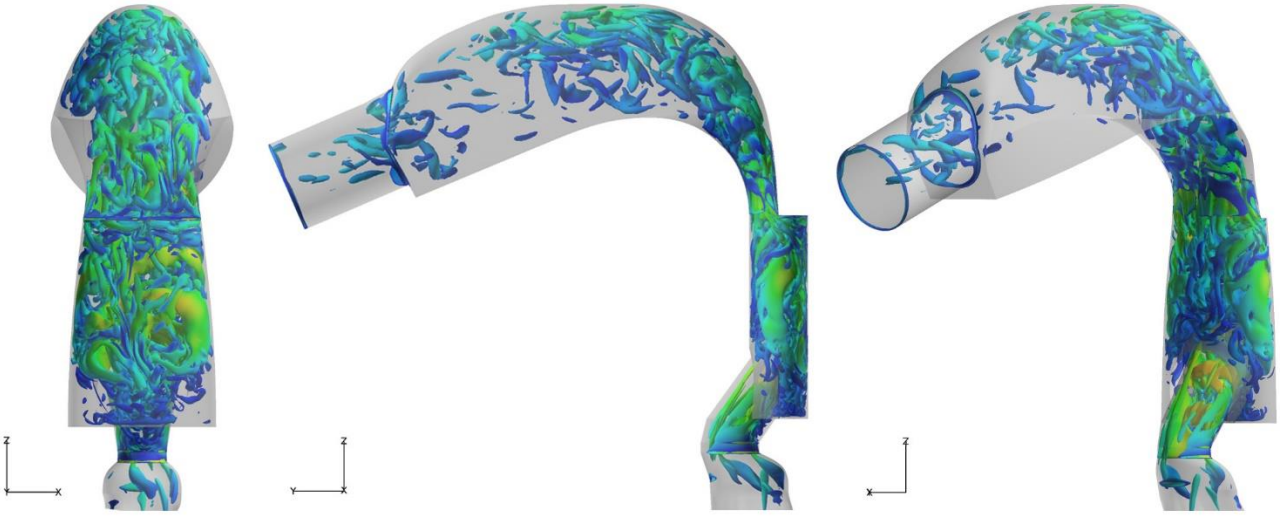

Figure 4.3.5 Iso-surface of Q-criterion colored by velocity magnitude for $\alpha = 6.68$ during expiration. Behind view, sagittal view and right oblique (45°) of the ETA from left to right. The geometry is in gray

4.4. Comparison of the Entire Airway with the ETA and the Lower Airway only

The solutions of the transient breathing cycle and constant inspiration/expiration of all three geometries were presented and discussed in previous sections. The effects of the ETA on the flow through the lower airways during inspiration can be gauged by comparing the solutions obtained from the entire airway geometry with one obtained for the lower airways only. Furthermore, the comparison can also be carried out during expiration to investigate the effects of flow regime where the ETA is downstream of the lower airway. The comparisons were carried out only for the high flow rate; because the qualitative nature of the comparison is similar between the high and low flow rate cases. To obtain a better understanding of the flow regime, comparisons were made between the entire airway geometry against the ETA and the lower airway geometry.

4.4.1. Inspiration

From investigation of the airflow during inspiration in the lower airway in section 4.2.1, the flow was found to be laminar in both flow rates, while in the ETA geometry, section 4.1.2.1, turbulent flow was induced due to the laryngeal jet formed by the construction of the larynx.

To investigate features of turbulence, TKE and turbulence intensity of central sagittal cross-section from the entire airway solution were compared against the ETA geometry in Figure 4.4.1. In the TKE contours of Figure 4.4.1, the strength of the highly turbulent flow can be seen in the ETA (geometry on the right), while the turbulent flow in the entire airway appeared at the posterior walls of the larynx. These differences in TKE contour plot of the entire airway could be because of the presence of the lower airway that impact on the level of the turbulence through the trachea. Nearly the same turbulence intensity can be seen between both geometries. Due to the presence of the small velocity magnitudes, there are several zones with high turbulence intensity. such as, recirculation bubble in the upper and the lower teeth in the oral cavity, the second backward facing step at the entrance of the pharynx, forward facing step between the anterior wall of pharynx and the epiglottis, at the bottom of the pharynx or upstream of the larynx and the third backward facing step in the trachea.

The effects of the ETA on the pulmonary airway can be gauged by comparing the entire airway with the lower airway only in Figure 4.4.2. This figure illustrates cross-sectional coronal view of velocity magnitude, limited to 2 m/s, for $\alpha = 6.68$ for the lower airway and the entire geometry. Noticeable differences can be observed between the solutions. A quasi-steady laminar flow occurs in the lower airway, while the entire airway geometry does not show similar flow phenomenon through the trachea and both primary bronchi. Figure 4.4.3 provides a better inside into of turbulence features through both airway geometries.

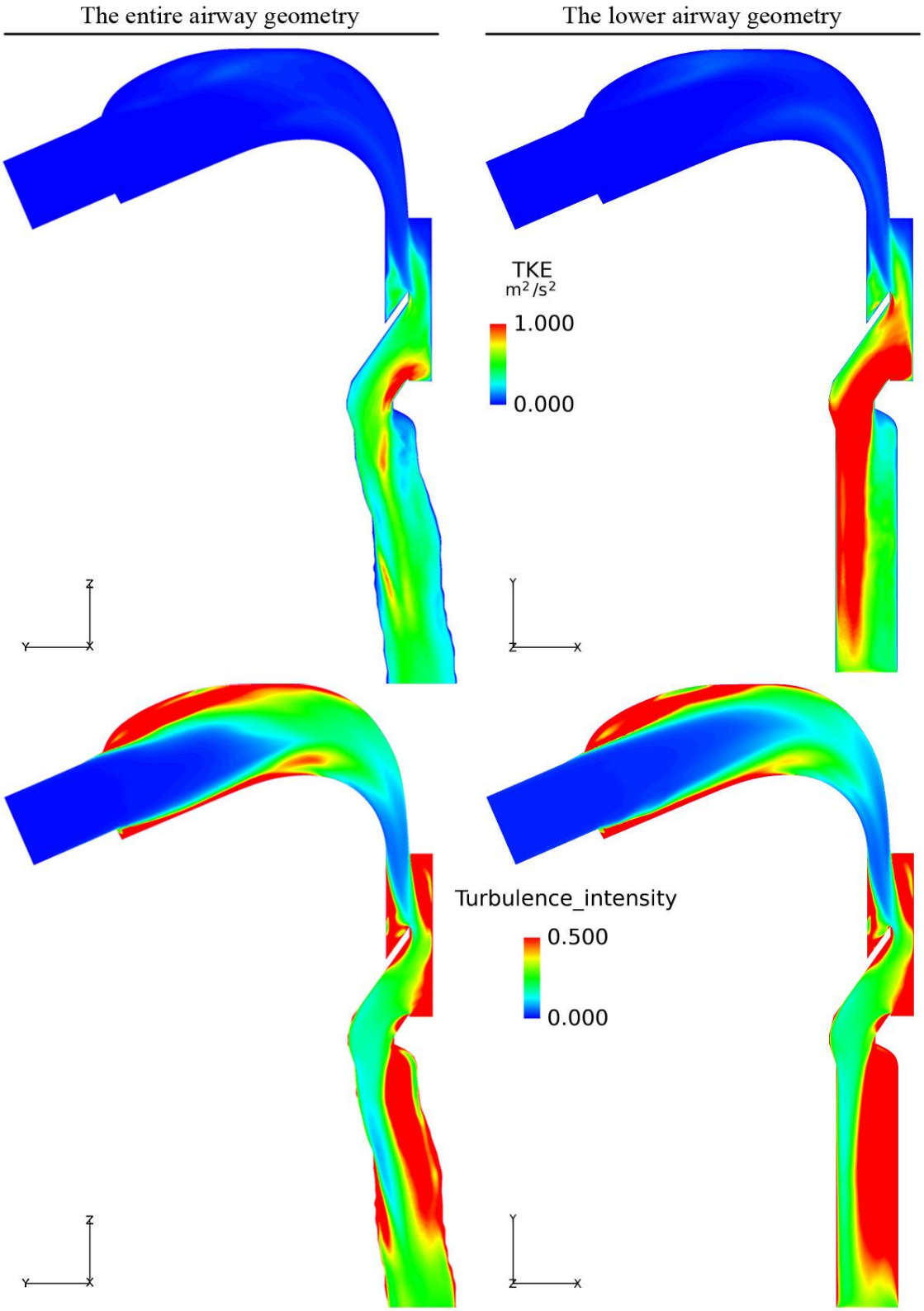

Figure 4.4.1 Central sagittal cross-section of the ETA and the trachea, illustrating TKE and turbulence intensity for high flow rate during inspiration. The values limited to 1 m^2/s^2 and 0.5, respectively

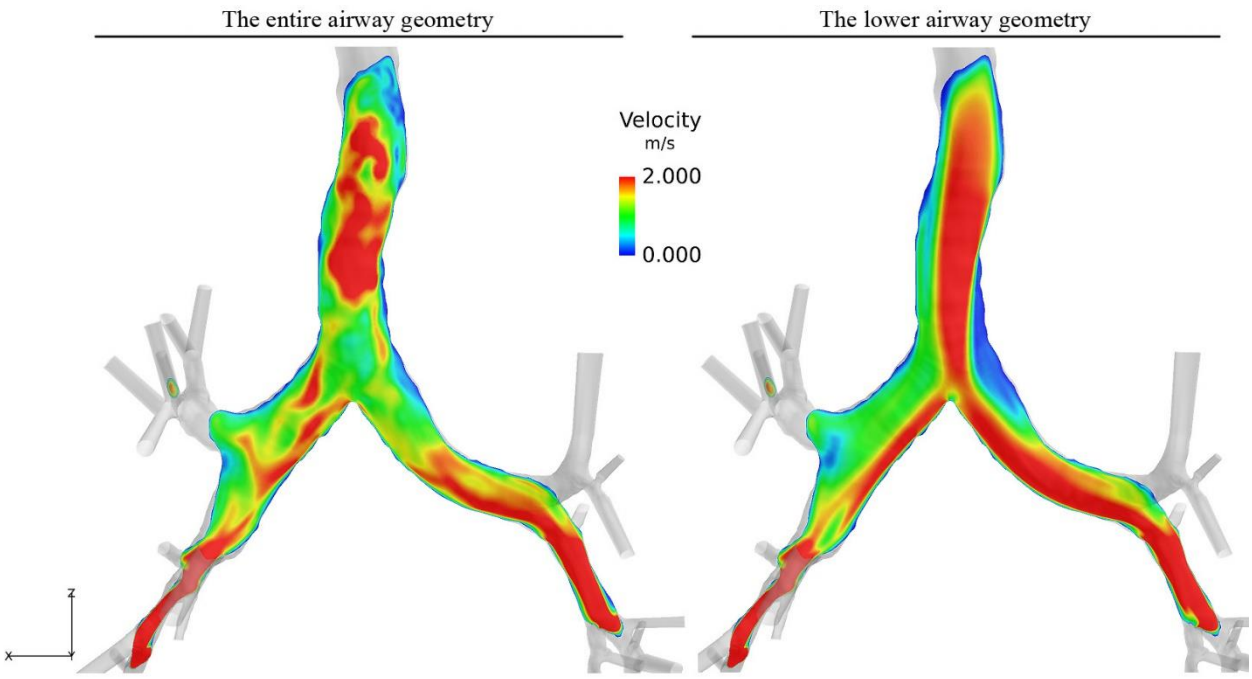

Figure 4.4.2 Cross-sectional plane of velocity magnitude is limited to 2 m/s for $\alpha = 6.68$ during inspiration

Figure 4.4.3 shows the TKE and turbulence intensity of the entire airway solutions and the lower airway. From the TKE contour in the entire airway, high turbulent flow appeared within the trachea and low level of turbulence decreases within the generations. Conversely, the TKE is almost zero throughout the lower airway geometry.

Turbulence intensity is also zero in the lower airway, whereas turbulence intensity can be spotted in different regions of the entire airway. High turbulence intensity can be found in stagnation points, as can be seen in the first bifurcation and second bifurcation of the right daughter branch. Note that high turbulence intensity is expected in other stagnation points that cannot be seen in this figure. The turbulence intensity is high in the central portion of the trachea downstream of the larynx as well as two sheet-like features near both sides of the wall within the trachea.

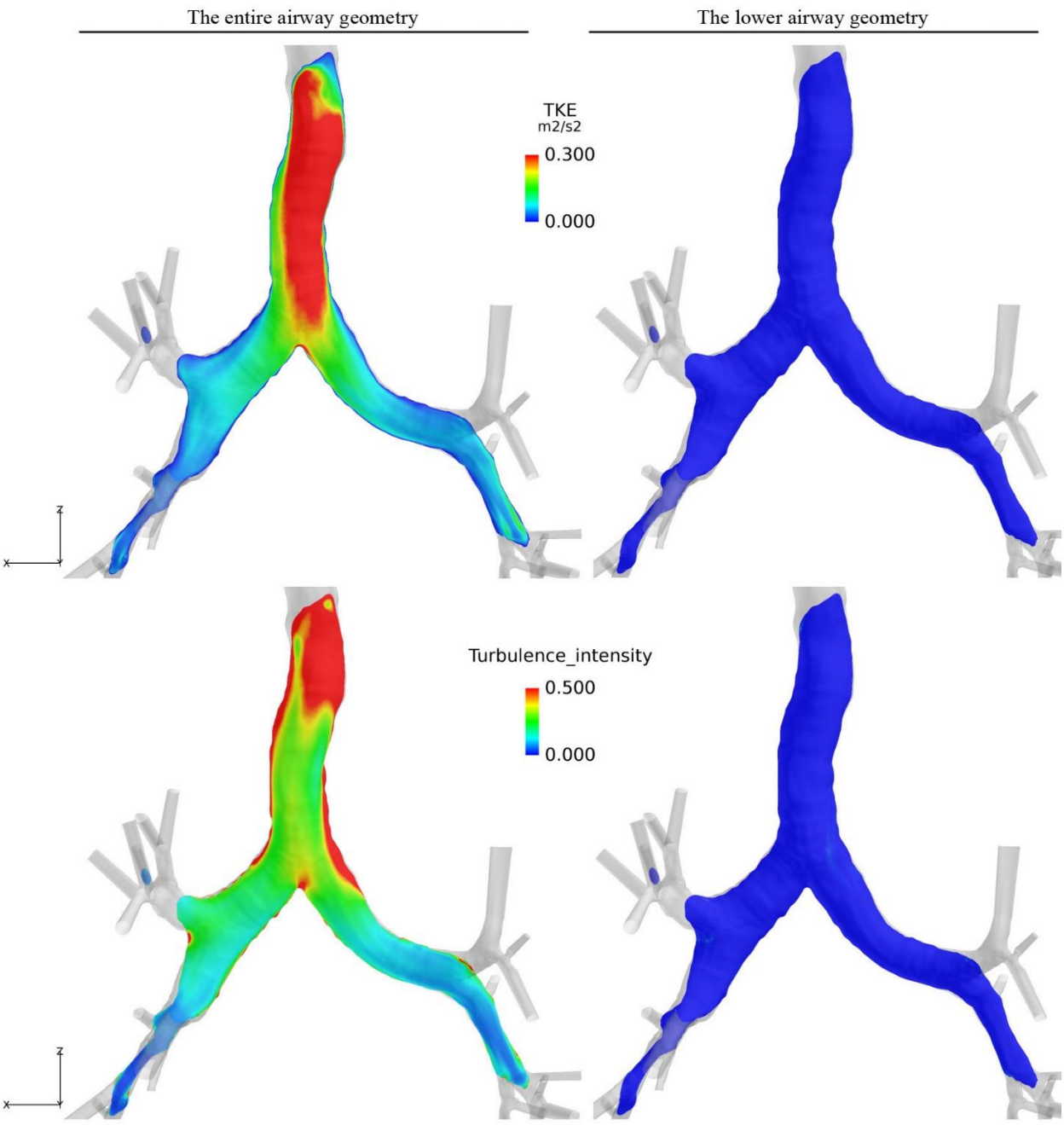

Figure 4.4.3 Cross-sectional coronal plane of the first generation of pulmonary airway, illustrating TKE and turbulence intensity for high flow rate during inspiration. The entire airway and the lower airway geometry are on the left and right, respectively. The values limited to 0.3 m^2/s^2 and 0.5, respectively

The flow in the lower airway geometry with practically zero turbulence intensity suggests quasi-steady laminar flow, while the entire airway geometry displays high levels of turbulence through the trachea as well as both primary bronchi. The high-speed laryngeal jet causes this characteristic of the airflow within the trachea and results in high turbulence levels. However, the level of turbulence intensity reduces significantly through the generations. This suggests that the flow through the lower airways is quasi-turbulent and is not significantly affected by the high-speed laryngeal jet.

Secondary flow velocity vectors, colored by velocity magnitude, are shown at various cross-sections (depicted in Figure 4.2.1) in Figure 4.4.4. The results shown here include that obtained for the entire airway geometry as well as the lower airways geometry. In this figure, only the high flow rate results are shown.

As can be seen from Figure 4.4.4, clear differences are visible in the cross-flow velocity vector patterns for the RS, RM and the LI bronchi, while the differences are less pronounced for the other two locations. However, differences in velocity magnitude (the colors in Figure 4.4.4) can be seen at these two locations (the RI and LS). In the RS, the differences between the two transient breathing solutions are quite clear. The transient breathing entire airway geometry solution shows the presence of two distinct vortices, while the corresponding lower airways solution has three well-defined vortices. The differences between the time-averaged solutions are even more pronounced, with the entire airway geometry showing the presence of a single vortex, while two well-defined vortices can be seen in the lower airways solution. Another comparison that can be made is between the time-averaged and transient breathing solutions. Comparing these for the entire airway geometry, one can see that there are two vortices for the transient breathing case, while there is a single vortex for the time-averaged case. The presence of the

second vortex towards the bottom of the cross-section pushes the other vortex against the edges of the cross-section, effectively squishing it. This also leads to the presence of a higher velocity region down the left side of the cross-section that is absent in the full breathing cycle case. Similar differences can be observed by comparing the time-averaged and transient breathing solutions for the lower airways only. The differences in the secondary flow for the RM are more pronounced compared to the RS bronchus. Similar to the RS, the number of vortices present seems to go up by one when comparing the corresponding time-averaged and transient breathing solutions. The time-averaged lower airways solution has a cloverleaf-like pattern, with the fourth vortex being fairly weak. A comparison of the full breathing cycle solutions for the entire airway geometry with the lower airways only case indicates the presence of a vortex towards the top of the cross-section (for the lower case), which is clearly missing from the entire airway geometry.

Only subtle differences are visible in the cross-flow velocity vector patterns between the solutions for the RI, LS, and LI bronchi. Differences are present in the velocity magnitude at all these stations. A possible explanation for these differences could be the distance to these cross-sections from the entrance to the trachea, i.e., the farther you get away from the exit of the ETA, the lesser its effect will be. This is because the low Reynolds number of the flows through the lower airways which tends to damp out most of the turbulent content with increasing residence time. From the observation in the lower airway geometry only, the flow field can be considered to be quasi-steady and laminar for both flow rates during inspiration. The Reynolds numbers for both flow rates, as tabulated in Table 4.4.1, are lower than the Reynolds number in the trachea in both flow rates, i.e., $\mathrm{Re} = 875$ and $\mathrm{Re} = 1750$. The maximum differences of Re between the transient and constant inspiration was found no more than 0.15% and 1.5% for the low and high flow rates, respectively.

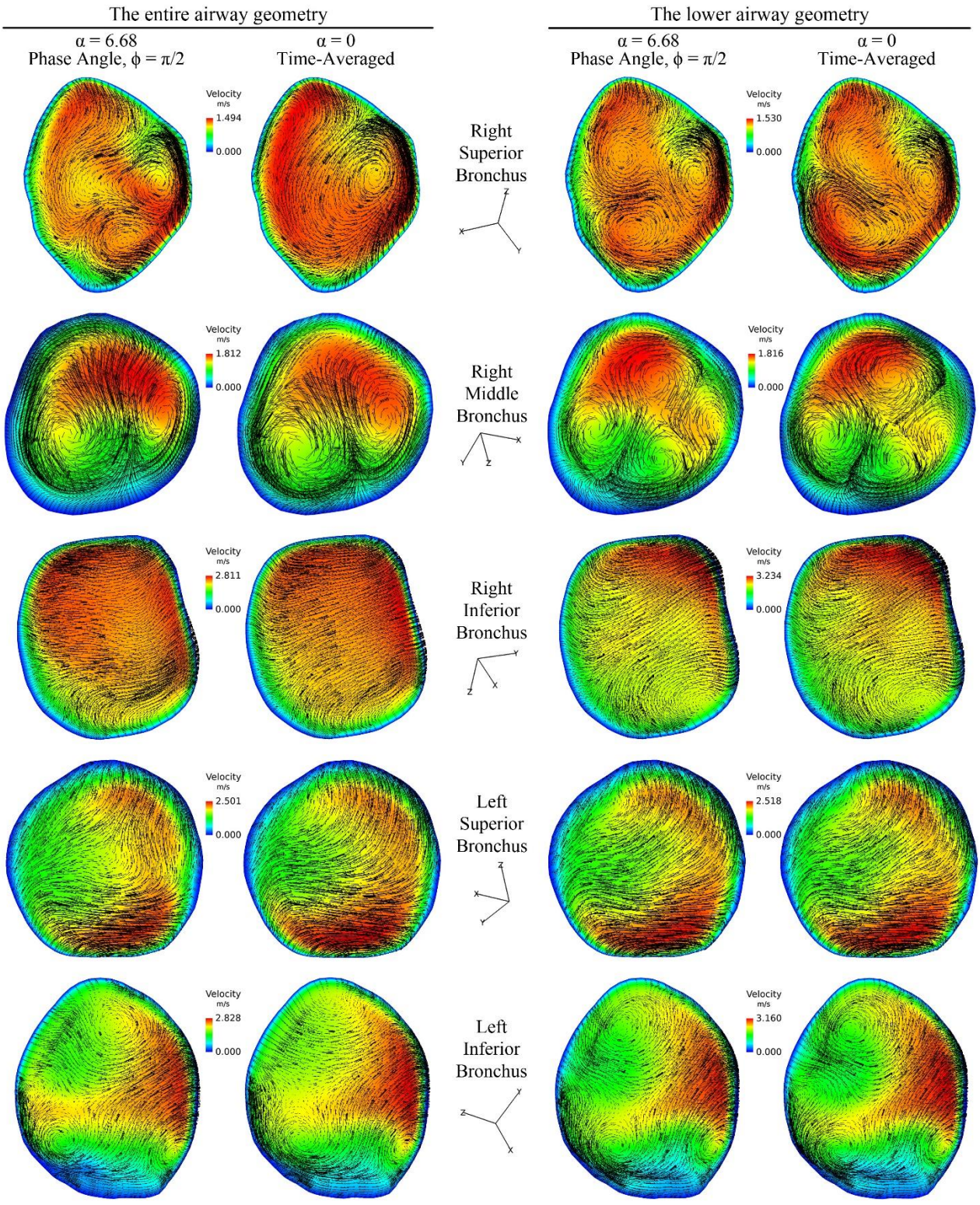

Figure 4.4.4 Secondary flows during inspiration for the entire and the lower airway geometry in the high flow rate. RS, RM, RI, LS and LI lobar bronchus are shown from top to bottom

Table 4.4.1 Reynolds number of constant and transient breathing cycle during inspiration at all five lobar bronchi in the lower airway only

Sections	Low flow rate		High flow rate	
	Re (Constant inspiration)	Re (Transient breathing)	Re (Constant inspiration)	Re (Transient breathing)
RS	381.118	381.215	773.729	759.310
RM	234.594	234.502	469.992	468.339
RI	567.179	566.318	1135.691	1118.158
LS	516.370	515.783	1046.211	1030.479
LI	438.087	437.765	879.891	876.362

In order to determine the existence of turbulent phenomena, the values of TKE and TI are summarized in Table 4.4.2 at all lobar bronchus. The values of TKE are practically zero for the low flow rate, while they are still very small for the higher flow rate. The values of turbulent intensity are small for both flow rates which indicate that the flow is essentially laminar through all the lobar bronchus.

Table 4.4.2 Values of TKE, U and TI during inspiration at all five lobar bronchi in the lower airway only

Sections	Low flow rate			High flow rate		
	TKE	U_{local}	TI %	TKE	U_{local}	TI %
RS	2.237e-16	0.581	2.102e-06	2.577e-06	1.181	1.109e-01
RM	0.0	0.521	0.0	4.911e-07	1.044	5.481e-02
RI	0.0	1.081	0.0	1.633e-06	2.163	4.824e-02
LS	1.507e-17	0.785	4.037e-07	2.795e-06	1.578	8.650e-02
LI	6.625e-16	0.879	2.391e-06	6.986e-06	1.781	1.211e-01

The values of Reynolds numbers in the entire airway geometry are summarized in Table 4.4.3. The most affected lobar bronchi are the RS, RM and LS. Note that at the RM cross-section

of the entire airway, discrepancy of the Reynolds numbers were more prominent in $\alpha = 6.68$ compared to $\alpha = 4.72$.

Table 4.4.3 Reynolds number of constant and transient breathing cycle during inspiration at all five lobar bronchi in the entire airway

Sections	Low flow rate		High flow rate	
	Re (Constant inspiration)	Re (Transient breathing)	Re (Constant inspiration)	Re (Transient breathing)
RS	385.109	396.291	781.350	733.032
RM	245.652	233.177	481.116	454.769
RI	566.082	577.698	1084.216	1089.654
LS	514.055	501.962	1001.680	967.802
LI	434.361	439.082	885.701	861.178

The effects of unsteady turbulent flow through the trachea on all lobar bronchus in entire airway can be gauged by comparing the values of Reynolds numbers of the lower airway geometry. Many of lobar bronchus in the entire airway suggested higher values of Reynolds numbers than the lower airway geometry, which shows the impact of the ETA geometry on the pulmonary airways. These effects can be observed in Table 4.4.4 which illustrates higher values of TKE as well as TI compared to Table 4.4.2. Higher flow rate intensifies features of turbulence which is much more pronounced in the entire airway due to the existence of the ETA. The values suggest high level of turbulence at the RS compared to other lobar bronchus.

Table 4.4.4 Values of TKE, U and TI during inspiration at all five lobar bronchi in the entire airway

Sections	Low flow rate			High flow rate		
	TKE	U_{local}	TI %	TKE	U_{local}	TI %
RS	0.00362	0.587	8.369	0.04237	1.192	14.099
RM	0.00099	0.523	4.912	0.02295	1.068	11.571
RI	0.00286	1.078	4.050	0.03543	2.065	7.442
LS	0.00158	0.784	4.139	0.03311	1.588	9.355
LI	0.00312	0.875	5.212	0.04732	1.705	10.417

4.4.2. Expiration

The secondary flow for the expiration case at all cross-sections of lobar bronchus is illustrated in Figure 4.4.5. Again, for the reasons mentioned earlier, only the high flow rate results are shown here. Compared to the inspiration case, only subtle differences are observed between the various solutions. The flow features for all cases are remarkably similar, with the only difference arising in the magnitudes of the velocity between the various cases. This is not surprising given that the flow is now traveling in a direction opposite to the inspiration case, making the ETA downstream of the lower airways. The effect of the ETA will be felt at best as a slight increase in flow resistance, but the overall flow features are not affected by the presence of the ETA.

The most significant differences between the time-averaged and full breathing cycle solutions for the entire airway geometry are seen in the LS and LI cross-sections, where there are some changes to the cross-flow velocity vector patterns. In the transient breathing solution (LI), an additional vortex appears at the bottom right-hand corner that does not exist in time-averaged solution. Furthermore, the velocity magnitude for the time-averaged solution was about 10%

lower than the transient breathing one. The maximum velocity (time-averaged) for the RI bronchus was approximately 4.2% lower than the breathing cycle case, while this difference was much more significant in the LS, with 18%. Moreover, in the LS bronchus of the lower airway, prominent differences can be seen in the velocity magnitude of the time-averaged solutions which is approximately 14% less than the transient breathing solution.

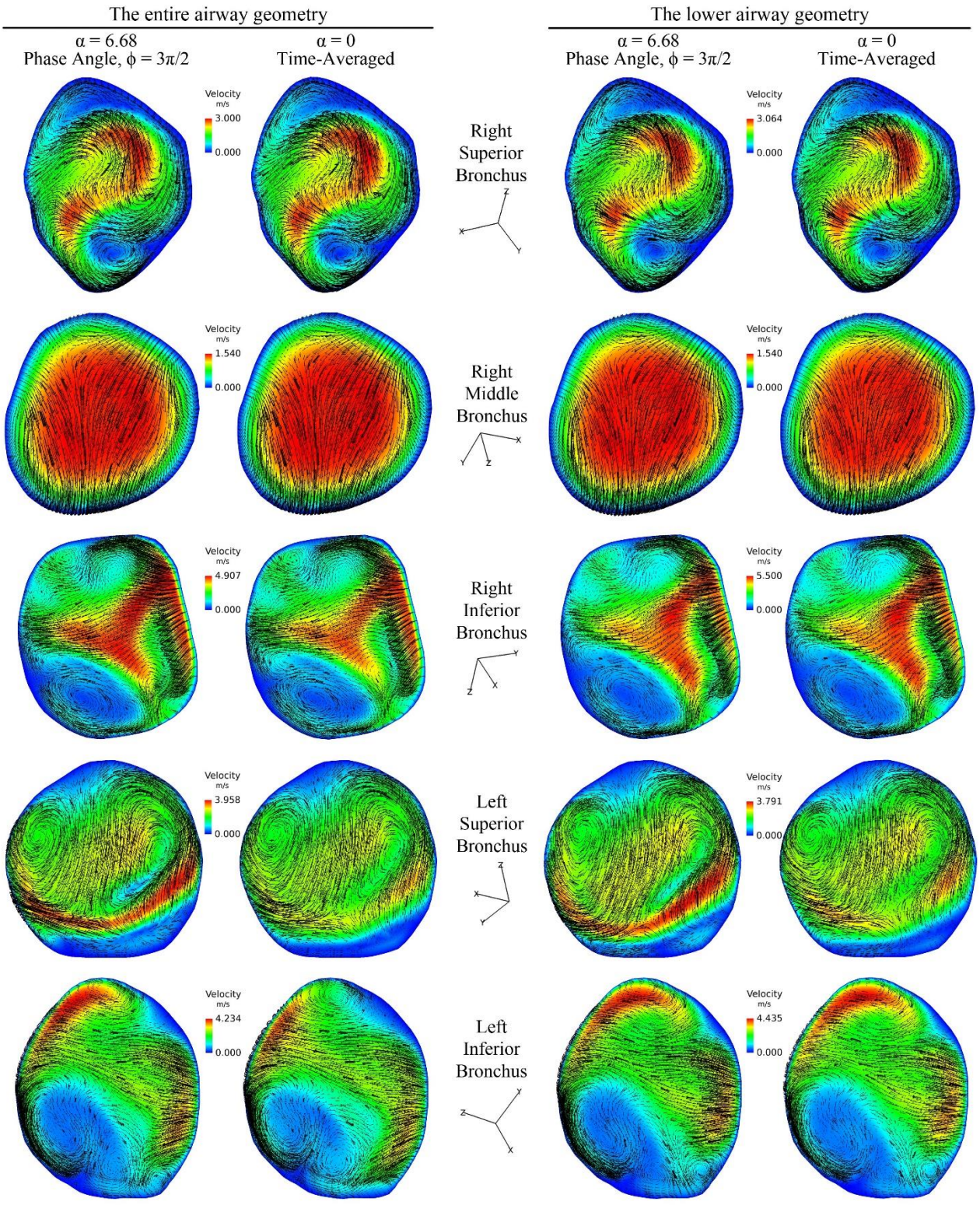

Figure 4.4.5 Secondary flows during expiration for entire and the lower airway geometry in the high flow rate. RS, RM, RI, LS and LI lobar bronchus are shown from top to bottom.

The Reynolds numbers for both flow rates in the lower airway during expiration are summarized in Table 4.4.5. The flow field for low flow rates was found to be essentially quasi-steady and laminar in the full breathing cycle. Small differences in the Reynolds numbers between transient breathing and constant expiration support this statement. Conversely, unsteady motions of the airflow were found for high flow rate. The differences of the Reynolds numbers at most lobar bronchus shows that the effects of unsteadiness significantly increase as the flow rate increases.

Table 4.4.5 Reynolds number of constant and transient breathing cycle during expiration at all five lobar bronchi in the lower airway only

Sections	Low flow rate		High flow rate	
	Re (Constant expiration)	Re (Transient breathing)	Re (Constant expiration)	Re (Transient breathing)
RS	423.132	423.131	866.830	863.562
RM	234.380	234.374	468.019	479.802
RI	623.803	623.383	1271.302	1271.244
LS	557.199	556.905	1129.434	1115.517
LI	535.914	535.765	1039.054	1097.118

The comparison of the values in Table 4.4.6 with Table 4.4.2 indicates that expiratory flow has more fluctuations and unsteadiness compared to inspiratory flows. These effects are much more prominent for higher flow rates. The highest turbulence level can be found at the LS lobar bronchus for the high flow rate. This could be because of the complexity of the geometry in this region which causes high level of unsteadiness and fluctuation during expiration.

Table 4.4.6 Values of TKE, U and TI during expiration at all five lobar bronchi in the lower airway only

Sections	Low flow rate			High flow rate		
	TKE	U_{local}	TI %	TKE	U_{local}	TI %
RS	1.934e-07	0.645	5.567e-02	0.00198	1.318	2.756
RM	2.236e-08	0.520	2.348e-02	0.00019	1.039	1.083
RI	1.142e-07	1.188	2.322e-02	0.00011	2.422	0.353
LS	9.284e-08	0.961	2.588e-02	0.22273	1.863	20.683
LI	3.407e-08	0.948	1.589e-02	0.00241	1.922	2.085

The impact of the ETA on the lower airway can be gauged by comparing the Reynolds numbers of Table 4.4.5 and Table 4.4.7. Comparison of the values in the low flow rate suggested no significant changes in Reynolds numbers. Similar observations for the high flow rate reveal that the RI and LS are the most affected lobar bronchus. Generally, the presence of the ETA has no critical effects on the airflow during expiration.

Table 4.4.7 Reynolds number of constant and transient breathing cycle during expiration at all five lobar bronchi in the entire airway

Sections	Low flow rate		High flow rate	
	Re (Constant expiration)	Re (Transient breathing)	Re (Constant expiration)	Re (Transient breathing)
RS	422.720	418.078	868.619	841.831
RM	235.378	233.603	477.860	472.886
RI	623.425	617.525	1131.423	1205.340
LS	556.009	546.417	1024.050	1049.820
LI	533.122	524.850	1048.693	1094.214

The values of turbulence in Table 4.4.8 illustrate higher levels of turbulence in the entire airway compared to the lower airway only during expiration in Table 4.4.6. In contrast to the

lower airway geometry, expiratory flow in the entire airway has fewer fluctuations compared to inspiratory flow in Table 4.4.4, except the LS lobar bronchus in the high flow rate.

Table 4.4.8 Values of TKE, U and TI during expiration at all five lobar bronchi in the entire airway

Sections	Low flow rate			High flow rate		
	TKE	U_{local}	TI %	TKE	U_{local}	TI %
RS	0.00030	0.645	2.192	0.00382	1.325	3.808
RM	8.906e-05	0.522	1.476	0.00021	1.061	1.115
RI	0.00026	1.187	1.109	0.00330	2.155	2.176
LS	0.00116	0.956	3.416	0.23727	1.881	21.144
LI	0.00035	0.946	1.614	0.00429	1.743	3.068

The TKE and turbulence intensity of the lower airway and the entire airway solutions are provided in Figure 4.4.6 to gain insight into the flow regime that exists in the zeroth generation (trachea) and the first generation. The TKE contours in both geometries revealed the existence of the turbulent flow in the first generation. The level of the turbulence in the lower airway was more pronounced, compared to the entire airway. This can also be seen in the turbulence intensity contours. The turbulence intensity in both geometries revealed the existence of the turbulent flow during expiration. The level of the turbulence in the lower airway was more pronounced compared to the entire airway solution. This shows the importance of the ETA and its effects on the flow regime within the first bifurcation and the trachea. Higher turbulence intensity appeared in the right primary bronchus of both geometries, with the lower airway having higher values compared to the entire airway geometry. Another observation from both solutions is low level of turbulence intensity through the trachea toward the outlet. Therefore, less turbulent flow is expected at the entrance of the larynx in the entire airway geometry.

Figure 4.4.7 provided a better inside into the flow regime through the ETA at the central sagittal plane. The TKE value through the trachea is almost zero in both geometries which illustrates the low level of velocity fluctuation upstream of the larynx. The jet-like flow results in a highly turbulent region in the pharynx which can be observed in the TKE contours of Figure 4.4.7. Strong turbulent motion through the pharynx and oro-pharynx can be seen in both geometries; nevertheless, the TKE value within these regions in the ETA geometry only (geometry on the right) suggested higher values than the entire airway. Similar observation was made during inspiration in Figure 4.4.1. The turbulence intensity in both geometries with slight differences is approximately similar, except within the trachea. There is no intensity through the trachea in the ETA geometry only, while the entire airway geometry shows low level of turbulent flow. This turbulence intensity in the entire airway is the results of the weak turbulent motions caused by the lower airway.

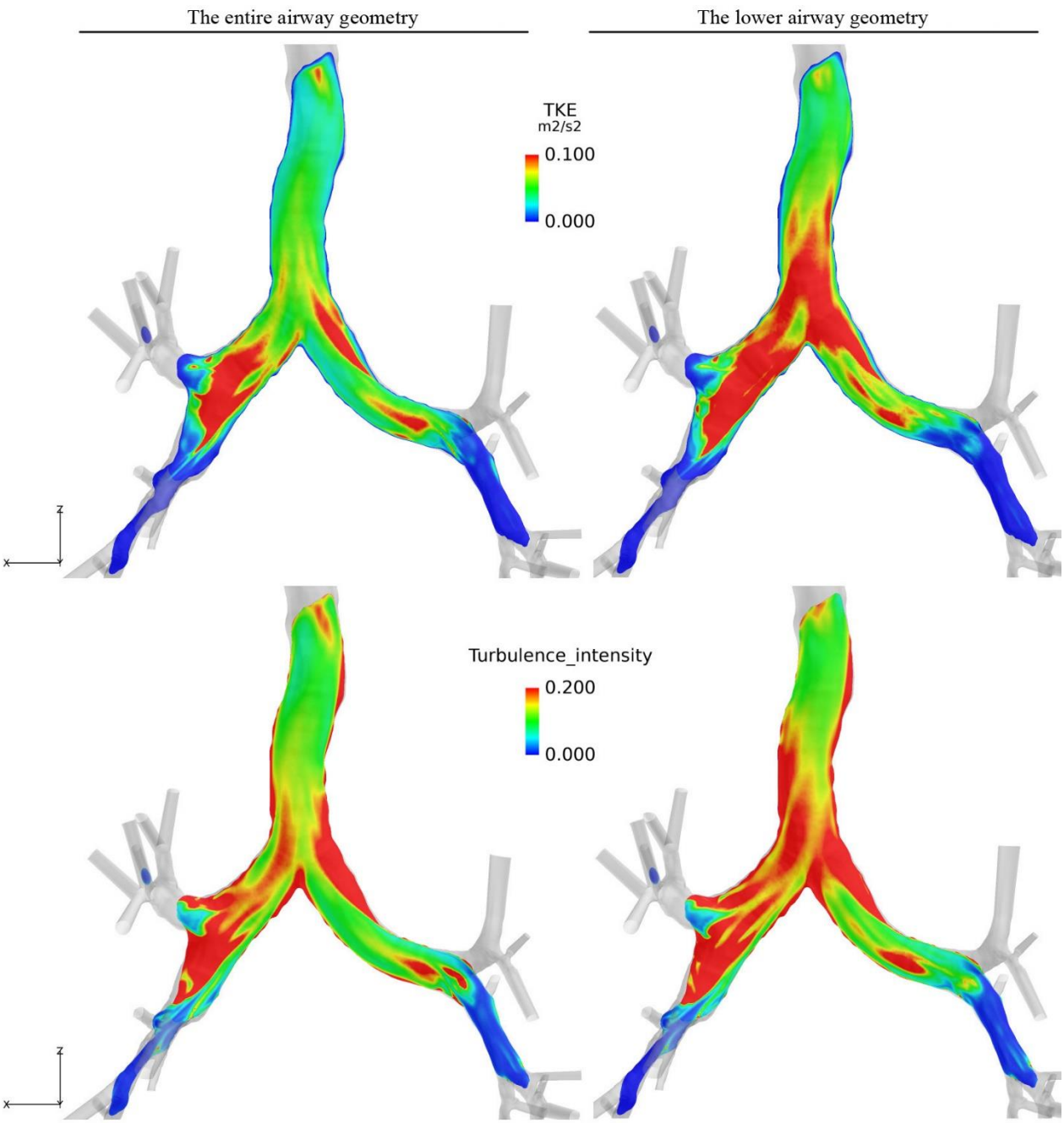

Figure 4.4.6 Cross-sectional coronal plane of the first generation of pulmonary airway illustrating, TKE and turbulence intensity for high flow rate during expiration. The entire airway and the lower airway geometry are on the left and right, respectively. The values limited to 0.1 m^2/s^2 and 0.2, respectively

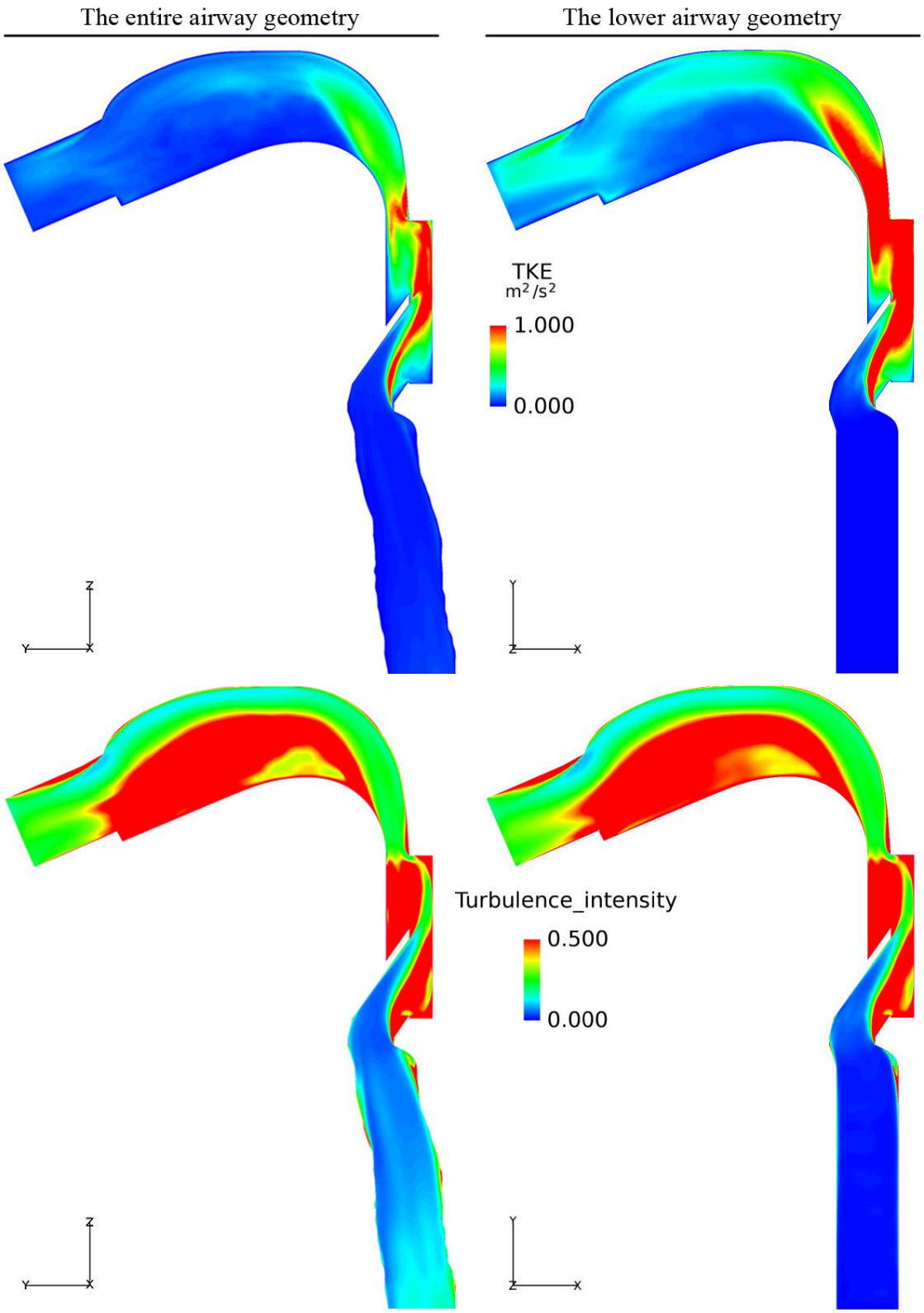

Figure 4.4.7 Central sagittal cross-section of the ETA and the trachea illustrating TKE and turbulence intensity for high flow rate during expiration. The values limited to 1 m^2/s^2 and 0.5, respectively

CHAPTER V

CONCLUSION

Computational simulations have been carried out using *Tenasi* for two different breathing conditions. These computations utilized three geometries namely, the entire geometry, the ETA and the lower airways geometry only. This allowed for an assessment of the impact of the ETA on the flow through the lower airways during inspiration and vice versa.

The accuracy of numerical simulations for the ETA geometry was assessed by comparing the solutions with numerical solutions (LBM) from other researchers and experimental data. Simulations were carried out for two grids, but for comparison purposes, solutions from the coarse grid were used. Taking into account the possibility of geometrical errors in the ETA geometry utilized in this study, acceptable agreement was obtained for the flow rate of 10 l/min.

The flow through the ETA is highly unsteady and has a significant level of turbulence within the trachea, especially near the larynx. Hence, the time-dependent nature of the airflow through the trachea is noticeable. This manifests itself as differences in velocity distributions at the various lobar planes which were considered for analysis. These differences could have a significant impact on drug delivery and point to the need for including the ETA geometry in any lower airways simulations inspiration.

Simulations of transient breathing were carried out for four breathing cycles in order to observe ensure no significant changes to the flow field during peak inspiration/expiration. The first cycle of solutions were considered for comparison.

During inspiration cycle, the airflow was observed to be laminar in the oral cavity and become transitional and turbulent after the oro-pharynx, the pharynx and the larynx, but eventually the airflow turned into laminar flow again through generations. The values of the turbulence intensity at the lobar branches illustrated this behavior of the flow field.

In expiratory flow, the differences in the flow patterns at all lobar cross-sectional planes of the lower airway and entire airway were not significant. This was expected because, in the expiration case, the lower airway is upstream of the ETA. This was observed by comparing the Reynolds numbers at these locations. The low level of turbulence intensity exhibited through the trachea of the entire airway geometry, but their effect on the ETA was not prominent. This conclusion was made by comparison with the ETA geometry only. It was observed that the highly turbulent flow occurred in the pharynx, the oro-pharynx and the oral cavity. Similar to inspiration, this complexity of the flow is mainly due to the existence of the jet-like flow formed in the larynx. Therefore, the effects of the jet flow on the flow regime were found to be significant in either inspiration or expiration. The value of Reynolds numbers within the pharynx and the larynx were higher than the Reynolds numbers in the trachea during inspiration, while values at all lobar bronchus showed smaller values than the trachea. Similarly during expiration, the Reynolds numbers within the oro-pharynx and the oral cavity suggested higher values compared to the value in the trachea. This indicates the possibility of turbulent flow though the ETA. Furthermore, expiratory flows in either constant or cyclic show more fluctuations and unsteadiness compared to inspiration.

The impact of constant inspiration/expiration compared to a full breathing cycle was also analyzed by comparing the results of the simulations between peak inspiration/expiration obtained using both the approaches. High levels of velocity fluctuation were found for both

transient breathing cycles in comparison with analogous constant inspiration/expiration flows. The differences between the constant inspiration/expiration and analogous transient breathing depended upon the flow rate, flow acceleration and construction of the geometry. Significant differences were observed in the simulations pointing to the fact that a constant inspiration/expiration approach might not be sufficient to develop an understanding of these complex flow phenomena. Therefore, unsteady transient breathing simulation is much more appropriate for investigation of the particle aerosol trajectories through the respiratory tract. Particle inspiration and deposition was not carried out as part of this research; it is however planned as a continuation.

By considering two flow rates for a normal breathing cycle, this can be deduced that the complexity of the airflow is dependent upon breathing intensity. In other words, higher flow rates caused the airflow to be more complicated. This is much more pronounced, especially through the pharynx, the larynx and the trachea in the entire airway geometry.

CHAPTER VI

FUTURE WORK

In this study, inclusion of the ETA provided the realistic inlet boundary condition with complicated airflow phenomenon entering the lower airway, but the ETA geometry that was utilized was an idealized geometry. Therefore, considering a patient-specific or CT based geometry of the ETA could lead to much more realistic simulation of the airflow through the respiratory tract. Also, the nasal cavity was excluded from the simulation of the airflow through the ETA model of the human upper airway utilized in this study. Thus, the effect of the nasal cavity on the flow field through the respiratory tract can be investigated.

A mesh convergence study for all three geometries for transient breathing needs to be performed. Mesh convergence study was carried out for the ETA only to validate LES solutions with experimental and computational results and this need to be extended to the other geometries.

In the case of breathing, there is significant movement in the walls of the respiratory tract. This was not included in this study. Therefore, in the future, the effect of the moving boundary walls on airflow features through respiratory airways needs to be studied.

Investigation of inhaled particle transport and deposition using micron particles or nanoparticles needs to be examined as these are the sources of bronchial infections and disease.

Furthermore, the impact of changing in the flow direction at transition moment between inspiratory and expiratory parts on particle deposition can be investigated.

REFERENCES

[1] Alwan A., Ross A., Resnikoff S., Mendis S., Cruz A.A. and Minelli E., "Global Alliance Against Chronic Respiratory Diseases," 2008-2013. [Online]. Available: http://www.who.int/gard/publications/GARD_actionplan_FINAL.pdf.

[2] Young, T., Palta, M., Dempsey, J., Skatrud, J., Weber, S., & Badr, S., "The occurrence of sleep-disordered breathing among middle-aged adults," New England Journal of Medicine, pp. 328(17), 1230-1235, 1993.

[3] I. Gonda, "Targeting by deposition," Drugs and the pharmaceutical sciences, pp. 54, 61-82, 1992.

[4] Johnstone A, Uddin M, Pollard A, Heenan A, Finlay W. H., "The flow inside an idealised form of the human extra-thoracic airway," Experiments in Fluids, pp. 37(5), 673-689, 2004.

[5] Ball, C. G., Uddin, M., & Pollard, A., "High resolution turbulence modelling of airflow in an idealised human extra-thoracic airway," Computers & Fluids, pp. 37(8), 943-964, 2008a.

[6] Ball, C. G., Uddin, M., & Pollard, A., "Mean flow structures inside the human upper airway. Flow," Turbulence and Combustion, pp. 81(1-2), 155-188, 2008b.

[7] Kleinstreuer, C., & Zhang, Z., "Airflow and particle transport in the human respiratory system," Annual Review of Fluid Mechanics, pp. 42, 301-334, 2010.

[8] Lin, C. L., Tawhai, M. H., McLennan, G., & Hoffman, E. A., "Characteristics of the turbulent laryngeal jet and its effect on airflow in the human intra-thoracic airways," Respiratory physiology & neurobiology, pp. 157(2), 295-309, 2007.

[9] Yu, G., Zhang, Z., & Lessmann, R., "Fluid flow and particle diffusion in the human upper respiratory system," Aerosol science and technology, pp. 28(2), 146-158, 1998.

[10] Stapleton KW, Guentsch E, Hoskinson MK, Finlay WH, "On the suitability of k–e turbulence modeling for aerosol deposition in the mouth and throat: a comparison

with experiment," J Aerosol Sci, pp. 31:739-749, 2000.

[11] Heenan AF, Matida E, Pollard A, Finlay W.H., "Experimental measurements and computational modeling of the flow field in an idealizedhuman oropharynx," Experiments in Fluids, pp. 35:70-84, 2003.

[12] Hahn, I., Scherer, P. W., & Mozell, M. M., "Velocity profiles measured for airflow through a large-scale model of the human nasal cavity," Journal of Applied Physiology, pp. 75(5), 2273-2287, 1993.

[13] Keyhani, K. P. W. M. M., Scherer, P. W., & Mozell, M. M., "Numerical simulation of airflow in the human nasal cavity," Journal of biomechanical engineering, pp. 117(4), 429-441, 1995.

[14] Sarangapani, R., "Modeling particle deposition in extrathoracic airways," Aerosol Science & Technology, pp. 32(1), 72-89, 2000.

[15] E. R. Weibel, Geometry and dimensions of airways of conductive and transitory zones, Springer Berlin Heidelberg, 1963.

[16] Horsfield, K., Dart, G., Olson, D. E., Filley, G. F., & Cumming, G., "Models of the human bronchial tree," Journal of applied physiology, pp. 31(2), 207-217, 1971.

[17] Xu, C., Sin, S., McDonough, J. M., Udupa, J. K., Guez, A., Arens, R., & Wootton, D. M. , "Computational fluid dynamics modeling of the upper airway of children with obstructive sleep apnea syndrome in steady flow," Journal of biomechanics, pp. 39(11), 2043-2054, 2006.

[18] De Backer, J. W., Vos, W. G., Gorle, C. D., Germonpré, P., Partoens, B., Wuyts, F. L., ... & De Backer, W., "Flow analyses in the lower airways: patient-specific model and boundary conditions," Medical engineering & physics, pp. 30(7), 872-879, 2008.

[19] Van Ertbruggen, C., Hirsch, C., & Paiva, M., "Anatomically based three-dimensional model of airways to simulate flow and particle transport using computational fluid dynamics," Journal of Applied Physiology, pp. 98(3), 970-980, 2005.

[20] Corcoran, T. E., & Chigier, N., "Characterization of the laryngeal jet using phase Doppler interferometry," Journal of Aerosol Medicine, pp. 13(2), 125-137, 2000.

[21] Tanaka, G., Ogata, T., Oka, K., & Tanishita, K., "Spatial and temporal variation of secondary flow during oscillatory flow in model human central airways," Journal of biomechanical engineering, pp. 121(6), 565-573, 1999.

[22] Zhang, Z., & Kleinstreuer, C., "Transient airflow structures and particle transport in a sequentially branching lung airway model," Physics of Fluids, pp. 14(2), 862-880,

2002.

[23] Ramuzat, A., & Riethmuller, M. L., "PIV investigation of oscillating flows within a 3D lung multiple bifurcations model," in 11th International Symposium on Applications of Laser Techniques to Fluid Flows, Lisbon, Portugal, 2002, July.

[24] R. R. I. Gruetzemacher, "Numerical simulation of human breathing and particle transport through a CT-based pulmonary airway geometry," The University of Tennessee at Chattanooga, Chattanooga, Chattanooga, 2014.

[25] Jayaraju, S. T., Brouns, M., Lacor, C., Belkassem, B., & Verbanck, S., "Large eddy and detached eddy simulations of fluid flow and particle deposition in a human mouth-throat," Journal of Aerosol Science, pp. 39(10), 862-875, 2008.

[26] Lee, J. H., Na, Y., Kim, S. K., & Chung, S. K., "Unsteady flow characteristics through a human nasal airway," Respiratory physiology & neurobiology, pp. 172(3), 136-146, 2010.

[27] Mihaescu, M., Khosla, S. M., Murugappan, S., & Gutmark, E. J., "Unsteady laryngeal airflow simulations of the intra-glottal vortical structures," The Journal of the Acoustical Society of America, pp. 127(1), 435-444, 2010.

[28] Mylavarapu, G., Murugappan, S., Mihaescu, M., Kalra, M., Khosla, S., & Gutmark, E., "Validation of computational fluid dynamics methodology used for human upper airway flow simulations," Journal of biomechanics, pp. 42(10), 1553-1559, 2009.

[29] Zhang, Y., & Finlay, W. H., "Measurement of the effect of cartilaginous rings on particle deposition in a proximal lung bifurcation model," Aerosol Science and Technology, pp. 39(5), 394-399, 2005.

[30] "T-Rex: Automated Boundary Layer Meshing," 2010. [Online]. Available: http://www.pointwise.com/focus/FocusOn_T-Rex.pdf.

[31] Hyams, D. G., Sreenivas, K., Pankajakshan, R., Nichols, D. S., Briley, W. R., & Whitfield, D. L., "Computational simulation of model and full scale Class 8 trucks with drag reduction devices," Computers & Fluids, pp. 41(1), 27-40, 2011.

[32] Ducros, F., Nicoud, F., & Poinsot, T., "Wall-adapting local eddy-viscosity models for simulations in complex geometries," in International Conference on Computational Conference, 1998.

[33] Womersley, J. R., "Method for the calculation of velocity, rate of flow and viscous drag in arteries when the pressure gradient is known," The Journal of physiology, pp. 127(3), 553-563, 1955.

[34] Berger, S. A., Talbot, L., & Yao, L. S., "Flow in curved pipes," Annual review of fluid mechanics, pp. 15(1), 461-512, 1983.

[35] Dubief, Y., & Delcayre, F., "On coherent-vortex identification in turbulence," Journal of turbulence, pp. 1(1), 011-011, 2000.

VITA

Jamasp Azarnoosh was born in Tehran Iran on June 28th 1989. He attended Azad University Central Tehran Branch and completed the Bachelor of Science in Mechanical Engineering in July 2012. After graduation, due to his deep interest in fluid dynamics he pursued his education in Computational Fluid Dynamics (CFD). He was accepted as a graduate research assistant at the University of Tennessee at Chattanooga in Computational Engineering Program in January 2014. In August 2016, Jamasp was awarded the Master of Science: Engineering from University of Tennessee at Chattanooga.